applied sciences

MDPI

Review

A Review of the Recent Advances in Piezoelectric Materials, Energy Harvester Structures, and Their Applications in Analytical Chemistry

Hamna Shaukat [1], Ahsan Ali [2], Saira Bibi [3], Wael A. Altabey [4,5,*], Mohammad Noori [6,7] and Sallam A. Kouritem [4]

1 Department of Chemical and Energy Engineering, Pak-Austria Fachhochschule: Institute of Applied Sciences and Technology, Mang, Haripur 22621, Pakistan
2 Sino-Pak Center for Artificial Intelligence, Pak-Austria Fachhochschule: Institute of Applied Sciences and Technology, Mang, Haripur 22621, Pakistan
3 Department of Materials Engineering, Pak-Austria Fachhochschule: Institute of Applied Sciences and Technology, Mang, Haripur 22621, Pakistan
4 Department of Mechanical Engineering, Faculty of Engineering, Alexandria University, Alexandria 21544, Egypt
5 International Institute of Urban Systems Engineering (IIUSE), Southeast University, Nanjing 210096, China
6 Department of Mechanical Engineering, California Polytechnic State University, San Luis Obispo, CA 93405, USA
7 School of Civil Engineering, University of Leeds, Leeds LS2 9JT, UK
* Correspondence: wael.altabey@gmail.com; Tel.: +86-173-6847-6644

Abstract: Energy harvesting from piezoelectric materials is quite common and has been studied for the past few decades. But recently, there have been a lot of new advancements in harnessing energy via piezoelectric materials. In this regard, several studies were carried out in analytical chemistry. This paper provides a detailed review of different piezoelectric materials, their structures, their fabrication processes, and their applications in analytical chemistry. Detection of the various gases percentage in ambient air is a valuable analytical chemistry technique. Additionally, the benefits of using piezoelectric materials, i.e., crystal for gas and liquid chromatography, virus detection including COVID-19 virus detection, water determination, trace metal analysis and the ability to measure micro weights with quartz crystal with some other applications are also described in this review. Energy harvesting is incredibly important and must be implemented on a large scale. So, developing self-powering devices can resolve the problems, and piezoelectric materials are gaining interest day by day because these materials help in energy generation.

Keywords: energy harvesting; piezoelectric materials; analytical chemistry; COVID-19 virus detection

check for updates

Citation: Shaukat, H.; Ali, A.; Bibi, S.; Altabey, W.A.; Noori, M.; Kouritem, S.A. A Review of the Recent Advances in Piezoelectric Materials, Energy Harvester Structures, and Their Applications in Analytical Chemistry. *Appl. Sci.* **2023**, *13*, 1300. https://doi.org/10.3390/app13031300

Academic Editor: Krzysztof Bernacki

Received: 1 November 2022
Revised: 13 January 2023
Accepted: 13 January 2023
Published: 18 January 2023

Copyright: © 2023 by the authors. Licensee MDPI, Basel, Switzerland. This article is an open access article distributed under the terms and conditions of the Creative Commons Attribution (CC BY) license (https://creativecommons.org/licenses/by/4.0/).

1. Introduction

P. Cure and J. Curie made the initial invention of piezoelectricity in 1880 [1]. The word 'piezoelectricity' originated from two words, 'piezo,' meaning the principle of stress and 'electricity,' meaning dependable on electron movement [2]. Piezoelectric materials generate electric fields in response to applied mechanical stress (piezoelectric effect), and a mechanical strain is produced when subject to an external electric field known as the inverse piezoelectric effect [2–6]. The immediate piezoelectric (PZT) effect is given by Equation (1) [7], and the inverse PZT effect is explained in mathematical Equation (2) [8]. Where: σ and $\in$ are stress and strain tensors, respectively, induced by the mechanical and electrical effects, E and D are the electric field and dielectric displacement vectors, S^E is the elastic compliance matrix, d_{im} and d_{ij} are the piezoelectric coefficients for direct and

converse effects, and e is the permitivity value of the dielectric evaluated under constant stress. The direct and inverse piezoelectric effects are shown in below Figure 1.

$$D = e.E + d_{im}.\,\sigma \tag{1}$$

$$\in = d_{jk}\,.\,E + S^{E}.\sigma \tag{2}$$

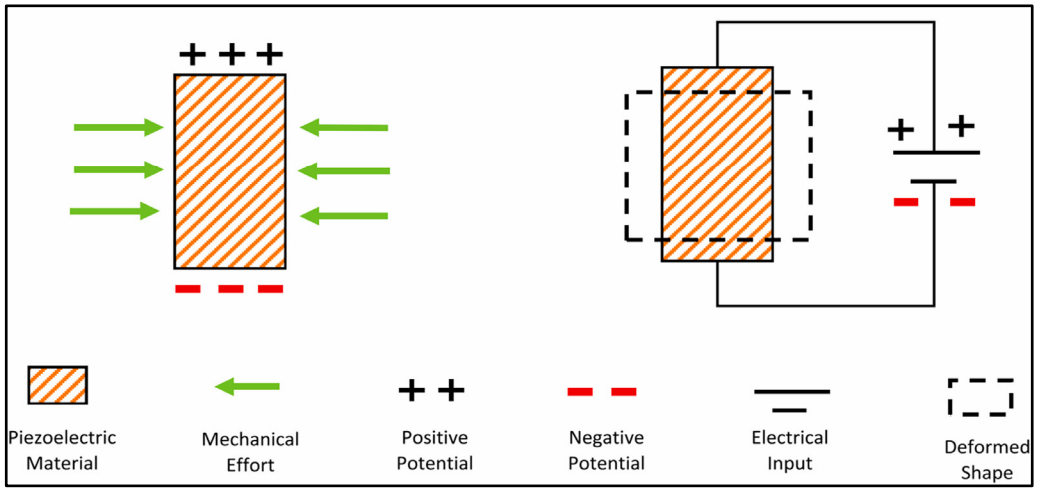


Figure 1. Direct and inverse PZT effect [9].

Due to the zero internal dipole of piezoelectric materials, when strain is produced, the lattice displacement occurs, which results in the movement of dipoles and ultimately causes electric charge generation, and that charge produces an electric field or piezoelectric potential in the material [10,11]. Piezoelectric materials are a great source of energy storage and harvesting [11,12]. From renewable energy inputs, piezoelectric energy harvesters (PEH) may produce power ranging from nanowatts to microwatts by converting mechanical energy into electrical energy [13–16]. Piezoelectric energy harvesters are used in a large variety of products that are all around us, especially smart sensors. These devices have wireless communication capabilities with human beings and one another. The advancement of microelectronics and nanoelectronics technology is dependent on piezoelectric materials. The most sophisticated ambient energy harvesting method is piezoelectric transduction, which has found use in various fields, including transportation, construction, wireless electronics, IoTs, microelectromechanical systems (MEMS), implantable and wearable devices, and many others [17–19]. Compared to the other types of energy harvesters, piezoelectric energy harvesters are particularly effective at absorbing vibrational energy because they are lightweight and simple. The graph in Figure 2 depicts the number of publications on PEH from 2000 to 2020. The graph demonstrates the recent progressive rise of PEH [20,21].

Piezoelectric materials, which include ceramics, single crystals, composites and polymers, have recently been the main topic of research and development. These materials have been made in different forms of device structures, i.e., nanostructure (nanowires, nanorods, nanotubes, and nanoparticles) [22–31] and thin film for the development of piezoelectric nano/generators that will be used in a variety of fields. Their favorable properties, including high piezoelectric coefficient, durability, stretchability, and flexibility, made them ideal for various applications like wireless sensor networks and the Internet of Things (IoTs). It became simple to harvest energy from the environment for a sustainable power supply to sensor nodes due to the gradual increase in the number of deployed sensor nodes in a variety of fields as well as the significant reduction in the power requirement and node size [32,33].

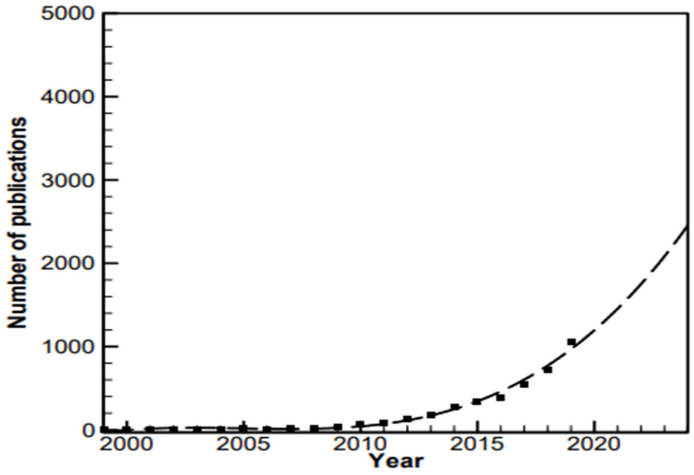


Figure 2. Total publications on PEH between 2000 to 2020 [21].

Humanity needs novel technologies to enhance its quality of life, considering fast-advancing social globalization. Over the last few decades, significant advancements in microelectronics have paved the way for the development of various piezoelectric devices and sensors that can be used in analytical chemistry [34–41]. Sonar was developed as a result of Langevin's utilization of quartz plates as underwater high-frequency wave emitters and receivers. To be utilized as tuning devices and crystal filters for telephone and radio communications, Cady and Pierce created highly stable crystal-controlled oscillators. Because of the continued widespread usage of this technique, crystals of high quality and low cost are readily available for analytical work [42]. It was discovered that the temperature coefficient of crystals might be changed by adjusting the cut angle of the crystal with reference to its optical axis. This discovery produced a wide variety of crystal cuts, which produced crystals with characteristics favorable for a variety of applications. The most used piezoelectric materials are quartz and Rochelle salts, although there are various materials, i.e., ethylenediamine tartrate, tourmaline, barium titanate, and ammonium dihydrogen phosphate. Rochelle salt holds a great piezoelectric effect and is effective and useful in vibrational and acoustic devices, but it must be protected from moisture. The completely oxidized compound is quartz. Quartz is more commonly used than natural ones due to its high purity [43]. Most of the piezo-electric research in analytical chemistry has utilized AT-cut crystals [44].

These days piezoelectric materials are being utilized for a variety of analytical applications, i.e., sorption detectors, detectors for gas and liquid chromatography, detectors for water, analysis of trace metals, detection of viruses, COVID-19 detection, detectors for air pollutants, electrogravimetry, different compound detection, and solution measurements. For example, piezo-electric sorption detectors can be used to determine air pollution. It is also used in detecting carbon monoxide (CO) in the ambient air at the sub-ppm level [45–49]. In the last 10 years, high-pressure liquid chromatography has made significant advances in the technique and applications. This is because of the improvement in the design, which causes an effective separation of high molecular weight and non-volatile compounds [50]. Similarly, a quartz crystal microbalance array can be used to determine the heavy metals in the natural or waste-water samples [51], and piezoelectric-based MEMS sensors are used for the detection of various viruses by providing them an active site to bind [52–56].

This study aims to comprehensively review piezoelectric materials, their structures, and their applications in analytical chemistry. This review has been divided into three sections. The Section 1 focuses on piezoelectric materials. The Section 2 explain the piezoelectric energy harvester's device structure, including nanowires, nanorods, nanotubes, nanoparticles and thin films. The properties of some basic piezoelectric materials are also presented in tabular form, and a comparison is made between the piezoelectric materials based on the piezoelectric coefficient, dij, and the matrix of compliance S^E. The Section 3

focuses on the applications of piezoelectric materials in analytical chemistry (sorption detectors, crystal detectors for water, detectors for gas and liquid chromatography, trace metal analysis, detection of viruses, COVID-19 detection, detectors for air pollutants, and solution measurement). It highlights the range of piezoelectric materials utilized for analytical processes. The steps involved in the piezoelectric energy harvesting process and the overall schematic of piezoelectric energy harvesting are shown in Figures 3 and 4, respectively.

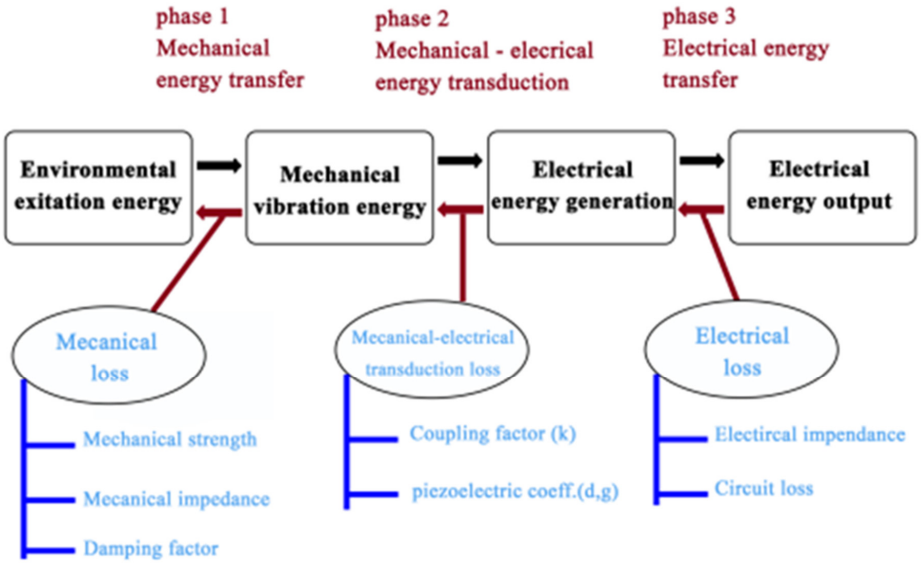


Figure 3. Three steps are included in the piezoelectric energy harvesting process reproduced with permission from [21,57], American Chemical Society, 2015.

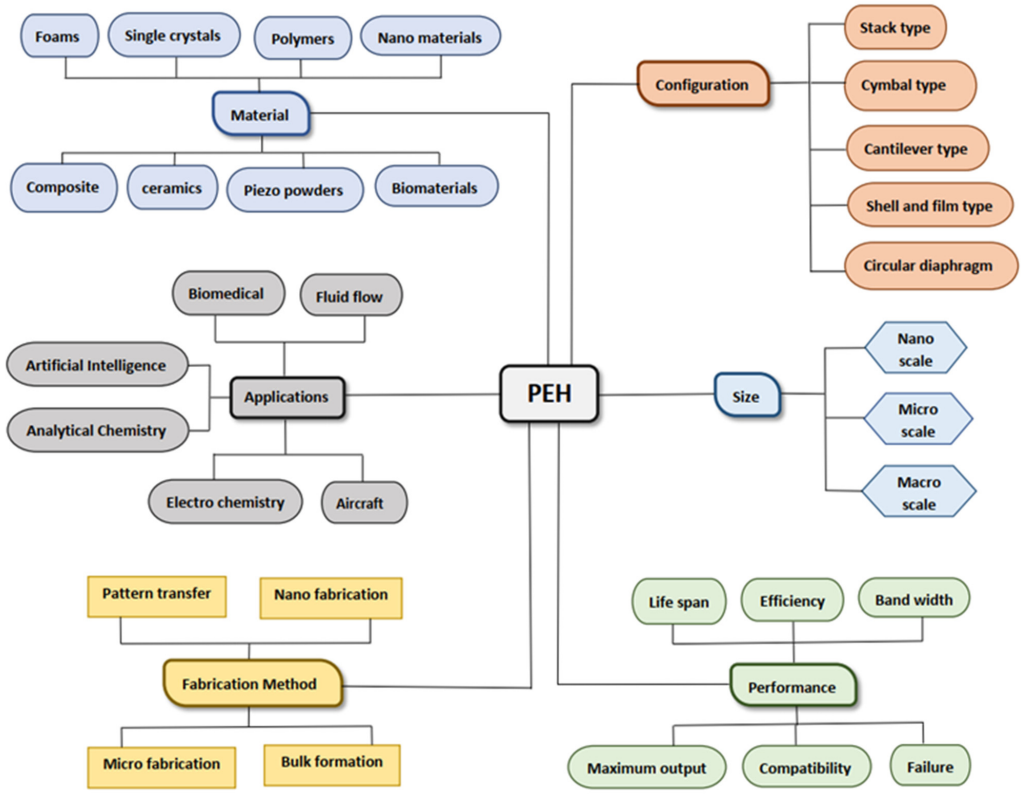


Figure 4. Schematic diagram of piezoelectric energy harvesting.

2. Piezoelectric Materials

In the design of energy harvesters, the most important step is the selection of a suitable piezoelectric material [58]. Piezoelectric materials have been discussed in numerous reviews of energy harvesting. In a variety of applications, different performance measures have been chosen to compare piezoelectric materials. The piezoelectric strain and voltage constants are appropriate parameters in actuating and sensing applications. The electromechanical coupling factor (k), mechanical strength, power density (Pd), manufacturability, mechanical stress (σ), and the quality factor (Q) are the most crucial elements for energy storage. Furthermore, material selection is influenced by the operating temperature [59]. Based on their structural properties, Li et al. [60] divided piezoelectric materials into four categories: composites, polymers, single crystals, and ceramics. In terms of the piezoelectric strain constant (S), electromechanical coupling factor (k), piezoelectric voltage constant (g), mechanical quality factor (Q), and dielectric constant, they described the properties of these four piezoelectric materials and compared them to some of the key candidate materials. In contrast to piezoelectric polymers, they found that piezoelectric ceramics and single crystals had far superior piezoelectric capabilities due to the intense polarization in their crystal lattice. However, they are less flexible and more brittle than piezoelectric polymers. Piezoelectric and mechanical properties must be taken into account when choosing a piezoelectric material for a piezoelectric harvesting application. Application frequency, the volume available, and how energy is delivered into the system are all crucial factors to consider. The PEH should be run at resonance frequency to capture the greatest energy. However, it is frequently impractical to match the input frequency of the host material structure with the resonance frequency of the piezoelectric. They concluded that the piezoelectric element may be thought of as a parallel plate capacitor for low-frequency applications and that the product of the piezoelectric strain constant and the piezoelectric voltage constant should be large to be able to capture more electrical energy. The highest output voltage, however, is reliant on the piezoelectric strain constant, while the harvester's optimal output power is independent of the piezoelectric characteristics of the piezoelectric element under near-resonance conditions. The selection of a piezoelectric material for a piezoelectric harvester is definitely influenced by the operating conditions, which makes the choice of a piezoelectric material more difficult. Table 1 shows the key insights of recent review papers on piezoelectric energy harvesting materials.

Table 1. Overall review papers on piezoelectric energy harvesting materials.

Author	Accomplishments	Piezoelectric Materials	Highlights	Conclusion	References
Li et al.	Considering the range of piezo-electric coefficients, manufacturability, coupling factors, material selection, output power, quality factor, energy density	PVDF, Pu, Cellular PP, PVDF-TrFE, Piezoelectric ceramics, Piezoelectric composite, Quartz	Learn about the techniques created to increase the output performance of PEH devices as well as the current status of research on PEH devices for low-frequency applications. Find out ways to optimize your piezoelectric energy collector designs and how to select the ideal piezoelectric material for your specific application	Life extension, size reduction, durability, energy density, manufacturability, and biocompatibility	[60]
Narita and Fox	Considering the range of piezo-electric coefficients, mechanical strength, manufacturability, energy density, output power	Piezoelectric micro/macrofibres, PVDF-TrFE, PVDF, Pu, Cellular PP, Quartz, Piezoelectric ceramics, Piezoelectric composites	Effectiveness of PZT-based PEH with various structural variations has been observed. By contrasting the results of various piezoelectric environmental harvesters, recent developments in the area of PVDF-PEH and polymer-based piezoelectric composite have been described	Longer life, reduced size, durability, energy density, manufacturability, and biocompatibility	[61]
Lefeuvre	Considering the range of coupling coefficients, energy density, output power	PVDF, Pu, cellular PP, PVDF-TrFE, Quartz	Efficiency rating for energy transformation. For piezoelectric materials, a merit Figure. Explain a comparison of power interfaces with one, two, and three stages	Piezoelectric material selection strategy	[62]
Safaei et al.	Considering the range of piezoelectric coefficient, stiffness, manufacturability, energy density, output power	Piezoelectric micro/macrofibres, Ceramic nanofiber, Polymer nanofiber, Piezoelectric nanowire, Micro/nanofiber, Wire composite material, Piezoelectric ceramic, Piezoelectric Foam, Quartz, Piezoelectric composite	There have been reports of recent developments in the area of piezoelectric materials. An analysis of certain recent piezo materials, i.e., piezo foams and the hot materials	Piezoelectric material selection strategy	[63]
Liu et al.	Consideration of piezoelectric coefficients, material selection guidelines, manufacturability, energy density, power range	Ceramic nanofibers, Polymer nanofibers, PVDF, Pu, Cellular PP, PVDF-TrFE, Piezoelectric ceramics, Piezoelectric foam, Quartz	A discussion of recent developments in the study of piezoelectric materials. Description of various production processes for piezoelectric materials used in energy-harvesting applications. A discussion of the main frequency bandwidth expansion methods. Discover the types of piezoelectric materials, how they are made, and how to expand their frequency range	Increased lifespan, size reduction, durability, energy density, manufacturability, and biocompatibility	[64]

Table 1. *Cont.*

Author	Accomplishments	Piezoelectric Materials	Highlights	Conclusion	References
Zaarour et al.	Consideration of manufacturability, mechanical strength, material selection guidelines, power spectrum or energy density	Piezoelectric micro/macrofibre, Ceramic nanofiber, Polymer nanofiber, Micro/nanofiber, Wire composite material, Piezoelectric nanowire	Manufacturing of nanofiber and wire. References to output current and voltage in nano- and micromaterials. Discover how to compare nano- and micromaterials according to their active area, maximum voltage, and current	Increased lifespan, size reduction, durability, energy density, manufacturability, and biocompatibility	[65]
Yuan et al.	Considering the range of piezoelectric coefficient, quality coefficient, mechanical strength, energy density, output power, stiffness	PVDF, Pu, Cellular-PP, PVDF-TrFE, Piezoelectric ceramics	Introduction of dielectric electroactive polymers and electro strain. Comparison of PZT, PVDF, and electrostrictive polymers in terms of their performance. Describes the difficulties in using dielectrically electroactive polymers in industry	Cost of piezoelectric materials	[66]
Mishra et al.	Piezoelectric coefficient, coupling coefficient, manufacturability	PVDF, Pu, Cellular PP, PVDF-TrFE, Piezoelectric ceramics, Piezoelectric composite, Quartz	This article primarily aims to compare significant forms of piezoelectric composites and polymers and explore the fundamental theories underlying the piezoelectric behavior of composite and polymer systems. The piezoelectric characteristics of numerous piezoelectric polymers and polymer composites are discussed in this article	Piezoelectric material selection strategy	[67]
Bowen et al.	Piezoelectric coefficients, coupling factors	PVDF, Pu, Cellular PP, PVDF-TrFE, Quartz, Piezoelectric ceramic	Discover some trending topics like nanoscale pyroelectric systems, piezoelectric focusing, and pyroelectric-based harvesting	Selection strategies for piezoelectric materials	[68]
Mukherjee and Datta	Piezoelectric coefficient, coupling coefficient, material selection guideline, quality coefficient	Piezoelectric ceramics	Discussion on the impact of the load resistance on PEHs' output power. Discussion regarding piezoelectric ceramic selection criteria	Cost of piezoelectric materials	[69]

3. Structures

3.1. Nanowires

Based on the observation of piezoelectricity, ZnO NW-based (Piezoelectric Nanogenerator) PENG was developed. Numerous studies have concentrated on the conceptualization, structure design, operating mechanism, and output optimization of nanogenerators [70]. Many studies show that PENG can harvest energy. Their output voltage signals are up to several hundred volts, enough to power LEDs and LCDs. Recently, piezoelectric-based lead-free $NaNbO_3$ nanowires with polydimethylsiloxane (PDMS), a polymer-based composite nanogenerator, have been developed [71]. This PENG has been fabricated using lead-free $NaNbO_3$ NWs. $NaNbO_3$ NWs are made using a hydrothermal process at low temperatures, and they can be polarized at room temperature using an electric field. The flexible nanogenerator consists of a $NaNbO_3$ NWs-PDMS composite, and Au/Cr coated films acting as electrodes. Figure 5a,b shows the topographical representation of a $NaNbO_3$ NW. The piezoelectric nanogenerator's structure is depicted in Figure 5c. It is made up of four layers: two Au/Cr-coated Kapton films functioning as electrodes in the yellow, blue, and light blue layers, a $NaNbO_3$-PDMS composite acting as a source of piezo potential, and a solid polyester (PS) substrate film working as the primary driving force of strain. Due to the utilization of all polymer layers in the nanogenerator, the object is flexible and could be bent and released. The power generation process of the nanogenerator is depicted in Figure 5d. Electric dipoles that are neither parallel nor perpendicular to the direction of the NWs are created when a compressive force is exerted. Figure 5d illustrates how the electric dipoles will typically align themselves with the electric field's orientation. Some piezoelectric domains will line up with the electric field's direction, while other zones may tilt away from it. However, the electric dipole element is present in every domain along the green arrow-depicted direction of the electric field. The piezoelectric potential is stronger at the bottom electrode region than at the top electrode area if we apply force parallel to the surface, as shown in Figure 5d. Electric polarization will also align with the dipole direction. The charges should travel from the bottom electrode to the top electrode in the reverse direction if the pressure is relieved, and the piezo potential should dissipate. Thus, both current and voltage are generated as a result of repeatedly applying and relaxing compressive stress. Figure 5e,f shows that the $NaNbO_3$-PDMS composite nanogenerator produces an output voltage of 3.2 V and an output current of 72 nA with a current density of 16 nA/cm^2 under a compressive strain of 0.23%. The findings demonstrate the value of $NaNbO_3$ NWs for applications using lead-free piezoelectric nanogenerators. Similar to the first, a second piezoelectric nanogenerator has been created by converting mechanical energy into electrical energy using cadmium sulfide (CdS) NWs [72]. The CdS NWs arrays, which are grown upwards, are utilized to transform mechanical energy into electrical energy. The hydrothermal approach and the physical vapor deposition technique are the two ways used to manufacture these vertically oriented CdS NWs arrays (PVD). The hexagonal wurtzite (WZ) and cubic zinc blend (ZB) phases with growth directions of WZ <0001> and ZB (111) were alternately present in the NWs produced by the hydrothermal method, while the single-crystalline WZ phase with growth direction <0001> was present in the NWs produced by the PVD process. Figure 6a displays the SEM picture of the hydrothermally generated CdS NWs, and Figure 6b displays the X-ray diffraction pattern (XRD). These NWs have a diameter of 150 nm. 5 nN of normal force and a speed of 150.24 m/s were kept in the AFM contact mode. Figure 6c illustrates how to measure output voltage across a load by moving the tip throughout the sample. A negative output signal was detected when the tip extended beyond the NW, as illustrated by the red curve in Figure 6d and the output power by the blue curve. To improve the output voltage, CdS NWs were synthesized using the PVD process at 950 °C. Figure 6e(i,ii) shows the SEM and TEM photographs of the single CdS NWs synthesized by the PVD process and the higher resolution transmission electron microscope (HRTEM) image at the marked region is shown in Figure 6e(iii). The topography and output voltage when the AFM tip scanned over the CdS NW formed by the PVD technique are shown in Figure 6f,g. The outcome demonstrates that the output

voltage's magnitude is significantly more than the voltage created by the hydrothermal method. The outcome demonstrates that the unique energy harvesters' concept could support the creation of future power electronics.

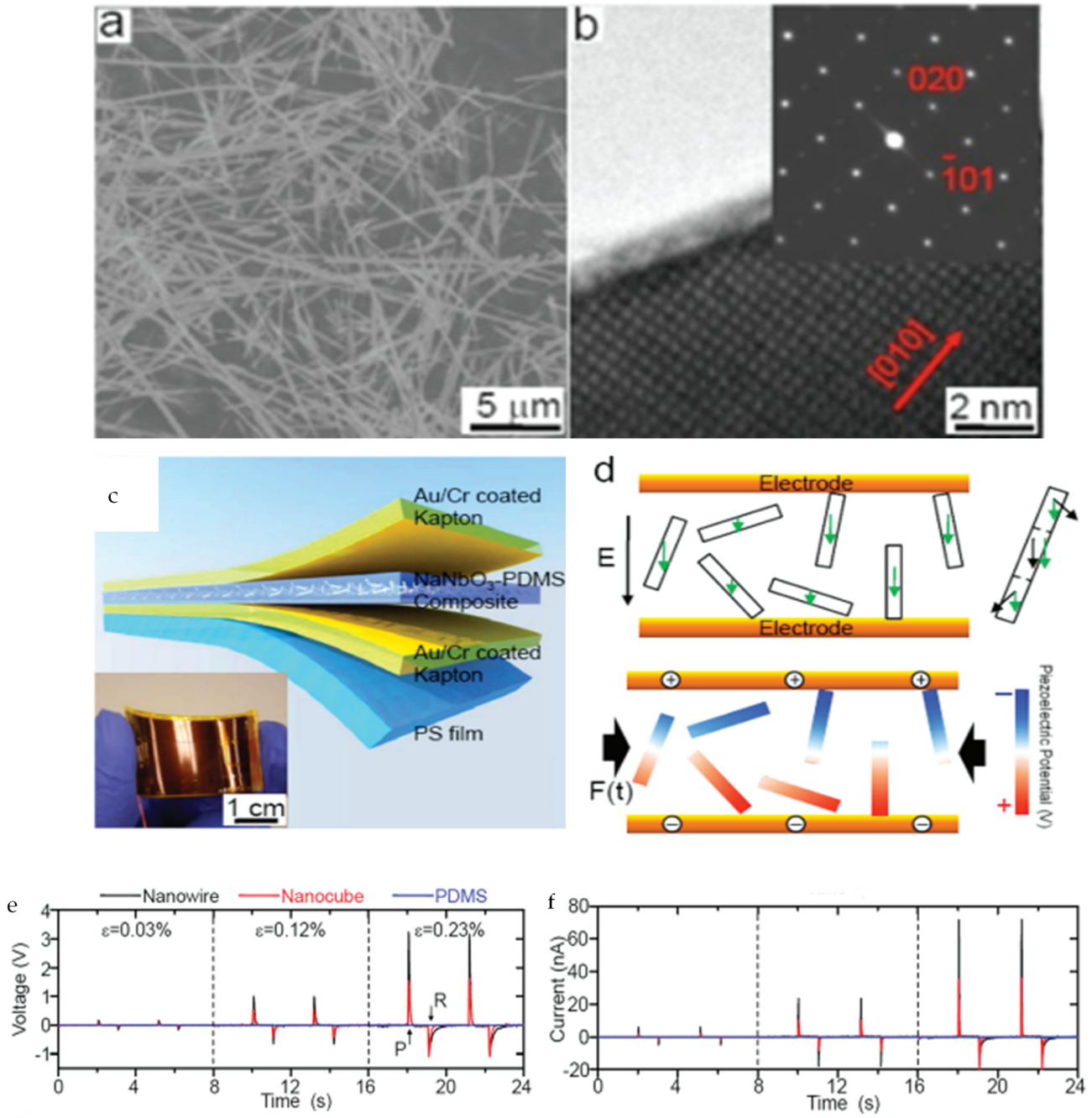


Figure 5. (**a**) SEM image and (**b**) TEM image of $NaNbO_3$ NW; (**c**) structural diagram of a nanogenerator, with the photograph showing nanogenerator device flexibility (inset); (**d**) diagram showing piezoelectric charge generation mechanism of the nanogenerator; (**e**) open circuit voltage and (**f**) short circuit current of $NaNbO_3$ NW (black line) and a nanocube−based (red line) nanogenerator reproduced with permission from [70], American Chemical Society, 2011.

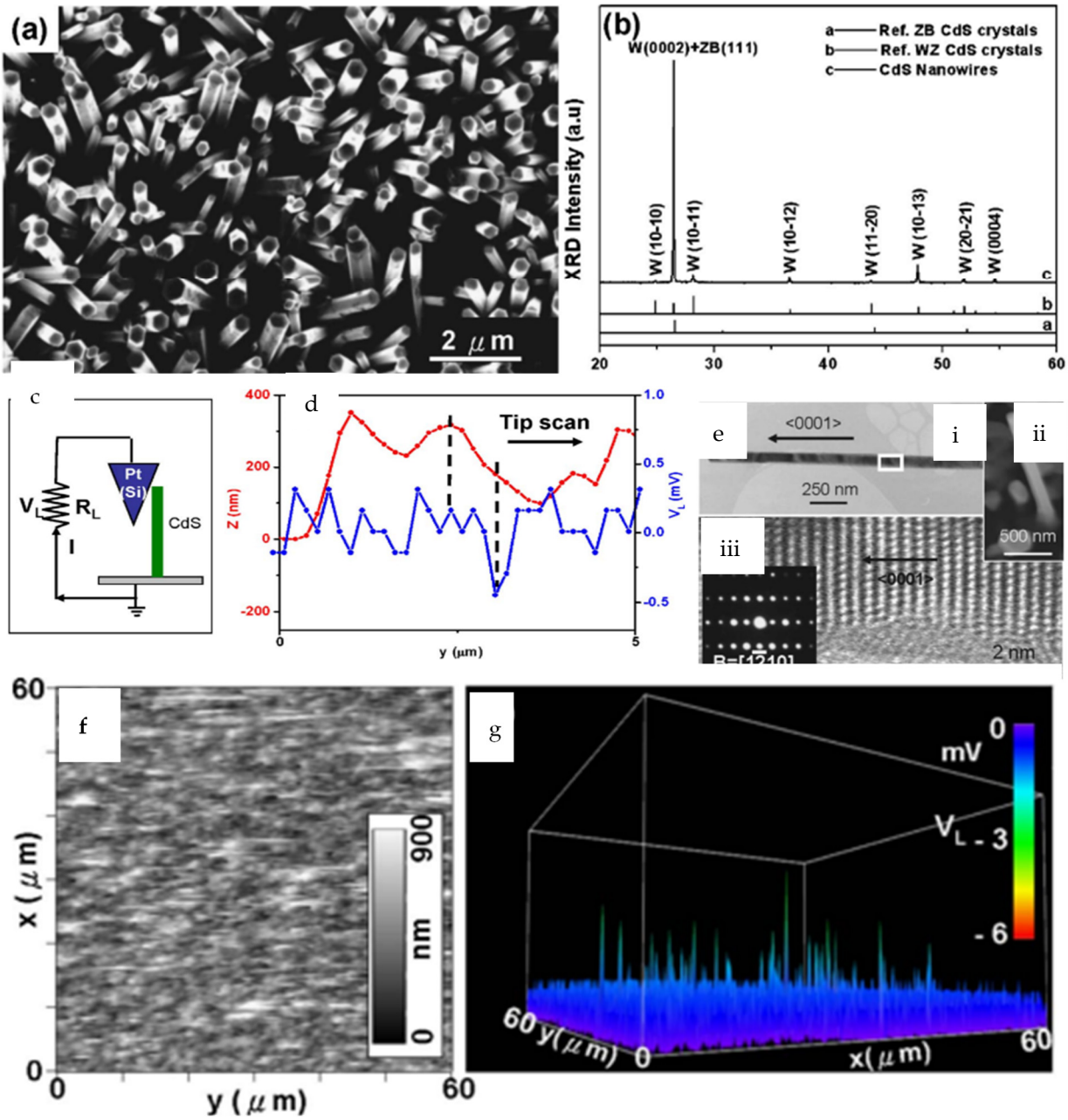


Figure 6. (**a**) SEM image of the CdS NWs produced by the hydrothermal method; (**b**) XRD pattern of the CdS NWs produced by the hydrothermal method; (**c**) schematic diagram of the AFM measurement system; (**d**) line profiles scanned across CdS NWs; (**e**) (**i**) SEM image of the CdS NWs prepared by PVD process (**ii**) TEM image of the CdS NWs prepared by the PVD process (**iii**) HRTEM image of the CdS NWs; (**f**,**g**) topography and subsequent output voltage image of CdS NW respectively reproduced with permission from [72], AIP Publishing, 2008.

3.2. Nanorods

Recently, ZnO-nanorods (NRs) comprised of PENG (ZnO-T-PENG) have been successfully developed [73]. Figure 7 shows the fabrication process of a vertically aligned ZnO NRs array. They are synthesized by using a novel hydrothermal method. In the first step, a precursor solution was formulated by mixing hexamethylenetetramine (HMTA), and zinc acetate dehydrate in deionized water. The nylon fabric piece was washed using alcohol and acetone and deionized with water by means of the ultrasonic method. Then the surface of the fabric is coated with silver (Ag) paste as an electrode by a facile screen-printing

method, as shown in Figure 7a,b. Figure 7c shows the arrangement of ZnO NRs synthesized vertically on the surface of an Ag-coated fabric. After being submerged in a precursor solution for 5 min with the fabric attached to a PTFE holder, a consistent ZnO seed layer was created on the fabric. The PTFE holder with fabric was then once more submerged in a reaction mixture in a sealed beaker and maintained in a water bath for 4 h. Subsequently, the fabric was removed, cleaned, and repeatedly annealed. A vertical ZnO nanotube array with hexagonal cross-sections was then created on the face of the Ag-coated fabric, as seen in Figure 7e. Figure 7f shows the structure of ZnO NRs patterned textile-based-PENG (ZnO-T-PENG), consisting of a vertically arranged ZnO NRs array inserted between the Ag-coated fabric. Figure 8a shows the process of the piezoelectric charge generation of the PENG. When a vertical force is exerted over the surface of the ZnO-T-PENG on the top and bottom sides, respectively, an equal quantity of positive and negative charges are produced, as shown in Figure 8a(i). As a current form, the electrons will start to flow from the top electrode to the bottom electrode (Figure 8a(ii)). The strain on the ZnO NRs increases as more force is applied. Electric charges start to flow backward from the bottom electrode to the top electrode as the applied force is withdrawn (Figure 8a(iii)). The electrons stop flowing when all the force is removed from the ZnO nanorods, as seen in Figure 8a(iv). As illustrated in Figure 8b,c, this PENG can produce an output power of 20 nA and an output voltage of 4 V and 0.8 V, respectively, for palm clapping and finger bending. The development of smart wearable electronics can be aided by this kind of PENG [74]. Similar to this, another method uses piezoelectric ZnO NRs on a standard paper substrate to transform mechanical energy into electrical energy [75]. The standard packing paper with excellent flexibility was employed as the paper substrate in the synthesis of ZnO paper. Radiofrequency (RF) magnetron sputtering was used to coat these pieces of paper with a thick ZnO layer after they had been cleaned with acetone, ethanol, and deionized water. The ZnO NRs were grown by a simple hydrothermal process. The solution that was used was composed of acetate dehydrate and HMTA. After that, the solution was poured into the Teflon reaction kettle, inside of which paper substrates covered in ZnO seeds were hanging vertically. The ZnO paper was then removed and washed. It was washed with deionized water and then baked at 100 C. To act as an electrode, silver (Ag) paste was applied to the two ZnO paper's ends. A flexible ZnO paper nanogenerator (ZPNG) was created after drying. The top and side views of the ZnO NRs in Figure 9a are shown in a highly magnified SEM picture, which unmistakably demonstrates that the ZnO NRs have hexagonal cross-sections. The schematic representation of each paper fiber developed with ZnO NRs is shown in Figure 9b. After the ZnO seed layer had coated the paper fiber, the ZnO NRs that had grown on it began to radiate outward along the fiber. The ZPNG can produce an output voltage and current of 10 mV and 10 nA and has high flexibility and piezoelectric sensitivity. The output voltage and current of the ZPNG after several cycles of rapid stretching (FS) and fast releasing are shown in Figure 9c,d (FR). The enlarged view of one cycle of FS and FR is shown in the insets. The output voltage and output current of the ZPNG are shown in Figure 9e,f at different frequencies, i.e., f1′f2′f3′, and at an applied strain of 2 cm. Figure 9e,f makes it abundantly evident that as the frequency rises, so do the output voltages and currents. The findings demonstrate that this energy harvesting system offers a straightforward and efficient platform to obtain low-frequency mechanical energy for real-world applications.

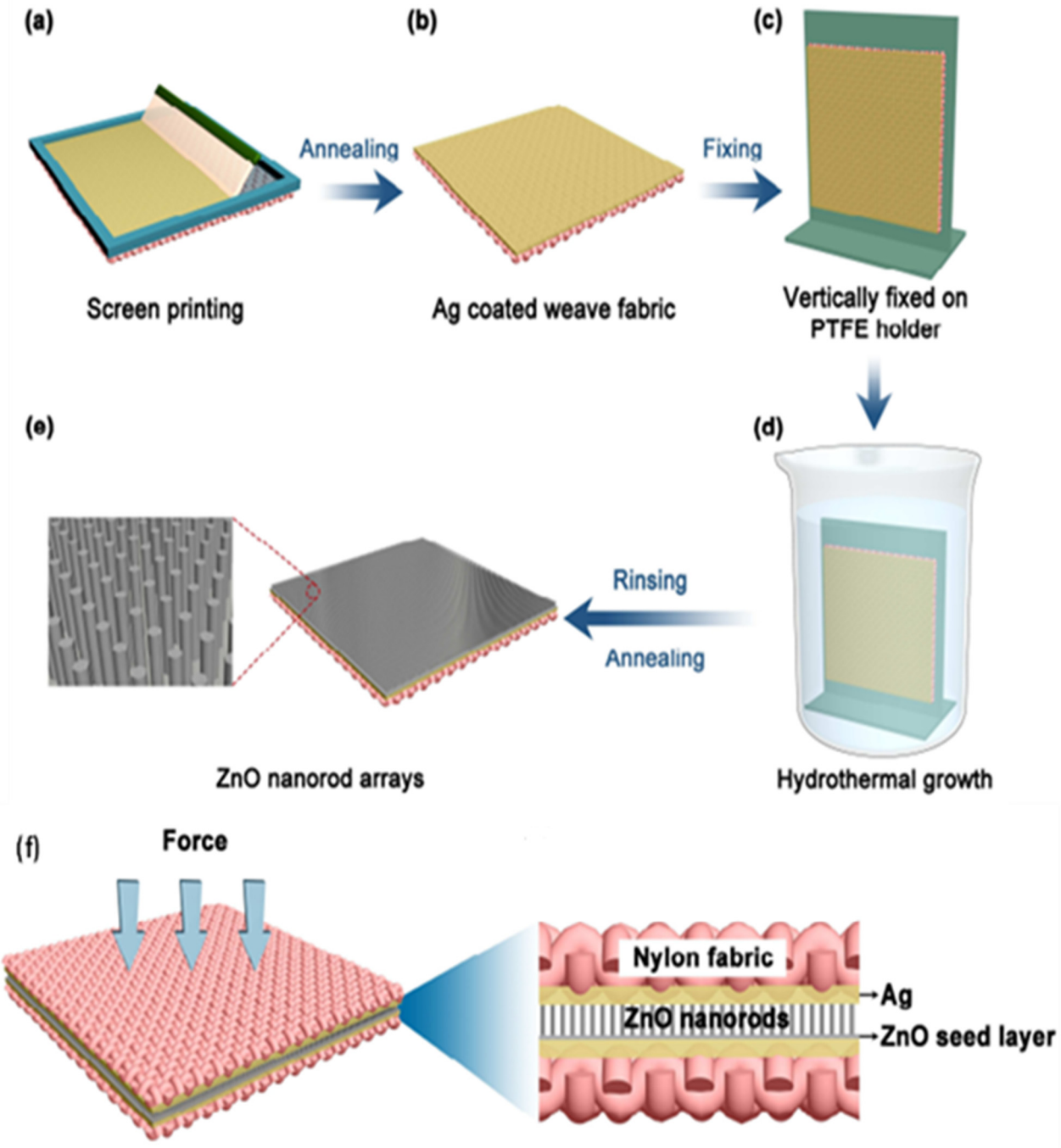


Figure 7. Schematic diagram of the fabrication process of vertically aligned ZnO NRs arrays; (**a**) screen printing method used to coat the fabric's surface as the electrode; (**b**) Ag-coated fabric; (**c**) fabric on a PTFE holder; (**d**) ZnO NRs array hydrothermal growth; (**e**) vertically aligned ZnO NRs array on the surface of the fabric coated with Ag; (**f**) structure of ZnO-T-PENG [73].

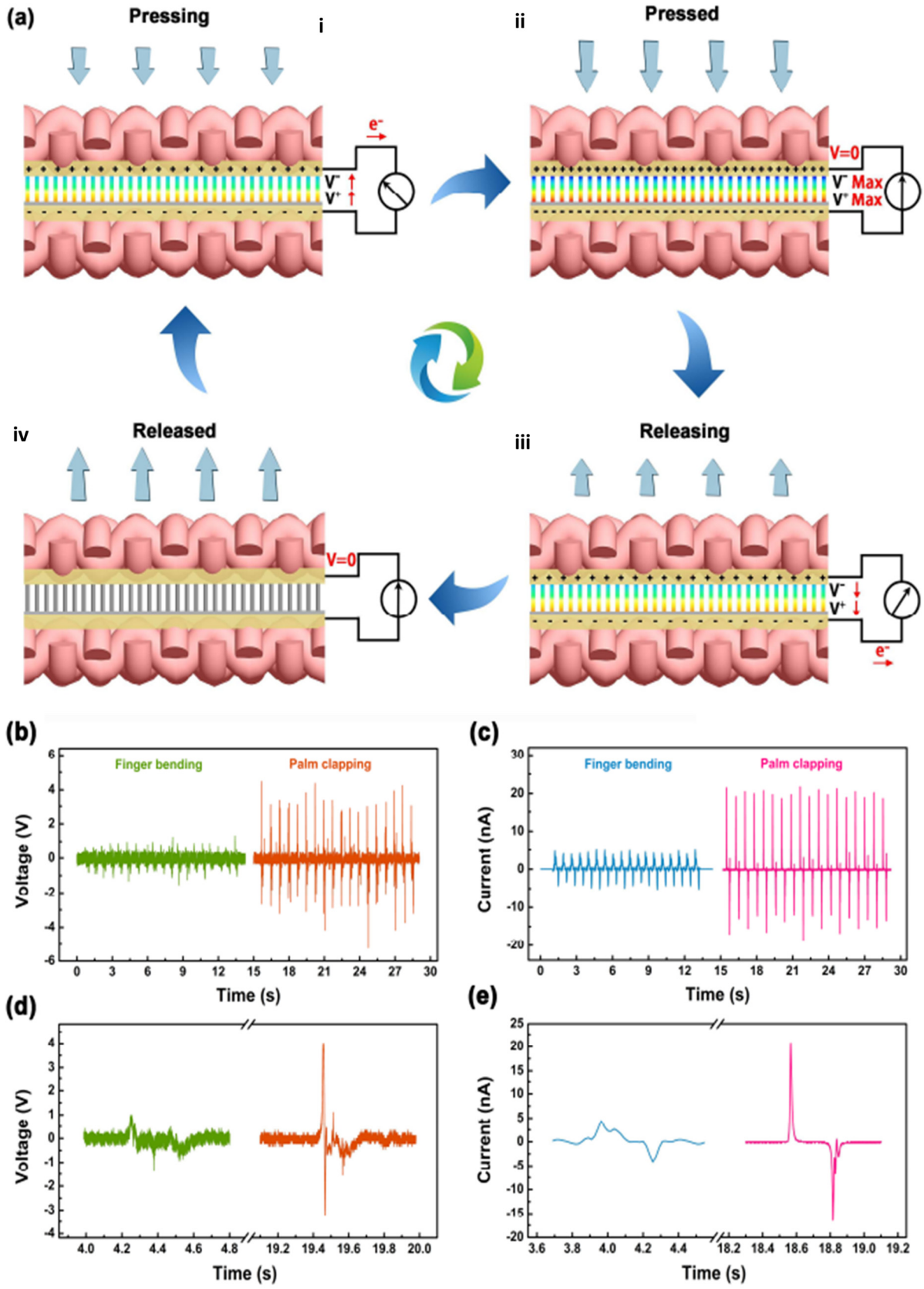


Figure 8. (**a**) Charge generation process of the PENG; (**b**) output voltage (**c**) output current of the PENG by finger bending and palm clapping; enlarged view of one cycle of (**d**) output voltage and (**e**) output current [73].

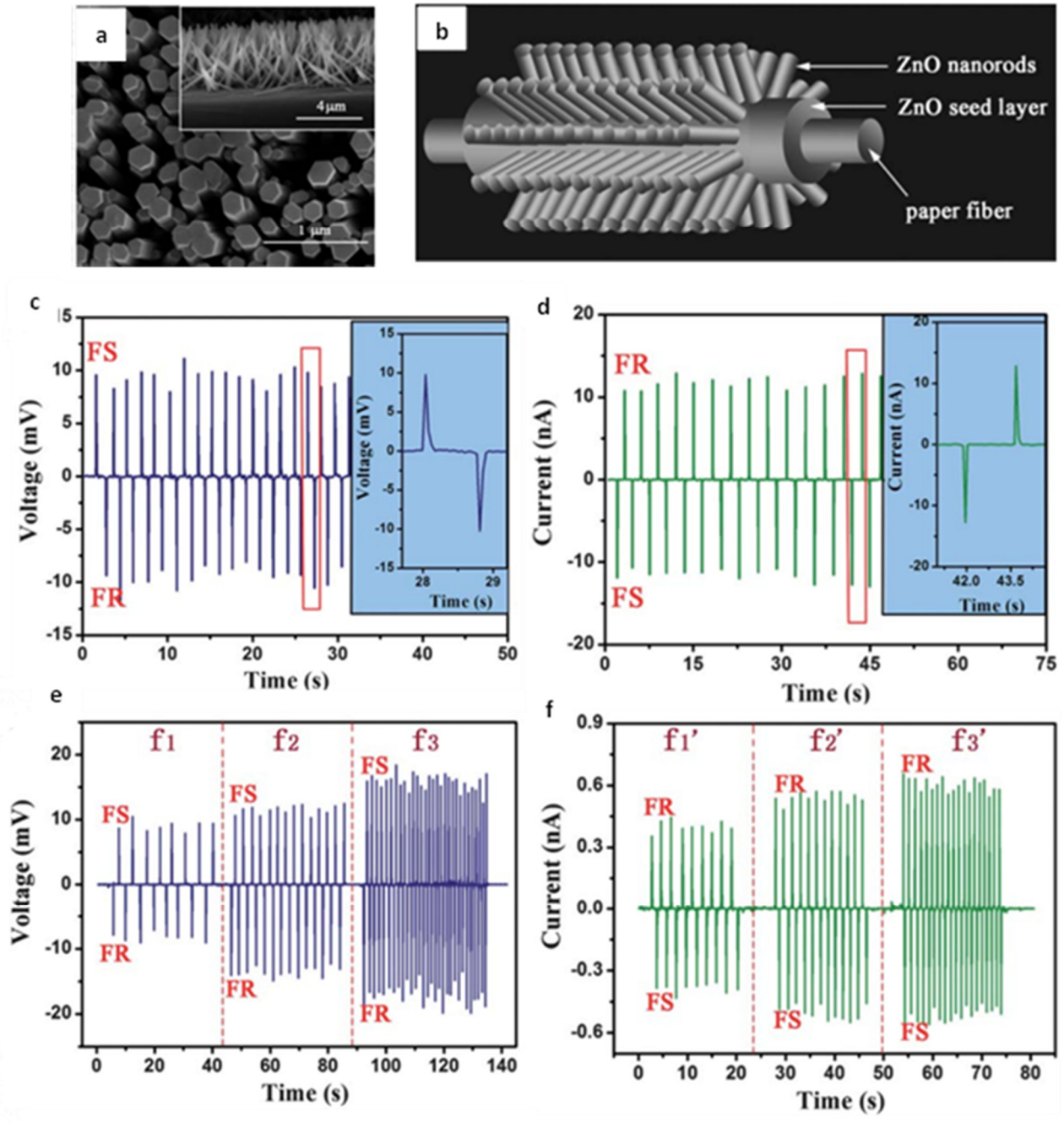


Figure 9. (**a**) Higher magnification SEM image of the ZnO NRs; (**b**) structural diagram of an individual paper fiber grown with ZnO NRs; (**c**) output voltage and (**d**) output current of the ZPNG subjected to repeated cycles of FS and FR; measured (**e**) output voltages and (**f**) output currents at different frequencies and a constant applied strain reproduced with permission from [75], RSC Pub, 2012.

3.3. Nanotubes

Nanotube-based PENGs are very well recognized for powering miniature autonomous, independent systems. Recently, simple, inexpensive, and scalable piezoelectric nanogenerators were fabricated using stretchable and flexible $BaTiO_3$ nanotubes [76]. Figure 10a shows a schematic of a nanogenerator composed of lead-free $BaTiO_3$ nanotubes synthesized hydrothermally by forming composites with PDMS polymers. A direct poling procedure was used to create flexible and transparent nanogenerators. According to Figure 10a, there are five layers in the nanogenerator. Two Au/Cr films act as two upper and bottom electrodes,

$BaTiO_3$ nanotubes and PDMS composites act as piezoelectric potential generators under applied voltage, and a PS substrate. The PS substrate and PDMS serve as supporting and shielding layers to keep the nanogenerators' conformation. The $BaTiO_3$ nanotube/PDMS composite's SEM picture is shown in Figure 10b, which also illustrates how adaptable the manufactured nanogenerators are. The output voltage and current of the constructed nanogenerators are shown in Figure 10c,d. The nanogenerator generates an open circuit voltage of 5.5 V and a short circuit current of 350 nA with a load of 1 Mpa. Because nanotubes are so small, nanogenerators have tremendous performance. To determine whether the generated output signal is the result of the piezoelectric effect, a switching polarity test is carried out. Nanogenerators are connected in two modes, forward and reverse. A positive output signal is generated during the forward link, as shown in Figure 10c, and an opposite output signal is recorded during the reverse link, as shown in Figure 10d. The COMSOL simulation model used to determine the distribution of piezoelectric potential inside the nanogenerator is depicted in Figure 10e. An upper PDMS layer, a $BaTiO_3$ layer, and a bottom PS substrate make up the simulation's three layers. In a similar vein, a hydrophobic piezoelectric nanogenerator based on poly (vinylidene fluoride)-carbon nanotube (PVDF-CNT) foam that is moisture-tolerant was created [77]. Figure 11 shows the fabrication process of nanogenerators based on hydrophobic piezoelectric PVDF-CNT foams fabricated by the solution route. PVDF-CNT foam fabrication involved mixing PVDF pellets, table salt (NaCl), and multi-walled carbon nanotubes (MWCNTs) in a solvent. The solution was held for 1 h at 60 °C with magnetic stirring. After that, the solution was put into a crucible made of silica gel and heated to 90 °C for 5 h. A black polymer composite was produced after cooling. The composite foam was submerged in boiling water to wash away the salt after the outermost layer of the composite sample was removed with sandpaper. Pictures of PVDF-CNT demonstrate how flexible it is. The chain structure of PVDF-CNT foam is crystallized and clearly defined. In order to create piezoelectric nanogenerators, conductive silver (Ag) paint was employed as an electrode. Figure 12a,b illustrates how a compressive force increase of 0.02 kgf resulted in a high output voltage of roughly 12 V and a current density of 30 nA/cm^2 from a flexible piezoelectric PVDF-CNT foam-based nanogenerator. The identical settings as in Figure 12c,e were used to test the piezoelectric output current. To confirm that the generated output signal is the result of the piezoelectric effect, a shifting polarity test is carried out. For this cause, forward as well as reverse linkages are used to connect nanogenerators. The operation of the piezoelectric PVDF-CNT foam-based nanogenerator is depicted in Figure 12g. Figure 12g(i) demonstrates that in the absence of an external force, no output is generated. Due to the piezoelectrically produced potential, electrons move from the top electrode side to the bottom electrode side through the external load when a voltage is supplied perpendicular to the nanogenerator's surface (Figure 12g(ii)). Electrons begin to flow in the opposite direction, returning from the bottom electrode to the top electrode, recording an opposite electrical signal, and the piezoelectric potential vanishes when the force is released (Figure 12g(iii)). The experimental setup schematic for determining the PVDF-CNT piezoelectric device's output power under-regulated humidity levels is shown in Figure 12h. Figure 12i illustrates the piezoelectric output of the instrument under vertical compression at various relative humidity (RH) levels, which produced a voltage output of 8 V even at 60% RH. It was completed. These outstanding performances of the device proved potential applications in ultra-sensitive nanosensors and self-powered nanosystems.

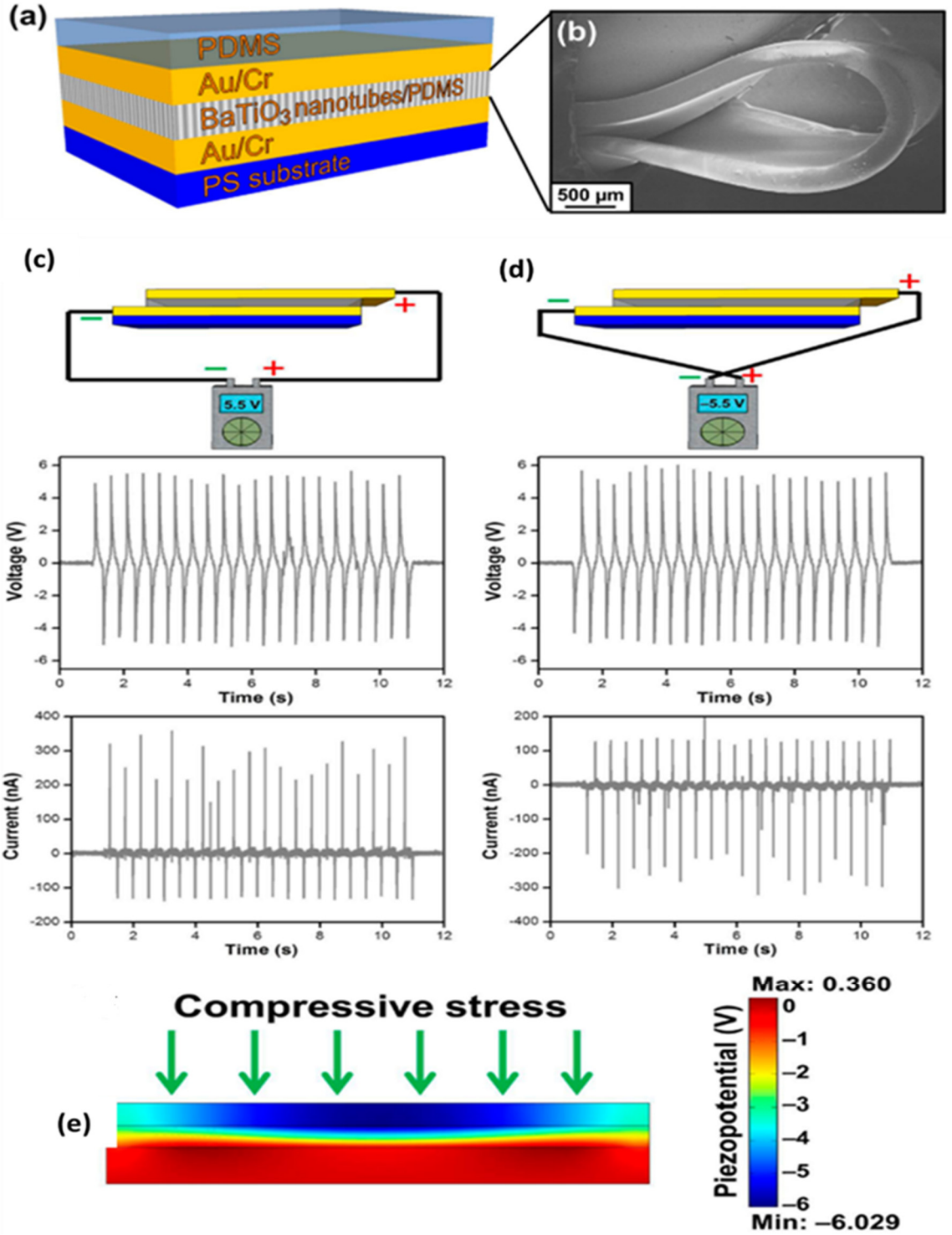


Figure 10. (**a**) Diagram of the manufactured nanogenerator; (**b**) SEM illustration of the $BaTiO_3$ nanotubes/PDMS composite; output voltage and output current of the nanogenerator measured under (**c**) forward connection (**d**) reverse connection; (**e**) COMSOL simulation model of the nanogenerator reproduced with permission from [76], American Chemical Society, 2012.

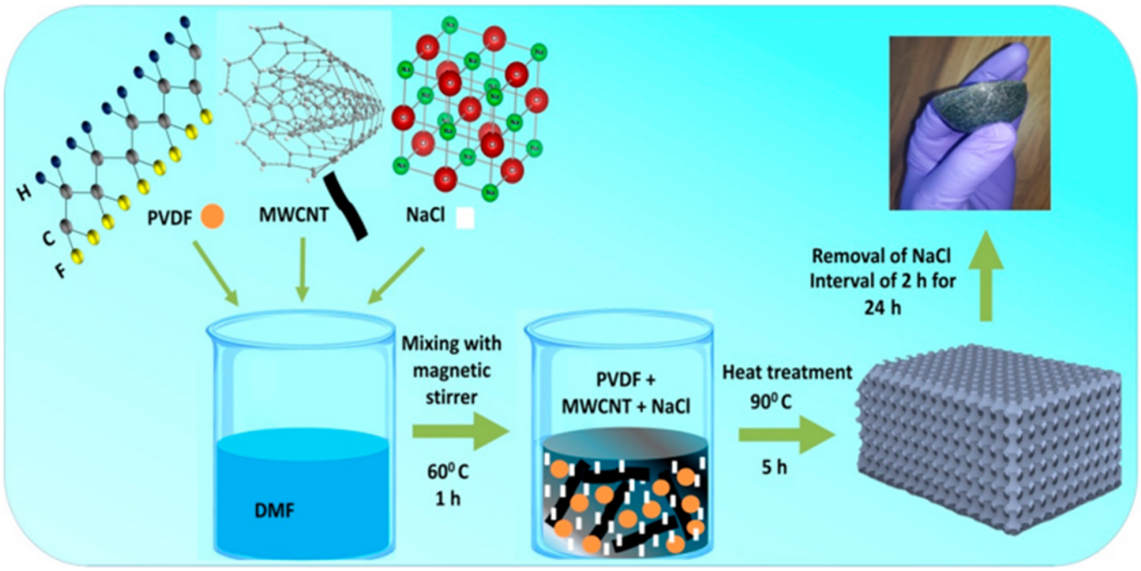


Figure 11. Diagram of the fabrication process of hydrophobic piezoelectric PVDF-CNT foam-based nanogenerator reproduced with permission from [77], American Chemical Society, 2021.

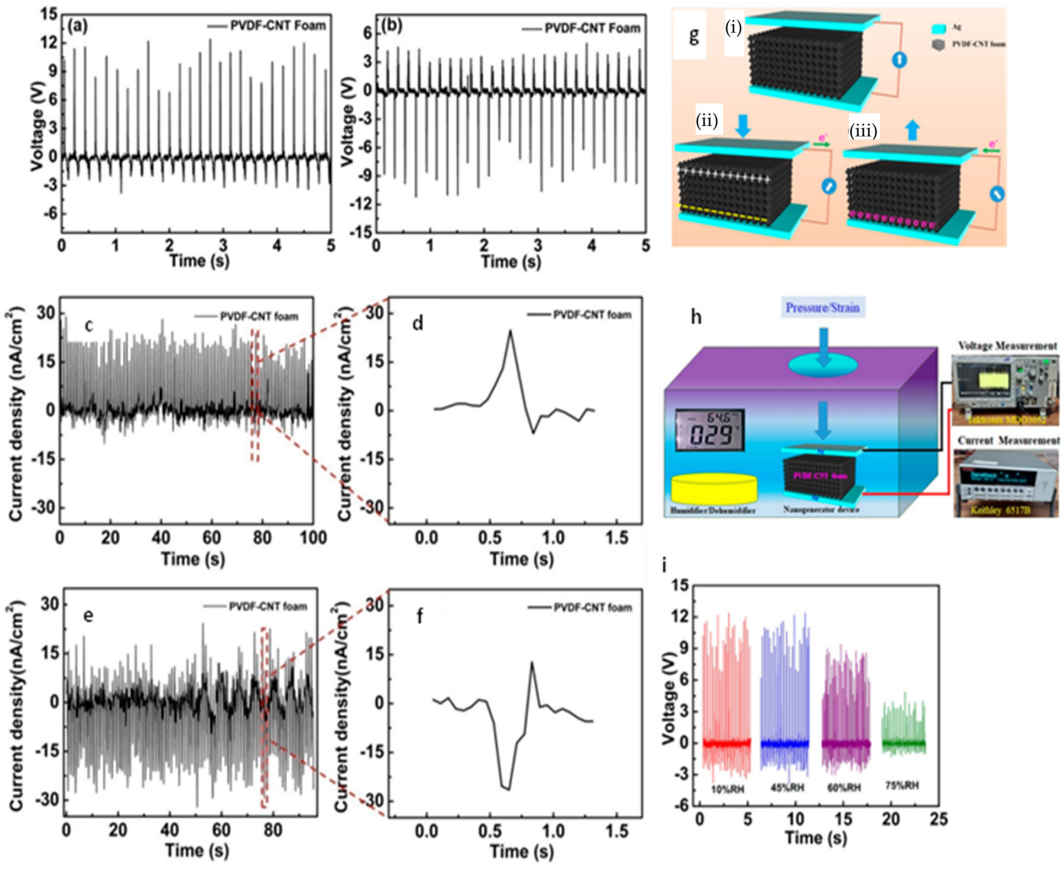


Figure 12. Output voltage of nanogenerator measured under (**a**) forward condition (**b**) reverse condition; output current of nanogenerator measured under (**c**) the forward condition and (**e**) reverse condition; (**d**) enlarged view of output signals measured under forward condition; (**f**) enlarged view of output signals measured under reverse condition; (**g**) working mechanism of piezoelectric charge generation of nanogenerator; (**h**) setup for measuring the output performance of PVDF-CNT device under controlled humidity; (**i**) output voltage of the PVDF-CNT foam based nanogenerator measured at different humidity levels reproduced with permission from [77], American Chemical Society, 2021.

3.4. Nanoparticles

Nanoparticles can also be used to create PENG nanoparticles (NPs). Recently, high-performance piezoelectric nanogenerators were created using poly (vinylidene fluoride) and lead formamidinium halide-based perovskite nps ($FAPbBr_3$-NPs @ PVDF) [78]. Figure 13a shows the fabrication process of $FAPbBr_3$ NP@PVDF composite nanogenerators. Thermal annealing can be used to create PVDF films with $FAPbBr_3$ NPs. A composite nanogenerator based on $FAPbBr_3$ NPs @ PVDF finger vents is depicted in Figure 13b, illustrating its remarkable flexibility and adaptability for integrated and wearable electronics. A schematic of the developed piezoelectric nanogenerator using a $FAPbBr_3$ NP @ PVDF composite is shown in Figure 13c. It is placed between two Au/Cr-coated PET films that serve as electrodes. The piezoelectric distribution inside the composite nanogenerator is calculated using the finite element method of the COMSOL simulation software. Three layers make up the simulation model. The top and bottom two Au/Cr-coated PET sheets act as electrodes, with the $FAPbBr_3$ NP @ PVDF composite layers being scattered at random. Figure 13d shows the scanning results of $FAPbBr_3$ NPs with electrode-coated PVDF. Composite-based $FAPbBr_3$ NP @ PVDF piezoelectric nanogenerators exhibited an output voltage of 30 V and a current density of 6.2 μA/cm at an applied voltage of 0.5 Mpa and a frequency of 5 Hz when they were subject to periodic compression and release obtained by measurement using a force simulator shown in Figure 14a. To confirm that the generated output signal is the result of the piezoelectric effect, a switching polarity test is carried out. When linked in forward mode, the nanogenerator produces a signal that is positive. Similar to forward mode, reverse mode records the negative output, as seen in Figure 14b. Similarly, lead-free $(1 - x)$ $KnaNbO_3$-x $BaTiO_3$ NPs (x = 0.02, 0.04, 0.06, and 0.08) (used as KNN-x BTO) nanoparticles (NPs) were used to construct a membrane-based flexible piezoelectric nanogenerator [79]. Figure 15a shows a diagram of a composite piezoelectric nanogenerator (PCNG). Figure 15a(i) displays the morphological structure of the prepared composite. The thickness of the prepared composite film encroached into the PDMS matrix is shown in Figure 15a(ii), and the digital images of the PCNG specimen and operating mechanism are displayed in Figure 15a(iii) and Figure 15b, respectively. The gadget develops a potential difference between the two electrodes when a vertical push is applied because the electric dipoles align in the same (single) direction. As a result, as shown in Figure 15b(i), electricity travels through an external circuit from top to bottom. As depicted in Figure 15b(ii), when the force is removed, the electric dipole is inverted, and the current flow is reversed. PCNG produces a maximum output of 58 V, 450 nA. Figure 15c,d shows the output voltage and current for KNN, KNN-0.02 BTO, and BTO NPs, with the maximum output being represented by KNN-0.02 BTO NP. Figure 15e shows a comparison of the electrical output of PCNG devices. The doped PCNG device, PCNG2 (KNN-0.02 BTO), shows the greatest performance compared to other undoped (pure) PCNG devices, i.e., PCNG 1 (KNN), and other doped devices, i.e., PCNG3 (KNN-0.04 BTO), PCNG 4 (KNN-0.06 BTO), and PCNG 5 (KNN-0.08 BTO). This finding suggests that such a system might be helpful for identifying sleep disorders and might represent an evolution in mobile health surveillance.

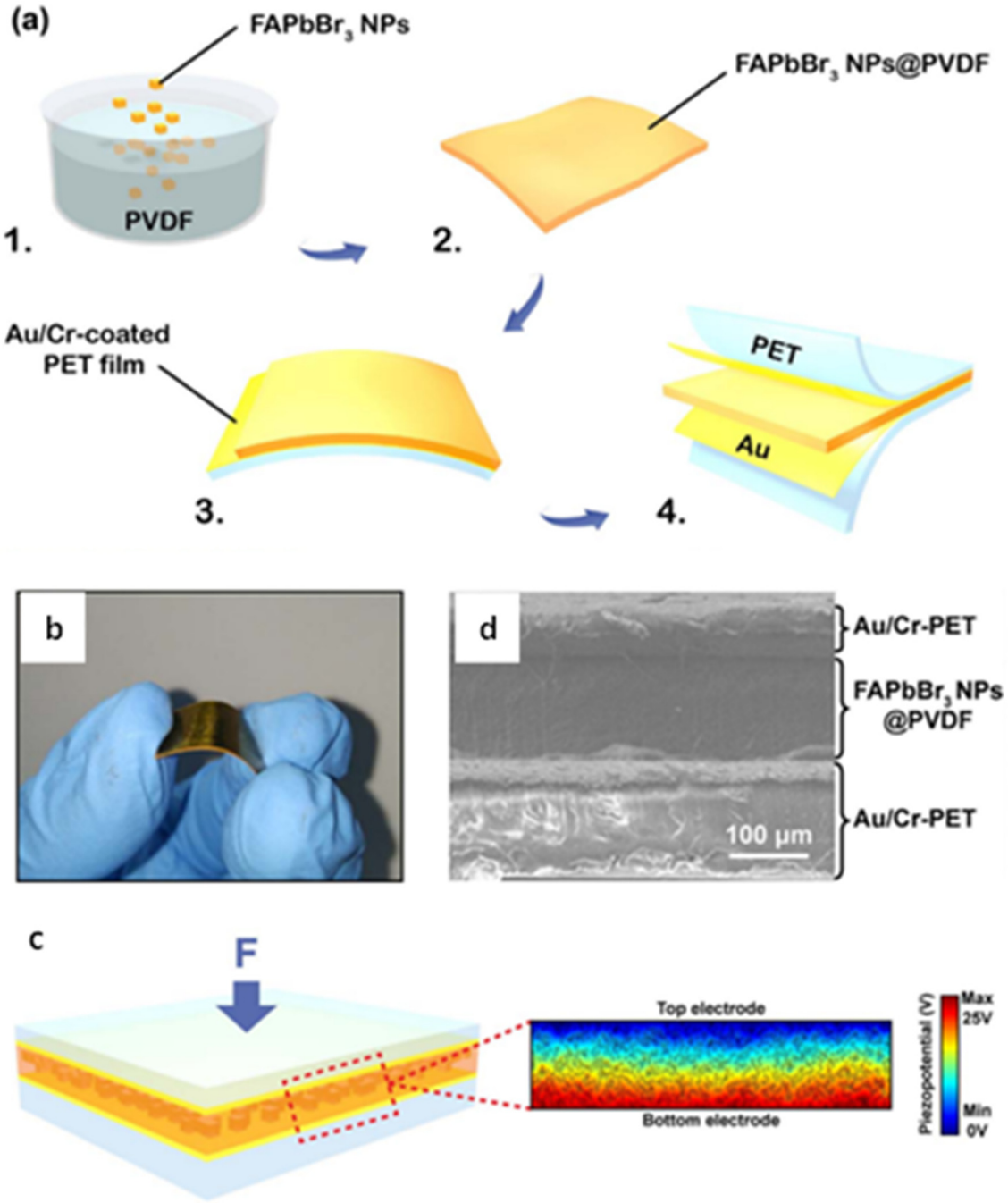


Figure 13. (**a**) Schematic diagram of the fabrication process of $FAPbBr_3$ NPs @ PVDF composite-based nanogenerators; (**b**) picture of nanogenerator bent by finger showing its flexibility; (**c**) diagram of the structure of $FAPbBr_3$ NPs @ PVDF composite-based nanogenerator sandwiched between two Au/Cr coated PET films acting as electrodes, and the piezo potential distribution inside the nanogenerator is specified by the color code; (**d**) nanogenerator SEM image reproduced with permission from [78], Elsevier, 2017.

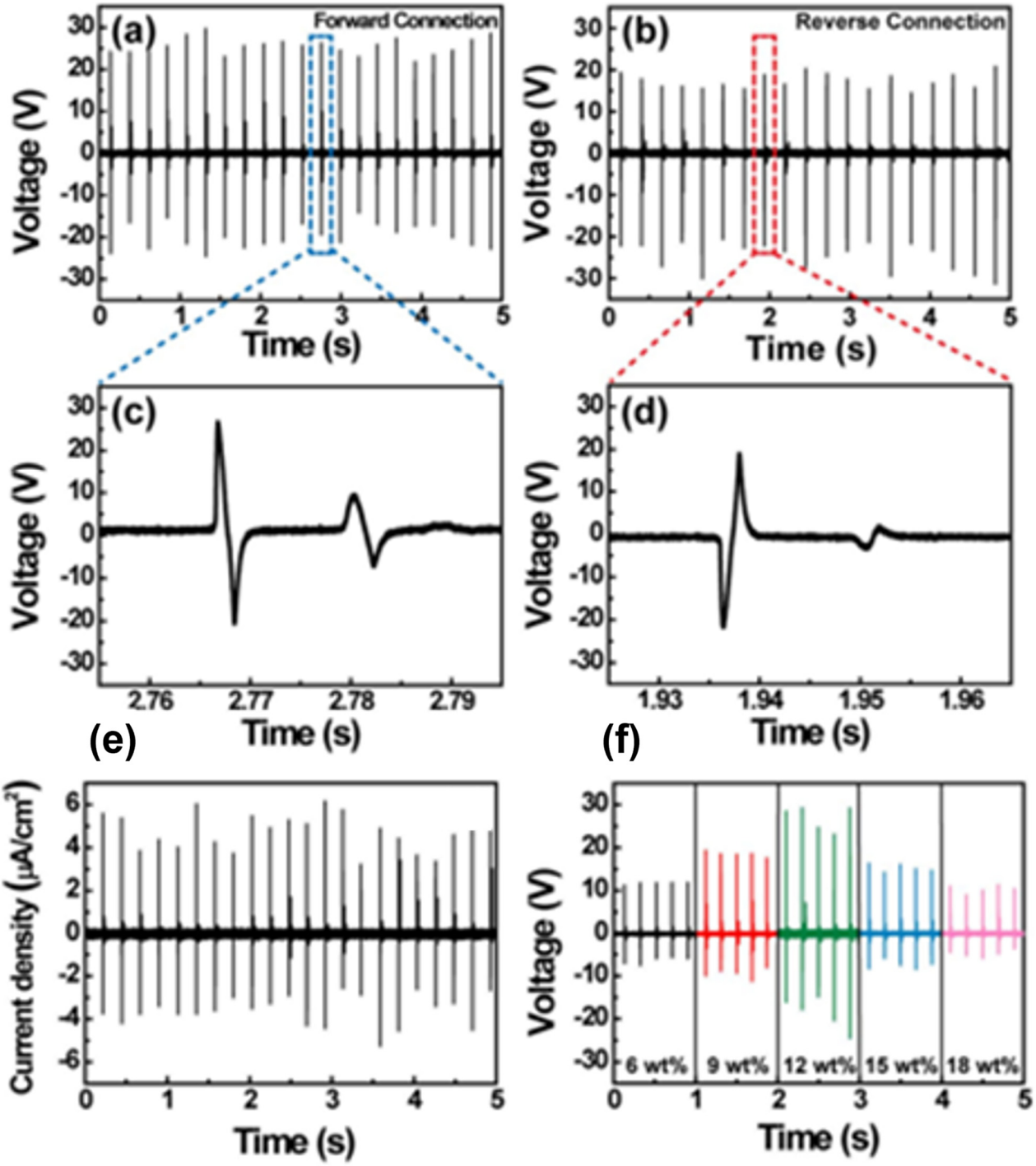


Figure 14. Output voltage of $FAPbBr_3$ NPs @ PVDF composite-based piezoelectric nanogenerator (**a**) in forward connection (**b**) in reverse connection; (**c**,**d**) enlarge views of output voltage for one cycle for forward and reverse connection respectively (**e**) output current density of $FAPbBr_3$ NPs @ PVDF composite-based piezoelectric nanogenerator (**f**) output voltage of nanogenerator with different concentrations reproduced with permission from [78], Elsevier, 2017.

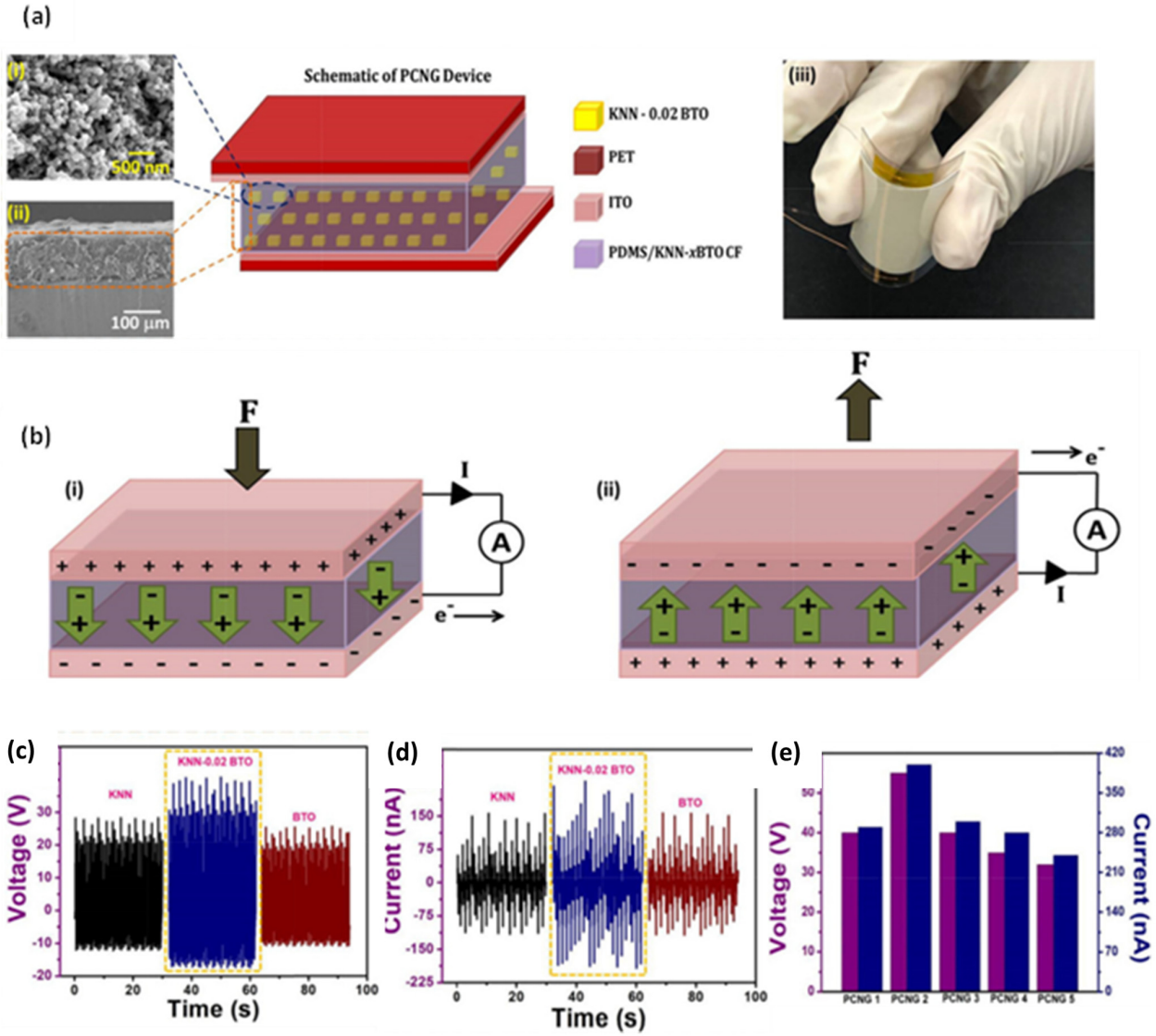


Figure 15. (**a**) Schematic diagram of the PCNG device (**i**) morphology of the manufactured nanoparticle (**ii**) thickness of the composite film (**iii**) digital image of the PCNG device; (**b**) PCNG device working mechanism; (**c**) output voltage of the PCNG device; (**d**) output current of the PCNG device; (**e**) output comparison of the PCNG devices reproduced with permission from [79], Elsevier, 2019.

3.5. Thin Films

Thin films are another significant structure of PENG [80]. Newly, an increased flexible nanogenerator relying on a composite thin film made of poly (vinylidene fluoride-co-hexafluoropropene) P(VDF-HFP) and hemispherical clustered $BaTiO_3$ nanoparticles (NP) has been developed [81]. By evaporating solvents containing tetragonal BTO-NP, P(VDF-HFP), dimethylformamide (DMF), and acetone, the composite thin film was created. A schematic representation of the device manufacturing process is shown in Figure 16. A silicon substrate is shown in Figure 16a. Following the solvent evaporation of the spin-coated solution, a BTO-P(VDFP-HFP) composite thin film was cured in an incubator at 80 °C for 1 h under ambient circumstances. During the curing process, clusters develop. Following a high-field poling procedure, the subsequent composite thin film is peeled off from the Si substrate containing BTO clusters, as shown in Figure 16c. Finally, the top and bottom of the thin composite layer were enclosed by the coated PDMS before the spin-coated PDMS cured, coated metal electrodes AI on the polyimide (PI) film, as illustrated in Figure 16d,e. Figure 16f illustrates the flexibility of the device by providing an optical view of the manufactured nanogenerator in its bent condition. Piezoelectric potentials were

produced for two distinct BTO NP topologies using the simulation tool COMSOL. One is the hemispherically packed BTO clusters (Figure 17a), and the other is the planar distribution of the lower region depicted in Figure 17b. In both simulations, the same number of BTO-NPs were employed. At a force applied of 0.23 Mpa, the flexible nanogenerator displays an open-circuit voltage of 75 V and a short-circuit current of 15 A, highlighting the significant significance of the hemispherical BTO clusters and producing enough power to turn on light-emitting diodes (LEDs). A PDMS layer increases the output power. To verify the reliability of the output signal, a switching polarity test was run. In this test, the nanogenerator was measured in two different modes. Figure 17c shows the nanogenerator measured in forward link mode, and Figure 17d shows the nanogenerator measured in reverse link mode. The output signal in reverse link mode is the same as in forward link mode; only the polarity of the signal is reversed. Furthermore, the durability and reproducibility of the nanogenerator were tested, which produced an output of ~5 V and ~750 nA, by repeated bending tests during the bending stage shown in Figure 17e. Similarly, another $BaTiO_3$ piezoelectric thin film was deposited on a plastic substrate to show a direct piezo effect [82]. The manufacturing of flexible $BaTiO_3$ nanogenerators on plastic substrates is depicted in Figure 18a. On $Pt/Ti/SiO_2/(111)Si$ substrates, perovskite ceramic $BaTiO_3$ thin films were formed by RF magnetron sputtering, crystallized at 700 °C, and poled to enhance piezoelectric characteristics. The $BaTiO_3$ thin film was then printed using soft lithography and nanofabrication techniques onto a substrate material and linked with electrodes. Figure 18b depicts the SEM image of the $Au/BaTiO_3/Pt$ layers on the SiO_2/Si substrate that make up the metal-insulator-metal (MIM) structure. The spectrum of an annealed $BaTiO_3$ thin film, which includes Ba, Ti, O_2 and tiny C peaks, is shown in the inset. The SEM image of the MIM structure ($Au/BaTiO_3/Pt$) shown in Figure 18c was created after the underlying Si layer was anisotropic ally etched with 5% tetramethylammonium hydroxide (TMAH) at 80 °C for 12 min. The inset is the scanning image of the MIM structure partially supported by the Si substrate during etching (corresponding to Figure 18a(ii)). According to Figure 18a(iii), the image in Figure 18d demonstrates that the MIM structure (about 1 cm^2) was effectively transferred from the bulk Si wafer to the PDMS stamp without fractures. The images of the twisted PDMS stamp and the top view of the MIM structure of the PDMS stamp are shown in the insets at the top and bottom, respectively. A flexible $BaTiO_3$ nanogenerator with an area of 82 mm^2 and a filling factor of 16.4% is depicted in Figure 18e (equivalent to Figure 18a(iv)) on a plastic substrate. To measure the output voltage and current, silver (Ag) paste was used to affix copper (Cu) wires to metal plates. The top and bottom electrodes of the MIM structure that are connected to the IDE are visible in greater detail in the inset (Au). Figure 19a (i,ii) shows the flexible $BaTiO_3$ nanogenerators before bending to the original state. Due to polarization in the initial condition of high electric fields without bending, piezoelectric materials have longitudinally oriented dipoles. Figure 19a (iii,iv) shows a flexible $BaTiO_3$ nanogenerator in a bent state. In the bent state, the longitudinal and compression stresses caused by device deflection generate charges in the MIM structure. The charge then passes into the Au electrodes, generating an output voltage (ΔV) across the IDE. Figure 19b,c shows the output voltage (right ii) and output current (left i) of flexible $BaTiO_3$ nanogenerators on plastic substrates in bent and unbending states. To verify that the output signal was produced by bending the MIM structure, a switching polarity test is done. According to Figure 19b, a positive voltage and current were produced during the forward connection. Negative voltages and currents for reverse connections were noted (according to Figure 19c). When circularly deformed by a bending stage, a $BaTiO_3$ flexible nanogenerator built on a plastic substrate can provide an output voltage of 1.0 V, an output current signal of 26 nA, an output current density of 0.19 A/cm^2, and a power density of about 7 mW/cm^3. The findings demonstrate that flexible displays can be powered by mechanical motion using nanogenerators for future technologies. Key Highlights of the recent progress on piezoelectric energy harvesters' designs are shown in Table 2.

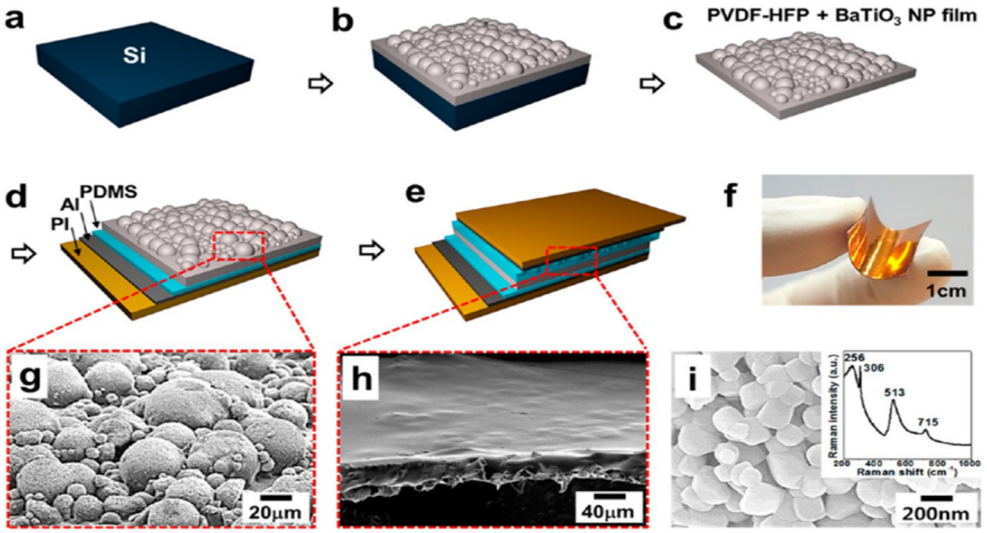


Figure 16. (**a**–**f**) Fabrication process of the BTO NPs schematic diagram; (**g**) SEM of the BTO-P(VDF-HFP) composite film consisting of BTO clusters; (**h**) SEM image of the PDMS-covered BTO-P(VDF-HFP); (**i**) Raman spectrum of the BTO NPs showing BTO NPs have a tetragonal phase, and high piezoelectric coefficient reproduced with permission from [81], American Chemical Society, 2014.

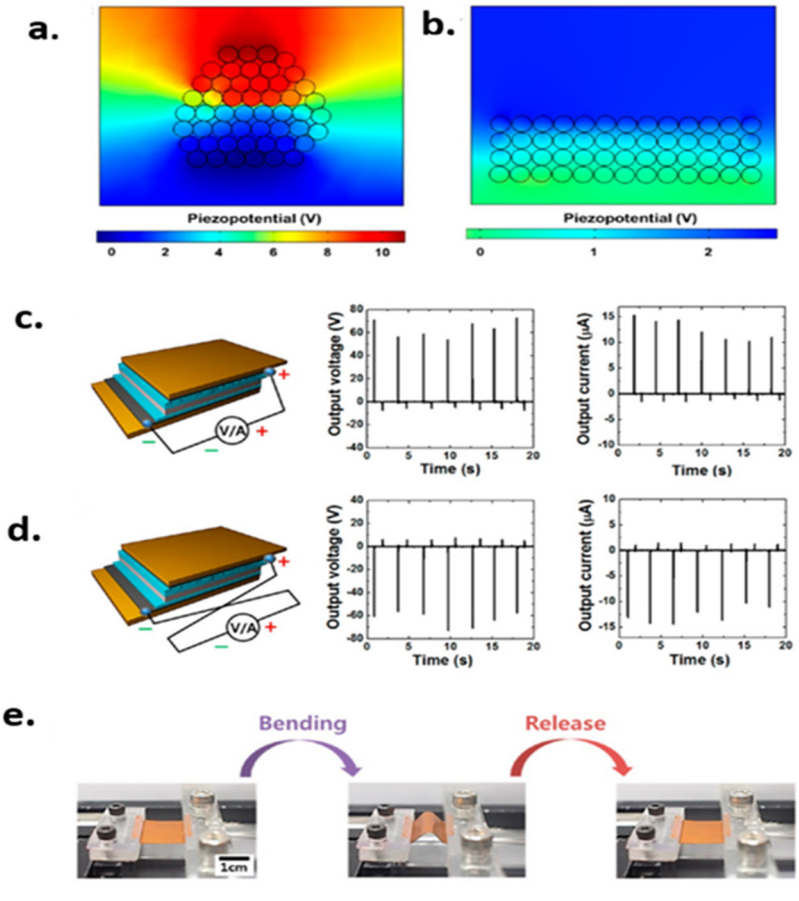


Figure 17. Simulated piezoelectric potentials for BTO NP in (**a**) distribution pattern as a hemispherical cluster, (**b**) planner distribution at the bottom; switching polarity test (measure open circuit voltage and short circuit current) in (**c**) forward connection mode and (**d**) reverse connection mode; (**e**) photograph of the nanogenerator in the bending and releasing states reproduced with permission from [81], American Chemical Society, 2014.

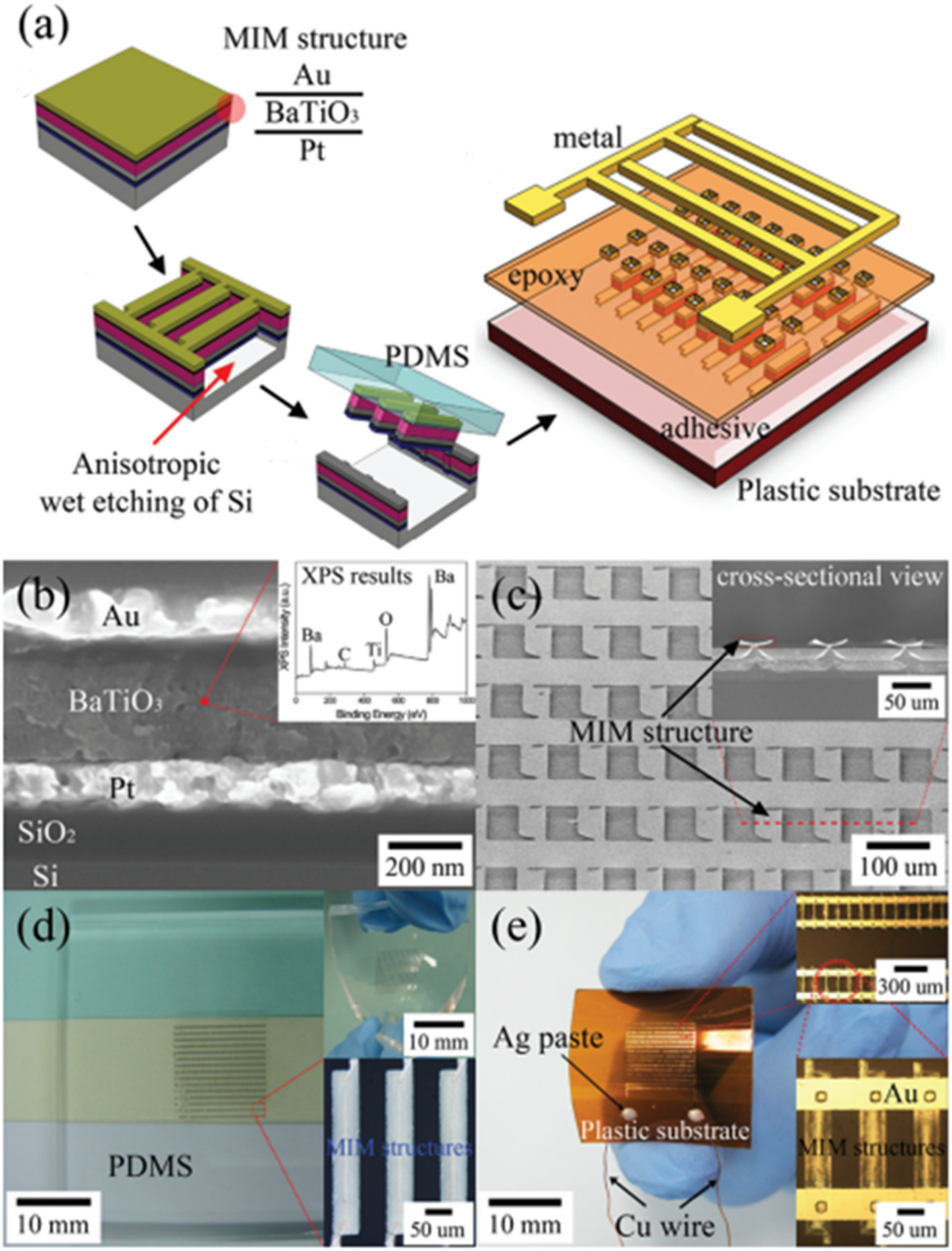


Figure 18. (**a**) Diagram of a flexible $BaTiO_3$ nanogenerator fabrication process; (**b**) SEM image of MIM structure ($Au/BaTiO_3/Pt$ layers); (**c**) SEM image of the MIM structure ($Au/BaTiO_3/Pt$) after anisotropic etching of the Si layer. The inset is a magnified cross-sectional view of the MIM structures; (**d**) a magnified image of a PDMS slab inked with MIM structure. The inset shows the MIM structure (300 μm × 50 μm) was successfully transferred onto the elastomer; (**e**) magnified optical image of the flexible $BaTiO_3$ nanogenerator supported on the plastic substrate after the PDMS was removed. The inset shows the image of the MIM structure connected to the IDEs reproduced with permission from [82], American Chemical Society, 2010.

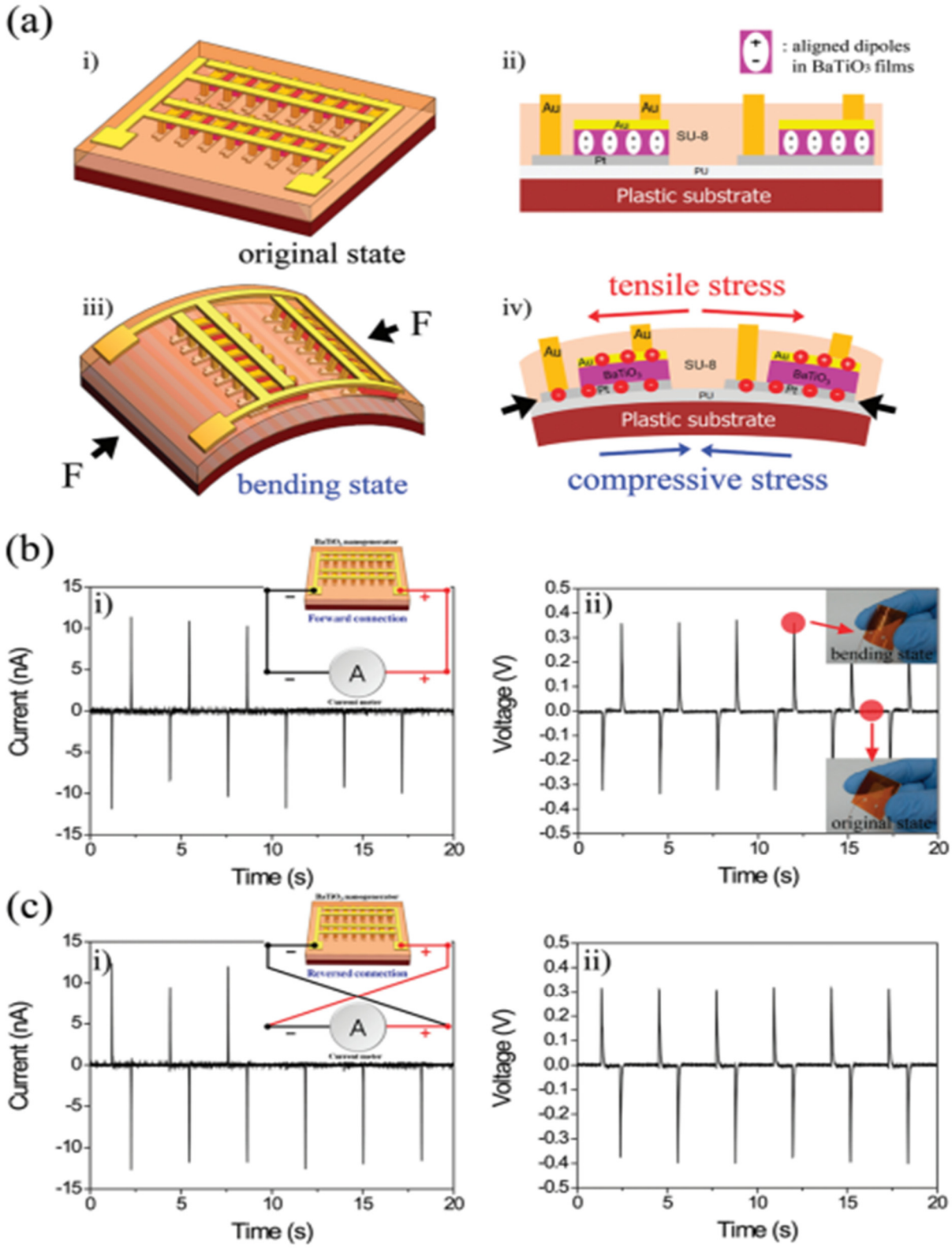


Figure 19. (**a**) Schematic diagram of the power generation of the flexible $BaTiO_3$ nanogenerator in unbending (**i**,**ii**) and bending (**iii**,**iv**) states; measured output voltage (**right ii**) and output current (**left i**) of the flexible $BaTiO_3$ nanogenerator during bending and unbending (**b**) when forward connected (**c**) when reverse connected reproduced with permission from [82], American Chemical Society, 2010.

The roadmap and factors for the performance improvement of the piezoelectric nanogenerator from μW to mW to W are shown in Figures 20 and 21, respectively.

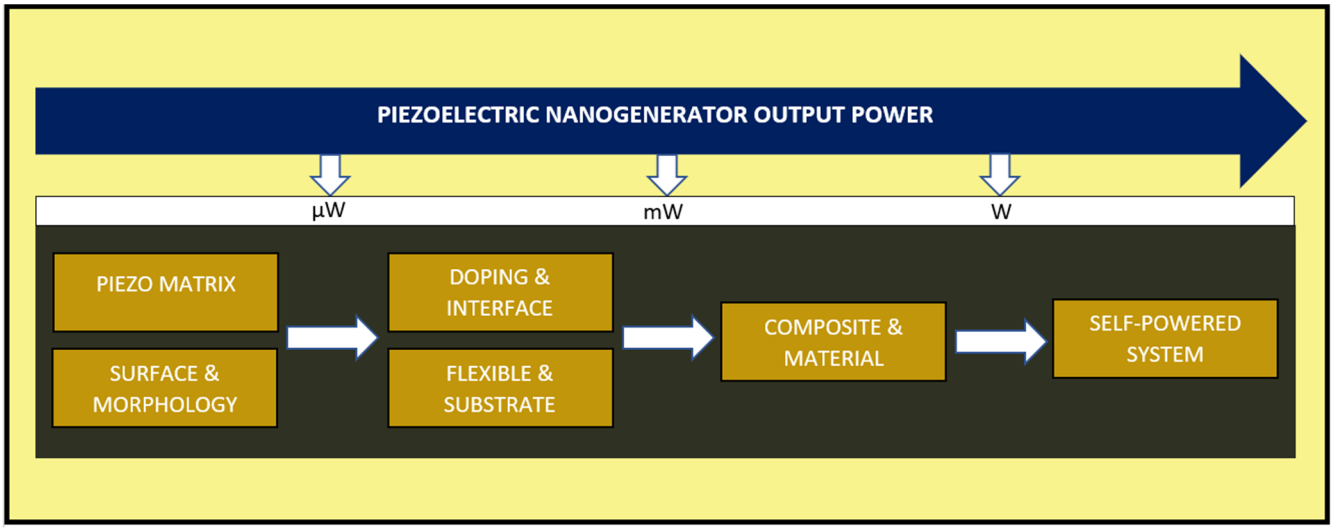


Figure 20. Road map for improving the output performance of piezoelectric nanogenerator from μW to mW to W.

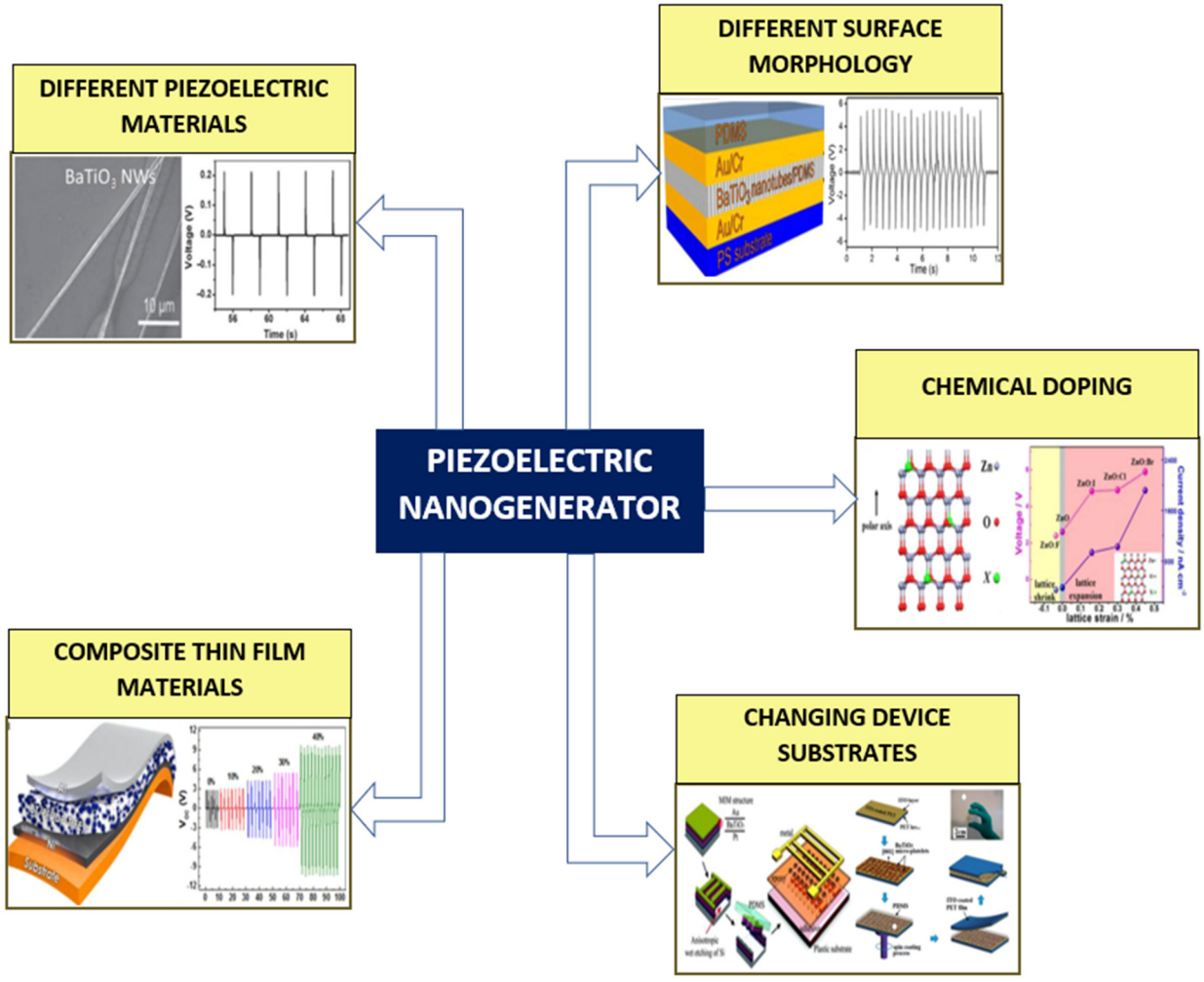


Figure 21. Factors to improve the output performance of piezoelectric nanogenerator.

Table 2. Overall review papers on the PEH design.

Author	Accomplishments	Subdivisions	Highlights	Conclusion	References
Uchino	Considering the energy conversion efficiency, the PHE's output power, the coupling coefficient, and the operating mode, including a mathematical model to match the PHE's resonant frequency to the driving frequency, was reported	Piezoelectric materials and their selection criteria, thin PEH, energy conversion efficiency, mathematical modeling of PEH, piezoelectric basins, improved piezoelectric cantilever design, electrode optimization, PEH electronic interfaces and power storage circuit, power quantification and comparison strategies, hybrid energy harvesting mechanism	Explanation of the background of PEH, condemnation of various researchers' misconceptions, a thorough examination of the energy flow in the energy harvesting system, a description of the methods for greatly enhancing efficiency, and helpful/significant comment regarding harvester output that is not useful	Importance of storage circuits and electric interface circuits	[83]
Priya	Considering the energy conversion efficiency, the PEH's output power, the coupling coefficient, and the operating mode, including a mathematical model to match the PEH's resonant frequency to the driving frequency, was reported	Piezoelectric materials and their selection criteria, thin PEH, energy conversion efficiency, mathematical modeling of PEH, power storage circuits of PEH, and electronic interfaces	Explains the criteria for choosing materials in on- and off-resonance situations. Explanation of the variables influencing PEH conversion efficiency. A number of low-profile PEHs are being used to create self-powered sensor nodes	Improvement of the material properties and material selection strategy	[84]
Yang et al.	Report the operating mode, coupling coefficient, and the mathematical model used to align the PEH's resonant frequency with the drive frequency for energy conversion efficiency	Nonlinear systems, mathematical modeling of PEHs, geometric optimization, improved piezoelectric cantilever design, piezoelectric stack configurations, piezoelectric basins, electrode optimization, comparative strategies, and power quantification	Evaluation of different designs, nonlinear approaches, optimization techniques, and materials to increase performance. Introducing the set of indicators to compare PEH performance	Importance of storage circuits and electric interface circuits	[85]
Li et al.	Considering the energy conversion efficiency, the PEH's output power, the coupling coefficient, and the operating mode, including a mathematical model to match the PEH's resonant frequency to the driving frequency, were reported.	Manual frequency tuning, frequency up-conversion approach, piezoelectric material and its selection criteria, mathematical modeling of PEH, improved piezoelectric cantilever design, piezoelectric basin, piezoelectric stack configuration, electronic interface, and power storage circuit for PEH	A discussion of the main challenges of PEHs and an explanation of the main limitations of piezoelectric materials	Importance of storage circuits and electric interface circuits	[60]

Table 2. *Cont.*

Author	Accomplishments	Subdivisions	Highlights	Conclusion	References
Talib et al.	A discussion of the main challenges of PEHs and an explanation of the main limitations of piezoelectric materials	Nonlinear systems, two-way and three-way systems, geometric optimization, design improvements for piezoelectric cantilevers, hybrid energy harvesting mechanisms, piezoelectric materials and their selection criteria	Finding a balance between the bandwidth and the output power will enable piezo harvesters to perform as expected	Importance of storage circuits and electric interface circuits	[86]
Ibrahim and Wahied	Report on the power output of PEH, including a mathematical model that matches the resonance frequency to the driving frequency	Manual frequency adjustment, autonomous frequency adjustment, mathematical modeling of PEH	Review, comparison, and classification of several autonomous and manual tuning methods. Addressing the challenges of energy consumption	Importance of storage circuits and electric interface circuits	[87]
Liu et al.	Considering the energy conversion efficiency, the PEH output power, the coupling factor and the mode of operation. This includes a mathematical model to match the PEH's resonant frequency to the driving frequency that was reported	Multi-frequency systems, frequency up-conversion approaches, non-linear systems, bi-directional and tri-directional systems, mathematical modeling of PEHs, piezoelectric materials and their selection criteria, improved piezoelectric cantilever design, piezoelectric stack configurations, piezoelectric basins, hybrid energy harvesting	Describes various important aspects of improving the overall performance of PEH devices. Classification of performance improvement approaches	Increasing endurance and lifetime of PEHs and their manufacturability, size reduction, and packaging	[64]
Yildirim et al.	Report of PEH output power, including mathematical model to match PEH resonance frequency to driving frequency	Manual frequency tuning, multi-frequency system, autonomous frequency tuning, non-linear system, floating mass system, frequency up-conversion approach, bi-directional and three-way systems	A new taxonomy of performance-enhancing techniques. Comparison of many performance-enhancing techniques	Increasing the PEHs' frequency tuning and bandwidth	[88]
Maamer et al.	PEH output power report with a mathematical model that matches the PEH resonance frequency to the driving frequency and accounts for the energy conversion efficiency	Manual frequency tuning, multi-frequency systems, autonomous frequency tuning, non-linear systems, free moving mass systems, frequency up conversion approaches, piezoelectric materials and their selection criteria, two-way and three-way systems	A proposal for a new general classification using approaches based on aspects of harvester improvement, such as techniques for extending operating frequencies, design of non-resonant systems, and multi-directional harvesters. Evaluation of applicability and compatibility with MEMS technology of performance improvement technology under various conditions	Increasing the PEHs' frequency tuning and bandwidth	[89]

Table 3 presents the properties of some basic piezoelectric materials in terms of their stress and strain constants, charge constants, coupling factor, mechanical quality factor, voltage constant, and curie temperature. PZN-PT and PMN-PT single-crystal structures exhibit great electromechanical properties as compared to PZT ceramics [89]. Due to the enhanced piezoelectric properties and high Curie temperatures, solid solutions of lead titanate and bismuth-based oxides have a wide range of possible applications. Compared to the other materials, ZnO and AIN have a lower piezoelectric effect. Mostly, they are used in thin-film structures at the micro-scale, where their performance metrics differ from that of the bulk materials. In general, we find that d15 >> d33 > d31, as indicated in Table 3. The maximum piezo-electric properties are displayed by the PMN-PT and PZN-PT. However, they are highly sensitive to temperature changes and more challenging to fabricate than the PZT. As a result, PZT is the most widely used piezo-electric material in energy harvesters.

Energy harvesters could be divided into two operation modes: d31 and d33, depending on the polarization and stress directions. In d31 mode, the electric field's direction, "3," is perpendicular to applied stress "1". In contrast, in d33 mode, the polarization and applied stress are both in the same direction. Electrodes are positioned perpendicular to the poling direction in both d31 and d33 modes. The shear mode, which is used by several energy harvesters, requires charge constant d15 mode. The most common piezoelectric material, PZT, has a piezoelectric coefficient that is about two times that of d31. If both the modes d31 and d33 have similar design parameters, the output voltage for the d33 mode is predicted to be greater than the d31 mode energy harvester. Moreover, the distance between electrode fingers influences the voltage produced by the d31 and d33 mode devices. As the PZT layer is often very thin, so the distance of electrodes in the d31 mode is less than in the d33 mode. In terms of power output produced by the product of both voltage and current, Lee et al. discovered that the d31 mode energy harvester outperformed the d33 mode [90]. The compliance matrix, S^E, is the inverse of C^E, the stiffness matrix and is measured under the constant electric field. There are 10 independent matrix elements for the frequently used poly-crystalline ceramic materials, i.e., PZT. Ideally, under low electrical field and stress, and for the material having low losses, these ten constants include all the information necessary to determine how the material will behave when an electrical field, stress or strain is applied to it. If stiff piezo ceramics are attached directly to the vibration host, they are unable to absorb much mechanical energy. The solution to this is to install the piezo-electric element on the flexible beam structure. The most frequently utilized structure is the cantilever. Around the high-stress end, the sub-structure is usually covered with one (unimorph) or two (bimorph) piezo-electric elements and frequently attached with tip-mass to reduce the resonant frequency and enhance the vibration-induced stress.

Table 3. Properties of some basic piezoelectric materials.

Piezoelectric Materials	Const. Strain (*S*)	Const. Stress (*T*)	Charge Constant (d_{15} pC/N)	Charge Constant (d_{31} C/N)	Coupling Factor (k_{33})	Mechanical Quality Factor (*Q*)	S^E_{11} (p/Pa)	S^E_{33} (p/Pa)	Voltage Constant (g_{31} 10^{-3} Vm/N)	Curie Temperature (°C)	References
PZT-4H	635	1300	495	-1.23×10^{-12}	289	500	12.3	15.5	-	328	[90]
PZT-5H	1470	340	741	-274×10^{-12}	593	65	16.4	20.8	-	193	[90]
α-quartz	4.63	4.63	-	-	-	10^5–10^6	12.8	9.72	-	-	[91]
$BaTiO_3$	910	1200	242	-158×10^{-12}	149	400	8.6	9.1	-	115	[49,90]
PMN-PT	680	8200	146	-1320×10^{-12}	2820	43–2050	69	119.6	-	-	[49,92,93]
PVDF	5–13	7.20	−27	21×10^{-12}	−33	3–10	365	742	-	100	[94,95]
$LiNbO_3$	27.9	28.7	69	-1.0×10^{-12}	6	10^6	5.83	5.02	-	-	[91,96]
ZnO	8.84	11.0	−8.3	-5.0×10^{-12}	12.4	1770	7.86	6.94	-	-	[90,91,93,96–98]
AIN	10	11.9	3.2	-2×10^{-12}	5	2800	2.85	2.824	-	-	[93,95,99,100]
GaN	11.2	-	3.1	-1.9×10^{-12}	3.7	2800	3.23	2.91	-	-	[95,100–102]
CdS	9.53	10.33	−13.9	-5.18×10^{-12}	10.3	1000	20.69	16.97	-	-	[103]
PZT (I) BM 400	-	-	-	-115×10^{-3}	-	500	-	-	−10.5	350	[9,102]
PZT (II) BM 500	-	-	-	-165×10^{-3}	-	80	-	-	−11.5	360	[9,102]
PZT (III) BM 800	-	-	-	-80×10^{-3}	-	1000	-	-	−10.5	325	[9,103]
PZT (VI) BM 532	-	-	-	-250×10^{-3}	-	70	-	-	−7.5	210	[9,103]
PZT-5A	-	-	584	-171×10^{-12}	0.71	75	-	-	−11.4	365	[104]
PZT-8	-	-	330	-97×10^{-12}	0.64	1000	-	-	−11	300	[104]
PMN-33%PT	-	-	-	-920×10^{-12}	0.93	69	-	-	−17.1	145	[104]
PZN-6%PT	-	-	-	-1400×10^{-12}	0.9	-	-	-	24.3	100	[104]

4. Applications of Piezoelectric Materials in Analytical Chemistry

Piezoelectric energy harvesters have recently been used in a variety of applications. They are also used in analytical chemistry for the detection and determination of various substances [105–110]. Below are several applications of piezoelectric crystal detectors in analytical chemistry.

4.1. Sorption Detector

King [111] constructed a selective and sensitive detector for gas chromatography using coated piezoelectric crystals. It is simple to measure the vibrating crystal's frequency within 1.0 Hz., and momentous changes can be easily detected. King has shown that various substrates used in gas chromatography columns are coated with crystals and are in contact with the chromatographic components of the stream. The mass of the vapors absorbed by the coating influenced the frequency of the crystal. Also, the carrier gas has no effect on the detection limit. As a result of the combination between absorption and adsorption, King termed this device a Piezoelectric Sorption Detector. Because of its high sensitivity and selectivity, it is applicable to be used in analytical chemistry.

4.2. Piezoelectric Crystal Detector for Water

A wide range of materials can be used to make water vapor detectors [112]. Since 1964, hygroscopic crystal has been used as a water detector. With its high selectivity and long life, this device can detect ppm water in 30 s. Gjessing et al. have created a radio sonic element having a film of SiOx deposited over a piezoelectric crystal. Between 15 and 95 percent relative humidity, there was no hysteresis. Several studies have shown that piezoelectric crystal detectors can also be used to determine the amount of water in the Martian atmosphere. The atmosphere on the surface of Mars is different compared to that on Earth. Mariner flyby showed that the Martian atmosphere consists of 80% of carbon dioxide, with a total pressure of 6–8 mbar. There is evidence that water vapor pressure in the atmosphere of Mars ranges from 50 mm to 0.9 mm. Under these adverse conditions, King's piezoelectric sorption hygrometers have been used to measure water vapor concentrations. Water was measured under various experimental conditions (temperature, pressure, etc.) [106–108]. Water measurement is an indicator that describes the level of hydration and water binding in a certain substance. Therefore, measures of water activity have great potential for technological use. In 2021 Agafonov et al. provided a technique for measuring water activity using a piezoelectric quartz crystal sensor covered with a porous layer of alumina. By injecting the air with the appropriate humidity in the vessel containing the resonator, it was possible to evaluate how the piezoelectric crystal's frequency varies with respect to the relative humidity. The observed dependence was changed into the water sorption isotherm on the alumina. The water adsorption onto the pores wall of anodic oxide is enhanced by the presence of sulfate ions, which are the hydrated ions [113]. In order to address the global issue of sustainable access to water, Okosun et al., in 2021, developed an amino acid-based detector that is capable of detecting pipe leaks, Figure 22. The polycrystalline system uses the correlation between the piezoelectric voltage and the leak-induced vibration to detect pipeline degradation. The voltage constant and the piezoelectric strain for this device are 60 mV m/N and 0.9 pC/N, respectively. Compared to the PVDF patches, the crystal sensor of glycine has substantially higher sensitivity [114].

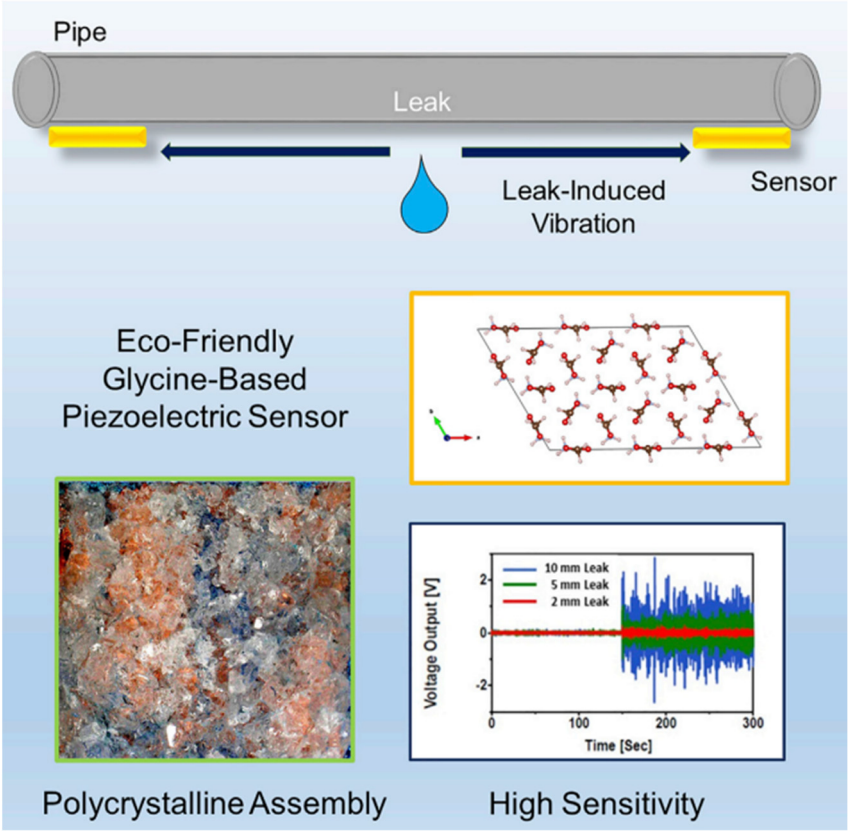


Figure 22. Amino acid-based detector for the detection of pipe leaks developed by Okosun et al. [114].

4.3. Detector for Gas Chromatography

With gas chromatography, the more sensitive flame ionization detector or thermal conductivity detector is used the most. Mass spectrometry and electron capture have been used to create more sophisticated detection methods. King and Karasek et al. [115,116] established a low-cost system of gas chromatography that is based on a piezoelectric crystal detector. The crystals were covered with the liquid that is used in the gas chromatography column. The compounds which are separated are detected by passing them onto the surface of a coated piezoelectric crystal, where the compound disperse within the coating of the crystal, resulting in the change in the piezoelectric crystal's resonance. The frequency shift is used as a response to the detector and is converted to a voltage. Piezoelectric detectors can be used at room temperature or above if the carrier gas is air, nitrogen, or helium. Chromatographs can be used to apply a variety of compounds with boiling temperatures up to 200 °C. Equation (3) below shows the reaction between the coated piezoelectric crystal and the elution of the compound from the column of gas chromatography:

$$A = \frac{CW}{\gamma P^{\circ} F} \tag{3}$$

Here, A represents the area of the response curve, W represents the total eluent weight, γ represents the eluent activity coefficient, P° represents eluent vapor pressure at the operating temperature, F represents the flow rate of the carrier gas, and C represents a constant which is a characteristic of the piezoelectric crystal, detector temperature, and the liquid coating over the crystal. Equation (3) describes several solvent properties of the piezoelectric crystal detectors when they are used in conjunction with the gas chromatographs. When utilizing piezoelectric crystals, the detector's temperature is crucial. When utilized above ambient temperature, the same properties, such as linearity and sensitivity, can be seen. There are variations in the separation between the compounds observed at high

temperatures because of the respective partition coefficients of the gas components. With the rising temperature, a compound's absolute detector response declines. The result is not as dramatic as predicted. For optimal detector conditions, the detector and column temperature must be maintained as low as possible while still being higher enough for the elution of the compound of interest in a sufficient amount of time [117]. Since the vapor pressure of all chromatographic separation solvents is fixed, the lifetime of the coated crystal is determined by the solvent used and the vapor pressure of the carrier from the column. Crystals coated with polymers and adsorbents have a longer service life. If the crystal detector is damaged in an accident, it can be repaired by cleaning it with a solvent or coating it with a new substance. A detector's lifetime is independent of the performance of the instrument. Janghorbani et al. [118] described a coated piezoelectric crystal's response characteristic as a distribution detector of dissolved vapors in the gas stream. The partition detector theory's authors assume that the detector is attached to the gas chromatograph column's outlet. The response of the peak area is associated with the gas mixture of the sample. The equations developed by them to describe the action of the crystal distribution detector in the gas and liquid chromatography under equilibrium conditions are shown below (Equation (4)),

$$A_y = \frac{mK_{y,x}\ V_x\ W_T}{F} \tag{4}$$

where A_y is the area below the peak caused by the y component, m represents the constant giving the change in crystal frequency caused by a mass increase at the surface, and $K_{(y,x)}$ is the partition coefficient of gas y in the liquid x, which describes the following ratio shown by Equation (5):

$$\frac{W_{y,x}}{W_y} = K_{y,x} \tag{5}$$

$W_{(y,x)}$ shows the equilibrium mass of the gas y in one unit of the crystal-coated material x, whereas W_y is the mass of the gas y in one unit of the gas phase. V_x is the volume of liquid coating x that is present on the crystal. W_T indicates the mass of the gas contained in the volume of a detector when in equilibrium with a liquid coating, and F indicates the gas phase flow rate. When squalene-coated crystals were used as a detector, an admirable linear relationship between A_y and an inserted volume of pentane, hexane, and octane was noted. Table 4 shows various coatings used with piezoelectric crystal detectors in gas chromatography. To enable in-line detection in gas chromatography, Hu et al. [119] developed a revolutionary microfluidic film bulk acoustic wave resonator gas sensor (mFBAR) in 2021, Figure 23a. The detecting element FBAR within this detector is contained within a microfluidic flow channel and operates via a desorption or adsorption mechanism. Comparative tests and computer simulations showed that adding an additional mFBAR to the capillary line (flow channel) did not significantly alter the flow or affect separation. In this system (gas chromatography-mFBAR-flame ionization detector (FID)), they showed that the simultaneous measurement of concentration profile within the mobile phase by the flame ionization detector (FID) and the direct measurement of concentration profile over the surface of the solid by mFBAR was possible. The rate of mass transfer could be easily determined by the difference between the maximum peak positions of the solid phase and the mobile phase. Figure 23b displays a 1-dimensional separation of the chromatogram for 11 gases utilizing an in-line mFBAR detector.

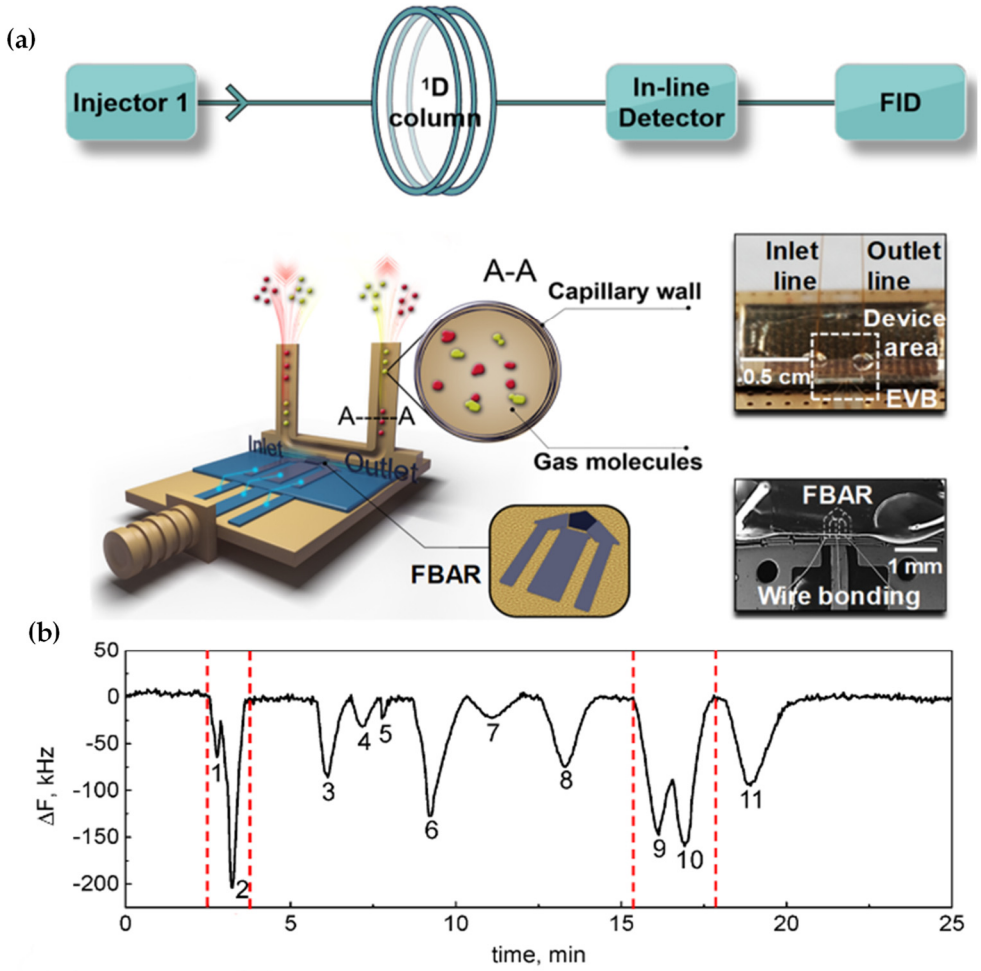


Figure 23. (**a**) mFBAR developed by Hu et al. [119]; (**b**) 1-dimensional separation of the chromatogram for 11 gases [119].

Yen et al. [120], in 2021, created an electronic nose model that is based on the surface acoustic wave to analyze the freshness and quality of the kiwifruit, Figure 24. Piezoelectric properties were displayed by $LiNbO_3$. Due to the absorption of the volatile organic compounds, the change in frequency varied based on the characteristics of different polymers. We examined the VOCs in the kiwi aroma using a thermal desorption (TD)-gas chromatograph (GC)-mass spectrometer (MS) (TD-GC-MS) system. The kiwifruit started to ripen as the esters' concentrations rose, which was followed by an increase in the concentration and the type of VOCs. As a result, ester aroma was primarily determined using fluoropolymer and polystyrene, which acted as the sensing materials. While kiwifruits were ripening, polyvinyl butyral, poly-N-vinylpyrrolidone and polyvinyl alcohol were used to extract the acids and alcohols. The frequency shift of 2510 Hz occurred from the unripe stage to the ripe stage, and the frequency shift of 4572 Hz occurred from the ripe stage to the over-ripe stage, which is best for determining the freshness of the kiwifruit and was specifically revealed by the surface acoustic wave chip that is coated with thin polyvinyl alcohol film. This is a promising technique for identification analyses and developing food quality.

Table 4. Various coatings use with piezoelectric crystal detectors in gas chromatography.

Crystal Coatings	Column Packing	Temperature (°C)	Time (min)	Carrier Gas (mL/min)	Samples	References
Squalane	Carbowax 1540, dinonyl phthalate (DNP)	62 °C	-	He	n-pentane, n-octane, n-hexane, benzene	[121]
Squalane	Squalane	27 °C	4 min	He	n-pentane, benzene, n-hexane, n-heptane, n-octane, toluene, o-xylene, ethyl benzene,	[111]
1,2,3-Tris cyano-ethoxy-propane (TRIS)	TRIS	23 °C	28 min	He	Benzene, ethyl benzene, toluene, propyl benzene, pentyl benzene, butyl benzene, heptyl benzene, hexyl benzene	[122]
OV-17	5% of OV-17 on the chromosorb W	22 °C	2.5 min	He	n-hexane 35.5 wt. %, n-octane 18.4 wt. %, n-heptane 17.9 wt. %, n-decane 9.5 wt. %, n-nonane 18.7 wt. %	[115]
Carbowax 20 M	10% of carbowax 400 on the chromosorb W	22 °C	5.5 min	He	Ethanol, Acetone, n-propanol, cyclohexanone, water	[115]
Carbowax 20 M	10% of carbowax 400 on the chromosorb W	22 °C	2 min	He	Breath containing ethyl alcohol and normal breath	[115]
Carbowax 20 M	10% of carbowax 400 on the chromosorb W	22 °C	5.5 min	He	Diethyl ketone, acetone, 2-methyl-pent-2-enol, cyclo-hexanone, n-butanol	[115]
Carbowax 400	Carbowax 400 on the chromosorb W	22 °C	7 min	Dry air	40.0% ethanol, 53.4% methanol, 6.6% propanol	[123]
OV-17	5% of OV-17 on the chromosorb W	22 °C	4 min	He	Chloro benzene, benzene, m-dichlorobenzene	[115]
Carbowax 400 (about 4 μg)	5% of carbowax 400 on the chromosorb W	25 °C	1 min	Air	SO_2 in nitrogen	[116]
OV-17 (about 4 μg)	5% of OV-17 on the chromosorb W	25 °C	14 min	Air	benzene, n-hexane, n-octane, n-decane, toluene	[116]
Rubber cement	5% of carbowax 400 on the chromosorb W	25 °C	-	-	n-decane, n-nonane, dodecane, b-undecane	[116]

Table 4. *Cont.*

Crystal Coatings	Column Packing	Temperature (°C)	Time (min)	Carrier Gas (mL/min)	Samples	References
Carbowax 400 (about 4 μg)	5% of carbowax 400 on the chromosorb W	25 °C	14 min	Air	Propyl-, ethyl-, butyl-, alcohol, amyl-	[116]
Carbowax 400 (about 7 μg)	5% of carbowax 400 on the chromosorb W	74 °C	-	Air	n-octane, n-hexane, n-dodecane, n-decane	[117]
Carbowax 400 (about 7 μg)	5% of carbowax 400 on the chromosorb W	40–100 °C	-	N_2	benzene, -n-butanol, -n-decane	[117]
Ucon LB550X (about 4 μg)	5% of Ucon LB550X on the chromosorb W	25 °C	8 min	Air	Propyl acetate, ethyl acetate, butyl acetate, hexyl acetate, amyl acetate	[116]

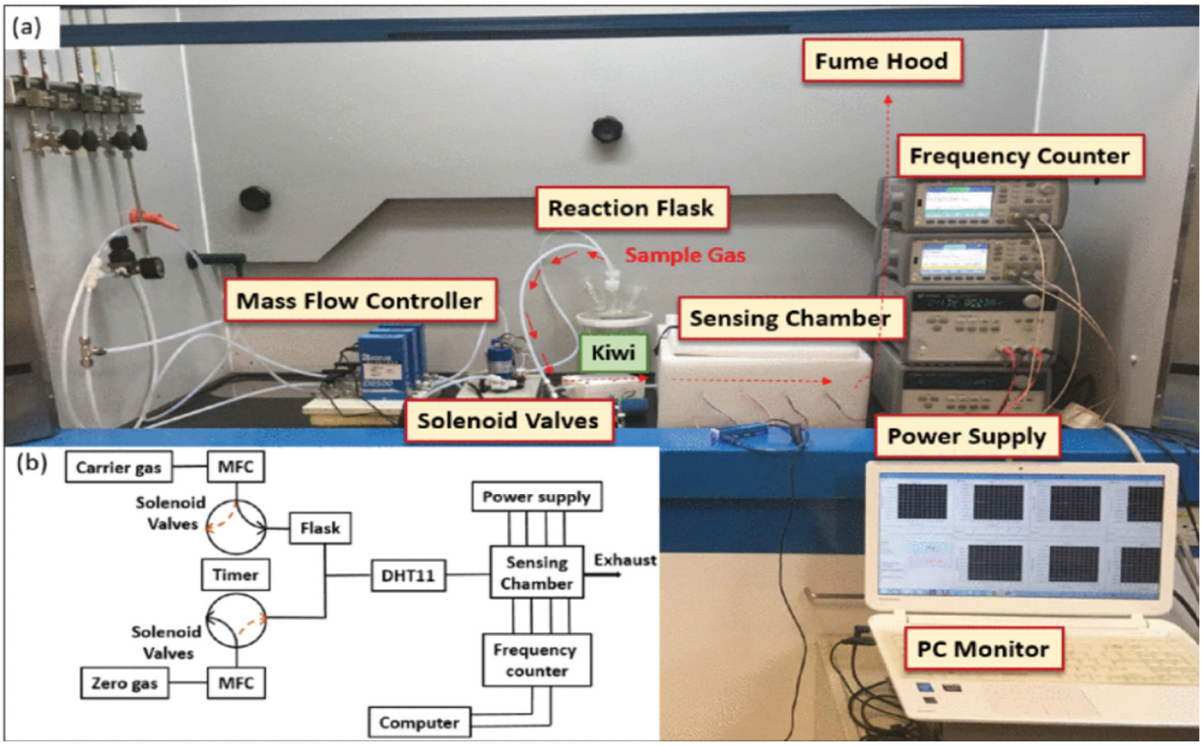


Figure 24. TD-GC-MS system, (**a**) experimental setup (**b**) schematic diagram, created by Yen et al. [120].

4.4. Detector for Liquid Chromatography

King and Schulz [124] constructed a worldwide mass detector for liquid chromatography. The effluent of the liquid chromatograph was sprinkled over the surface of the crystal. After the solvent has evaporated, the change in crystal frequency is used to calculate the mass of the remaining solute. Solute deposition and the sampling of liquid flow can be done quickly. Sensitivity was comparable to conventional liquid-liquid chromatography detectors, and nebulization, drying and measurement all took place in just 10 s. A gel transmission chromatograph differential refractometer directed the effluent to a crystal detector. A polystyrene blend was evaluated using chromatography, and the system was tested with butyl rubber. The mass versus retained volume distribution curves was compared with the results that were obtained with the differential refractometer detector. Refractometer detectors have been proven to be inferior to piezoelectric crystal detectors. The benefits listed by Schulz and King include that the method is non-destructive, highly sensitive, has a mass and universal detector, a wide dynamic measuring range, independent of changes in the chromatograph's pressure temperature or flow rate, any solvent or solute mixture can be useable, volatile impurities do not inhibit it, and it is compatible with the digital response with the digital processing equipment. For effluent detection, Bastiaans and Konash [125] placed a piezoelectric crystal detector immediately in the liquid phase. A large energy loss at the interface of the liquid crystal makes it further difficult to obtain liquid phase adsorption measurements, making it more difficult to sustain crystal vibrations. The piezoelectric crystal's frequency is determined by the liquid phase density over the crystal's surface. Therefore, the change in density induced by the solvent gradient and the solute causes the crystal's resonant frequency to drift. Reference crystals and a coated sample crystal were used to compensate for changes in liquid density. Only one side of each crystal encounters the liquid phase to achieve stable oscillations. The density gradient, flow rate, and temperature effects are removed by using a reference crystal. To regulate the surface adsorption capabilities of the sample crystals in the presence of effluent, long-chain hydrocarbons were used. These coatings could only detect smaller non-polar

molecules; however, advanced surface modification techniques offer more sensitive and rapid detection. Piezoelectric crystals give very good results when they are used in photoacoustic detectors for liquid chromatography. According to the photoacoustic detection principle, when a solute is dissolved in the solvent and irradiated with a suitable light source, the solution expands due to light adsorption. Expansion to a piezoelectric crystal changes crystal resonant frequency. When a laser is utilized to illuminate the sample, photoacoustic detection of the compounds in the static solutions becomes an extremely sensitive approach. Therefore, an analysis of this type of detection system's application in liquid chromatography was analyzed. By combining liquid chromatography with the quartz crystal microbalance, Kartanas et al. [126] describe a technique for label-free protein analysis, Figure 25. This method uses size omission chromatography to initially separate a mixture of proteins in the physiological buffer solution, allowing for the selection of particular protein fractions, desalination, and subsequent spray-drying over the quartz crystal microbalance for mass analysis. Protein detection and sample fractionation are accomplished simultaneously by creating a continuous interface between the spray device and chromatography column using the flow splitter with precision as low as 100 µg/mL. With this method of quantitative mixture analysis, it could be possible to identify different protein species within physiological conditions. The most widely employed bulk analytical techniques have limitations regarding their capability to separate particular protein species hence needing more time to take steps. This work demonstrates a method for addressing these challenges by executing label-free protein detection by combining liquid chromatography with the gravimetric quartz crystal microbalance detection using the micro-fluidic spray nozzle and resulting in the protein detection limit at the microgram level.

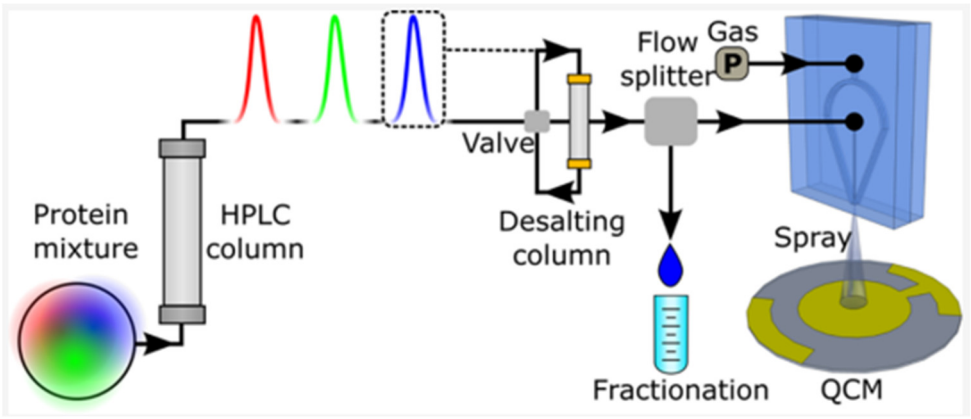


Figure 25. Label-free protein analysis by Kartanas et al. reproduced with permission from [126], American Chemical Society, 2021.

4.5. Trace Metal Analysis

Mieure and Jones [127] created an electrogravimetry assay that uses piezoelectric crystals to determine trace metals in solution. The electrochemical cell's cathode was made of AT-cut quartz. After passing the known amount of current through the cell, the crystals were removed, washed, and dried. The concentration was calculated by utilizing the frequency shift caused by metal deposition. Cadmium solutions with concentrations ranging from 5.0×10^{-4} M to 5.0×10^{-8} M were investigated. Cadmium accurateness of this technique ranged from 0.42% at a large concentration to 8.7% at a small concentration. Nomura and Mimatsu [128] measured iodide in solution using another electro-gravimetric analysis using silver-covered piezoelectric crystals on a platinum-coated gold electrode. Iodide was electrodeposited at −0.05 Volts in a 10^{-3} M potassium chloride (KCl) sample solution. The pH of the sample solution was adjusted to 9.8 with 10^{-3} M sodium tetraborate (IH) caustic soda solution. This technique involves first running the reagent blank through the detection cell until it reaches a specific frequency. Iodide was present in the sample

solution, which was then passed for 1 min (10^{-6} M to 10^{-5} M) or 10 min (10^{-7} M to 10^{-6} M). After each assay, −0.4 V electrolysis can be used to remove the iodide from the crystal. Lead was extracted from the solution using platinum-coated piezoelectric crystals. In another report, Nomura and Maruyama [129] examined the stability of metal ions in solutions and the method for detecting iron (III) as a phosphate. For concentrations up to 2 mM, it has been demonstrated using standard piezoelectric crystals that the measured frequency change of metals in solution is proportional to the specific conductance, with variations owing to solution density and viscosity. The solution short-circuiting the crystal caused significant frequency changes at concentrations above 20 mM. Under these conditions metal ions i.e., Ni^{2+}, Mn^{2+}, Zn^{2+}, Co^{2+}, Cd^{2+}, Pb^{2+}, Ag^{2+}, and Cu^{2+} was deposited on the electrodes. Changes in aluminum and iron frequencies have been attributed to salt adsorption. Another quartz plate was placed on the other side of the quartz plate, with just "four thin hairs deposited on each of the sides of the 'square' quartz plate", separating the two. The plate was firmly bonded with epoxy resin. To avoid electrolysis, resin is also applied to the crystal holder's lead wire. It was discovered that the modified crystal responded linearly to lead (III) in the range of 1×10^{-5} M to 1×10^{-4} M. Interference experiments concerning an iron (III) solution at 5×10^{-5} M have shown that the 10-fold molarities can be harmful if deviations larger than 15% are attained. This occurs with aluminum, sulfide and thiosulphate, bismuth, and lead [106–108]. The contamination brought on by the existence of trace metals that could transmit through the in-filtrate water and soil is one of the main problems with mining operations and has a direct impact on the sustainability index for the environment. There are numerous methodologies that could be utilized to detect trace metals in the water and soil, as depicted in Figure 26, but the majority of them have limitations that make it impossible to apply them in real-world settings. There have been numerous attempts to develop portable sensor devices for regulating environmental trace metal concentrations. The transducer and the sensing elements are the two primary components of a traditional sensor for the precise detection of an analyte. This is because adding new structures to sensors, like nanostructures, can significantly increase their effectiveness in terms of selectivity, sensitivity, portability, and multiplexed detection [130]. Due to their availability, chemical stability, and high-temperature impedance, quartz crystals have become the most often used type of natural and synthetic materials that demonstrate the piezoelectric effect [131]. The self-generating, flexibility, high frequency, huge dielectric constant, and ease of use are some of the benefits of piezoelectric transducers.

The quartz crystal microbalance could be utilized under a variety of conditions, including liquid conditions, gas sensors, and in vacuums. It is helpful for monitoring the record of the rate of vacuum-based thin-film deposition systems. A flow-type chemical sensor was investigated by Sartore et al. [132] in 2011 for the purpose of detecting trace metals in the aqueous solutions, Figure 27. The 9 MHz AT-cut quartz crystal resonator used in the sensor's construction enables the surface chelation of metal ions. The use of new methods has made it possible to isolate gold electrodes with surface modifications that are highly capable of tracing metal ions and complexing them. By complexing with the functional groups included in polymers, these polymers grafted quartz crystal microbalance sensors may effectively adsorb trace metals from solution, such as lead, chrome, cadmium, and copper, in a range between 0.01 ppm–1000 ppm of concentration.

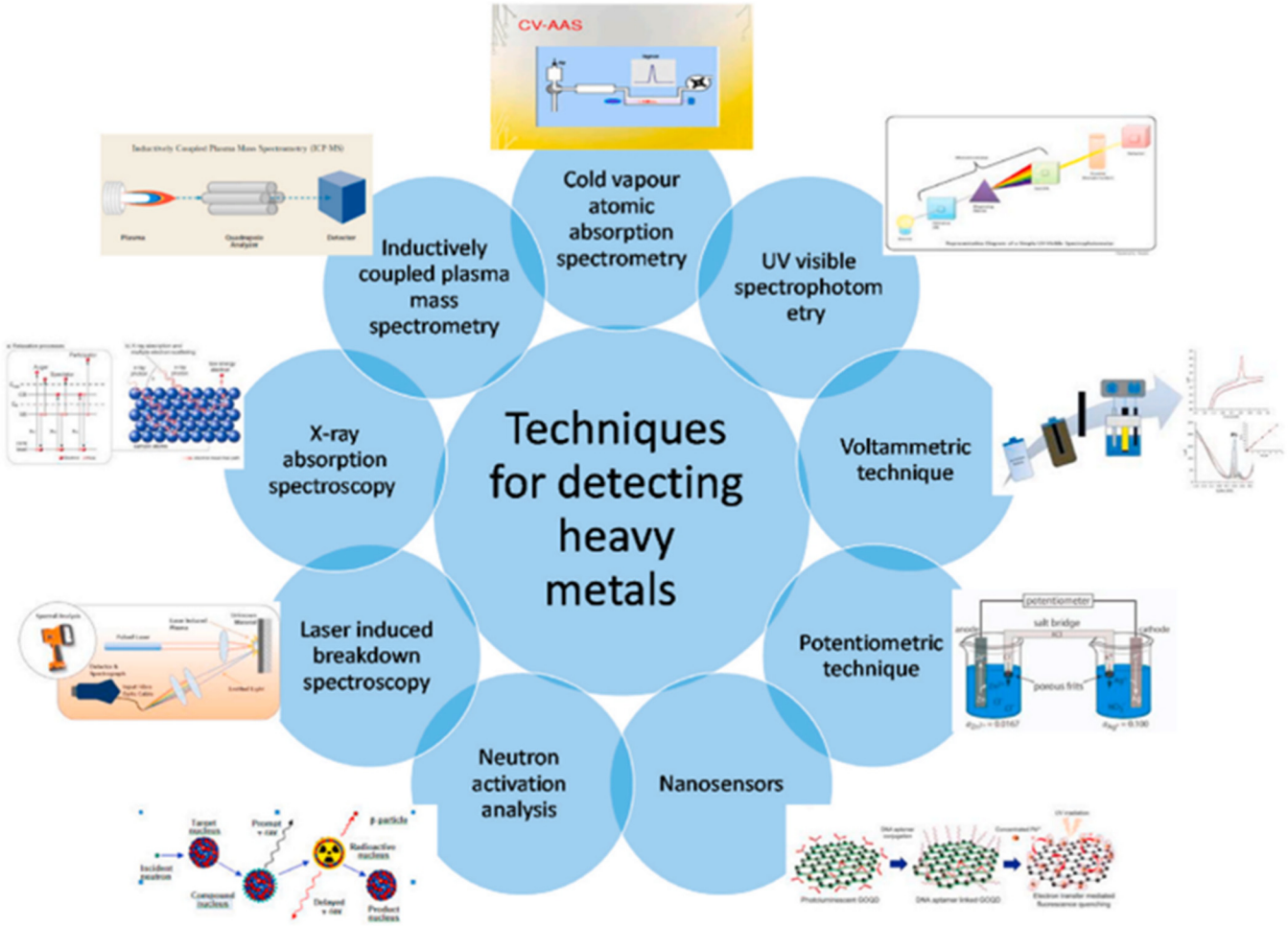


Figure 26. Numerous methodologies utilized for the detection of trace metals reproduced with permission from [130], Elsevier, 2021.

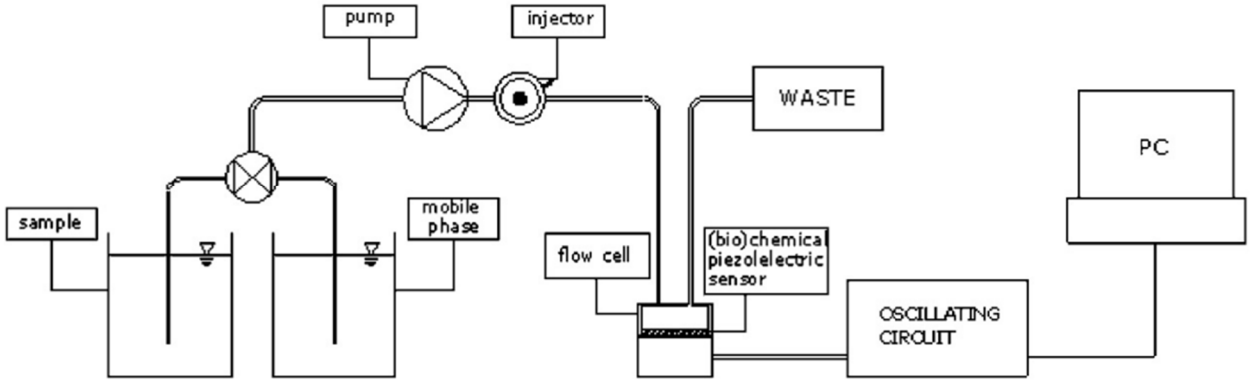


Figure 27. Chemical sensor developed by Sartore et al. for the detection of trace metals, schematic diagram reproduced with permission from [132], Elsevier, 2011.

Similarly, Huseynli et al. [133], in 2018, investigated a novel method for the quartz crystal microbalance nano-sensors for the detection of Hg (II) ions in wastewater. In this method, the N-methacryloyl-(l)-cysteine (MAC) and the Hg^{2+} ions were transformed in the pre-complex, which was subsequently changed on the nano-sensor chips to produce pHEMAC polymers and pHEMAC-Hg (II) ions. According to the estimates, the detection limit is about 0.21×10^{-9} M. The developed Hg (II) ions imprinted nano-sensors exhibit

great sensitivity and selectivity for the detection of Hg (II) ions from wastewater. This approach outperforms others in terms of speed, sensitivity, and affordability.

4.6. Detection of Viruses

Various viruses such as human papilloma, dengue virus, vaccinia, influenza A virus, Ebola virus, hepatitis B, and human immunodeficiency virus are detected by piezoelectric sensors. An alternating current causes a piezoelectric material to mechanically oscillate, creating an oscillating electrical field. The frequency regulated by alternating current voltage drops when the mass rises as a result of the molecular interactions. Piezoelectric sensors of the mass response type are frequently employed for the detection of viruses. Figure 28 provides a schematic representation of the piezoelectric biosensor's working. On the piezoelectric material's upper surface of the electrode, antibodies are attached. The piezoelectric material resonates as a result of the top and bottom electrodes. The majority of materials utilized for sensor materials are anisotropic, including PVDF, $BaTiO_3$, $PbTiO_3$, ZnO, AIN, and SiO_2 [134].

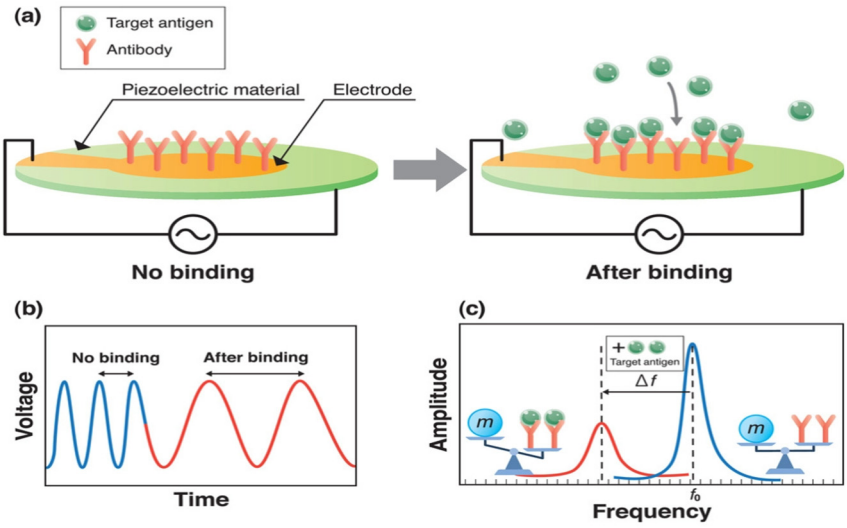


Figure 28. Piezoelectric material used for virus detection; (**a**) piezo-electric biosensor operating principle; graph of (**b**) voltage to time and (**c**) amplitude to frequency, during detection [134].

Human papillomavirus is a potential cause of cervical cancer, the third-most frequent malignancy in women. Fu et al. [135] created a piezoelectric gene sensor for the detection of the papillomavirus using an AT-cut quartz crystal of 10 MHz. Airborne detection and the rapid detection of the vaccinia virus were achieved using quartz crystal microbalance technology. By integrating the quartz crystal microbalance detection methods and polymerase chain reaction (PCR) amplification, Kleo et al. [136] produced a unique system for the detection of the vaccinia virus. Dengue fever is a widespread viral disease that is spread by mosquitoes and causes thousands of fatalities each year. It is a serious health issue in urban and semi-urban areas. A piezoelectric immuno-chip was created by Wu et al. [137] for the detection of the dengue virus. They utilized a 10 MHz quartz crystal microbalance to detect dengue E protein and NS-1 protein using an 8 mm AT-cut quartz wafer sandwiched between the Au electrodes. Since the discovery of the Ebola virus in 1976, thousands of individuals have died from the illness. The virus is transferred among humans via direct contact with the secretions, blood, other body fluids, or organs of the infected persons, as well as with the surfaces and materials that have been contaminated by these fluids. This virus is spread in humans from wild animals. For the quick detection of the Ebola virus, Baca et al. [138] suggested a label-free sensing method that is based on the surface acoustic wave sensor. The sensor chips were created by utilizing wafers of $LiTaO_3$. The influenza virus is the most harmful and prevalent infection, which has a

high level of infectivity and mutagenicity. Type A virus is transmitted both from human to human and animal to human. For the purpose of detecting the influenza-A virus, Jiang et al. [139] devised and created a surface acoustic wave sensor with piezoelectric $LiNbO_3$ wafers coated with SiO_2, Figure 29a. Another of the most frequently encountered diseases around the world is infection with hepatitis B. Despite the fact that billions of individuals have the hepatitis virus, effective treatments and medications have still not been developed to treat chronic hepatitis-B infections. Using the micro-fabrication technology, Xu et al. [140] created a piezo diaphragm-based immuno-assay chip to identify the anti-hepatitis B virus, Figure 29b. The results showed a detection limit of 0.1 ng/mL.

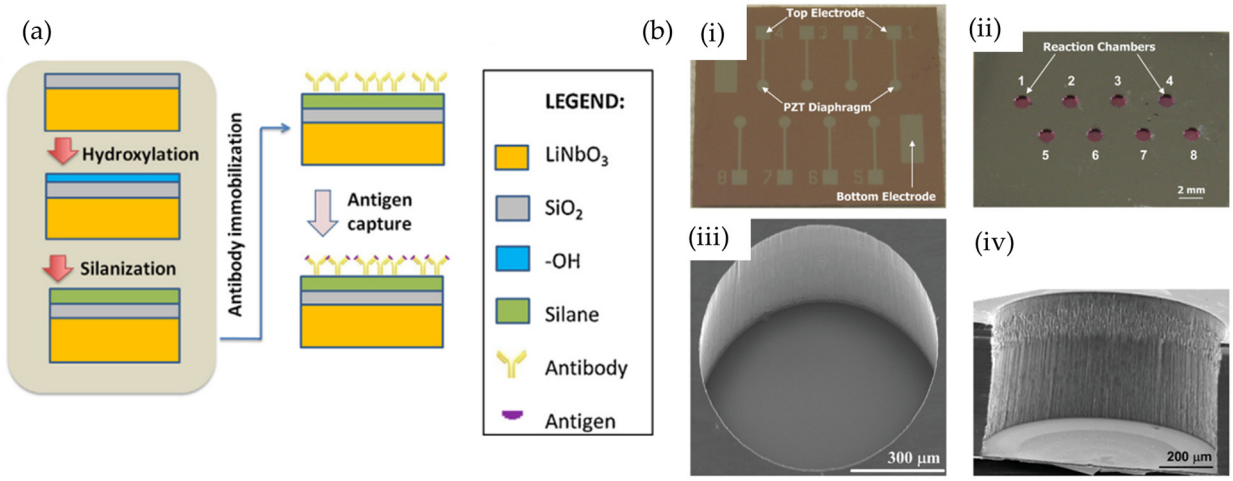


Figure 29. (**a**) Surface acoustic wave sensor for the detection of influenza-A virus devised by Jiang et al. [139]; (**b**) a piezo diaphragm-based immuno-assay chip for the detection of the hepatitis-B virus created by Xu et al. (**i**) SEM image of the manufactured chip, (**ii**) backside view, SEM image of the (**iii**) top view and (**iv**) cross-sectional view created by Xu et al. reproduced with permission from [140], Elsevier, 2015.

4.7. COVID-19 Detection

People's lives have changed all around the world as a result of the severe acute respiratory syndrome coronavirus (SARS-CoV-2) outbreak, which has had a profound effect on economies and communities. As illustrated in Figure 30, new techniques have recently been created to detect SARS-CoV-2 [141].

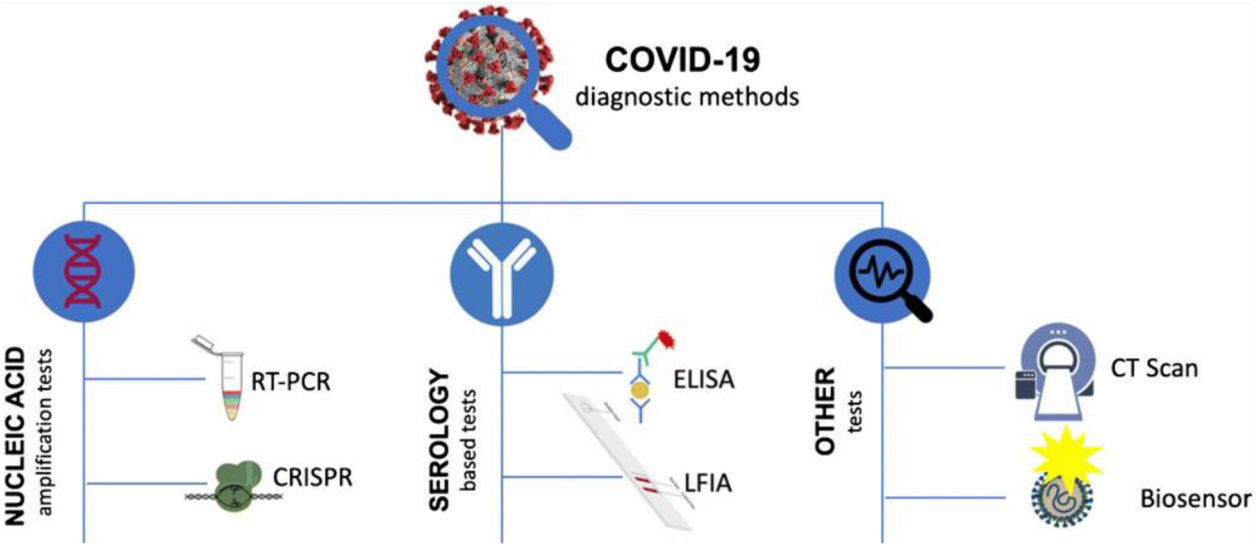


Figure 30. Methods for SARS-CoV-2 detection reproduced with permission from [141], Elsevier, 2011.

By 2030, it is predicted that the IoTs and AI will have a significant economic influence and become progressively more in demand in the upcoming post-corona society. For instance, AI-enabled IoT-connected biosensors may proliferate. Currently, there is a need for the creation of reliable and effective piezoelectric biosensors that can detect SARS-CoV-2. In fact, it has been reported that SARS-CoV can be detected using a piezoelectric immunosensor [142] and applying the recently suggested surface chemistry to the surface of quartz crystal of the quartz crystal microbalance will enable the rapid detection of the SARS-CoV-2, Figure 31 [143].

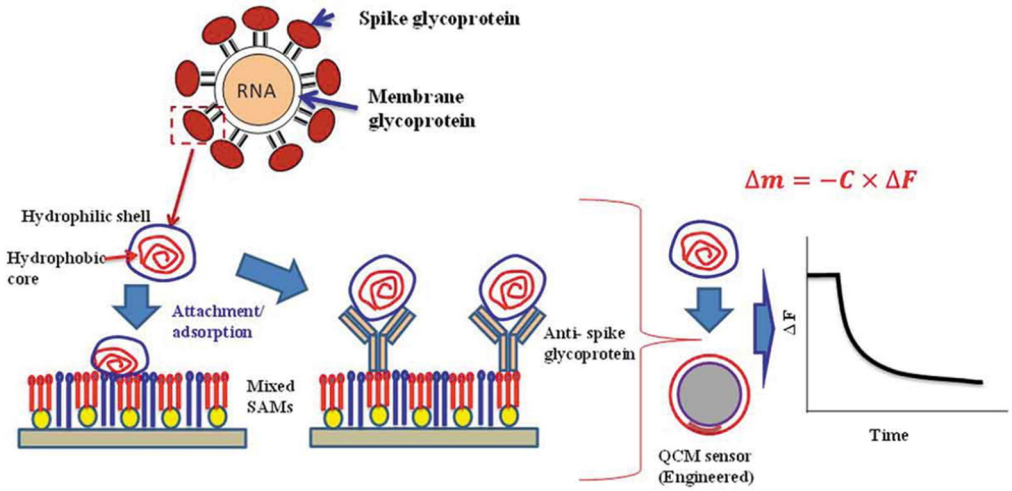


Figure 31. Schematic representation of engineered surfaces that could be applied to the quartz crystal surface of the quartz crystal microbalance for the rapid detection of SARS-CoV-2 reproduced with permission from [143], Elsevier, 2011.

The spike protein has hydrophobic and positively charged residues of amino acids at its protein binding sites. As a result, it is anticipated that a surface that is hydrophobic and negatively charged will adsorb or attach to the spike protein because of the strong electrostatic and hydrophobic interactions. The best-engineered surface used for this purpose appears to be mixed self-assembled monolayers of COOH and CH3 groups. For the real-time detection of the SARS-COV-2 with a sensitivity up to the ng range, the described surface chemistry could be applied to the quartz crystal surface of the quartz crystal microbalance. A piezoelectric microcantilever biosensor was developed for the immediate detection of COVID-19 without the need for any pre-treatment. The associated antibody is coated on the biosensor, which serves as a transducer. A piezo-electric microcantilever bio-sensor function based on the interactions between SARS-CoV-2 antigen and antibody. Through their spike proteins, the SARS-CoV-2 antigens adhered/attached to the microcantilever top surface. Different piezoelectric materials were assessed in order to create a biosensor with the optimum parameters. Consequently, it was determined that a PVDF biosensor provided the optimal result. As a result, the rapid detection of COVID-19 in clinical samples with different viral loads is made possible by the extremely sensitive microcantilever biosensor [144]. Piezoelectrics are attractive candidates for self-powering biosensors for the detection of viruses and communication by harvesting energy from environmental sources. Wearable biosensors should be integrated with the energy harvesters to provide a self-power source. By automatically gathering and transmission of data, such multi-function self-powered devices may be able to control health, making it possible for people to live without the fear of acquiring numerous viral infections. A representation of this type of future society is seen in Figure 32 [134]. Wearable actuators might be capable of guiding individuals away from dangerous situations. The energy required could be generated by the breeze. AI may be able to anticipate the severity and the rate of disease spread.

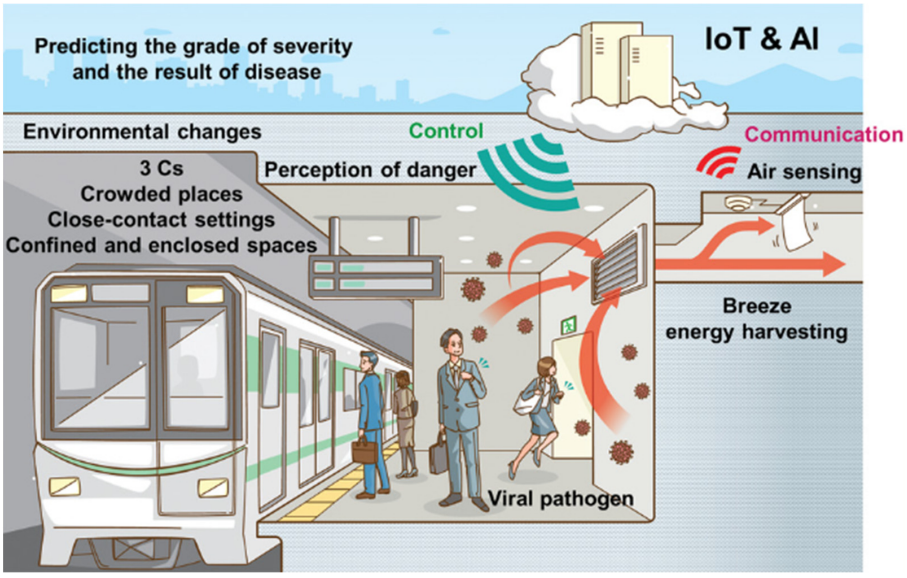


Figure 32. Future society [134].

4.8. Detector for Air Pollutant Detection and Determination

For over 60 years, analyzing SO_2 in the air has been a great concern. Oil refineries, paper and pulp mills, and the effluents released from a variety of other industries are all major sources of SO_2 emissions into the environment. Another ground-level pollution is the combustion of high-sulfur fuels in automobiles. As a result, there is a growing demand for new, effective, simple, and low-cost methods for measuring and controlling SO_2 pollution. Several scientific studies [144–152] have described the use of coated piezoelectric crystals as sensitive SO_2 detectors. Table 5 summarizes the various coating materials and their detection limits, as well as additional measurement settings. For SO_2, many coating materials have been studied. A novel detector was designed using triethanolamine and quadrol as the coating materials, which may detect trace quantities of SO_2 [153]. The primary characteristic of this system is the separation of the column effluent into two equal streams that fall on the opposite faces of a coated crystal simultaneously and directly. This design is expected to enhance sensitivity since the amount of the sample gas reacting with the coating at any specific time is greatly increased. Several experiments examined the effect of changing the temperature. With rising the temperature, the crystals' frequency also increased, according to Guilbault et al. [145], especially from 100 °C to 200 °C. The influence of temperature increases just slightly from 25 °C to 40 °C at 40 Hz. According to these experiments, the temperature needs to be consistent during the reading, but an increase in temperature of 10 degrees Celsius is not critical. Cheney et al. [146] employed triethanolamine as a coating substance. They found that an uncoated 9 MHz crystal's temperature dependence changed by 71 Hz when the temperature was raised from 10 °C to 35 °C. Investigations were also conducted on the SO_2 desorption and adsorption of the coated material at various temperatures. Several diverse ways of applying the substrate to the piezoelectric crystal were examined. Spraying, dropping, and dipping techniques were among them. According to Hartigan [154], the most important factor in coating the crystal is the capability to reproduce the coating procedure, not the amount of coating. For SO_2 detection, Cheney et al. [144] utilized cotton swabs to cover a crystal with ethylenedinitrotetraethanol. A center-covered 9 MHz crystal (340 Hz) was shown to be more sensitive to SO_2 as compared to the fully coated crystal (260 Hz). The scientists also found that the frequency variation caused by varying coating is predictable and constant for a center-coated crystal but not for a fully-coated crystal. Table 5 shows that NO_2 and moisture created significant interferences in the SO_2 assay when all coatings were utilized. Coated piezoelectric crystals cannot provide a reliable quantitative measurement of SO_2 in the presence of NO_2.

Table 5. Coatings used for detecting SO_2.

Coating Material	Coating Method	Sampling Method	Detection Limit ppm	Interference	Results	References
Ethylenedinitrillo-tetraethanol	Smearing with cotton swabs	Flow System in N_2	1 ppm	NO_2	Investigated the position of the coating material	[144]
Triethanolamine	-	Gas handling apparatus, EPA method	25 ppm	NO_2	Investigation of the response time and the nature of the absorption	[146]
Carbowax 400, 20 M; polyphenyl ether; DNP; β, β-oxidipropio-nitrite; triethanolamine; SAIB (sucrose acetate isobutyrate); squalane; amine 220	Dropping	Gas handling apparatus	5 ppm	-	Response time was investigated	[147]
Quadrol	Smearing with a tiny brush	Syringe dilution	20 ppm -50 ppm in the auto exhausts and up to 300 ppm in the stack gases	NO_2	Portable design	[148]
Quadrol	Smearing with a tiny brush	Syringe dilution	1 ppb	NO_2	Hydrophobic membrane used to eliminate interference	[149]
Apiezon; sodium tetra chloro-mercurate; silicone SE-30; carbowax 20 M; silicon QF-1; versamid 900	Spraying	Gas-tight syringe	5 ppm	-	Effect of change of voltage was investigated	[145]
Amine 220; ϱ-toluidine; triethanolamine; armeen 2S; quadrol	Smearing with a tiny brush	Syringe dilution	1.0 ppb	NO_2, moisture	New cells design	[150]
Styrene-dimethyl-aminopropyl-maleimide (1:1 copolymer)	Dropping with syringe	Gas-tight syringe	0.1 ppm	NO_2, moisture	Portable device	[152]
Igepal CO-880; tridodecylamine; diallylamine; SDM polymer; tripropylamine; phenyldiethanolamine PP-2040	-	Gas-tight syringe or gas sampling valve	5 ppm	NO_2	-	[151]

Coated piezoelectric crystal detectors were used to detect NH_3 in the ppb range. A great sensitivity towards ammonia was obtained when the coatings Ucon-LB-3OOX and Ucon 75-H-90,000 were applied [155]. The Ucon coatings reacted with the nitrogen dioxide to create new compounds upon that crystal, showing a high sensitivity towards both nitrogen dioxide and ammonia. These chemicals' infrared spectra showed the creation of new bands and modifications to certain existing bands, indicating the synthesis of new molecules. Atmospheric moisture and excessive amounts of organic chemicals that disintegrate the coatings caused several problems. New coating materials, i.e., coating of ascorbic acid, coating of capsicum annuum pods, and coating of ascorbic acid with silver nitrate, have been used to detect ammonia in the atmosphere precisely [156].

The impact of pesticides on our environment has become a major issue in recent years. Because they are strong cholinesterase inhibitors, pesticides are hazardous to both people and animals. The reactions that the organophosphorus pesticides undergo are all structurally connected to one another. Di-isopropylmethyl phosphonate (DIMP) was selected as a model compound in research by Guilbault and Scheide because almost all organophosphorus pesticides comprise either phosphoryl or thiophosphoryl groups, and the thiophosphoryl pesticides easily undergo oxidation reactions to produce phosphoryl containing compounds [157]. Various inorganic salts, i.e., $CuCl_2$, $CdCl_2$, $NiCl_2$, and $FeCl_3$, were used to coat the crystal, which had an impact on the detection of DIMP in the ppm range. It was determined that other organophosphorus compounds with a similar structure could not be detected using the $FeCl_3$-DIMP complex, which has been utilized as the substrate to measure low quantities of DIMP. In order to specifically determine paraoxon levels, a detector was developed utilizing a piezoelectric crystal and a $FeCl_3$- paraoxon complex as the substrate. Various inorganic salts, i.e., $HgBr_2$, $CuC1_2$, $HgCl_2$, $MnC1_2$, $ZnCl_2$, and $MoCl_5$, had a strong chemical interaction with DIMP [158]. Guilbault noted that salts of the majority of transition metals should perform well as piezoelectric crystal detector coatings.

Hydrogen sulfide is a hazardous gas that raises safety concerns for many industries. This is particularly true as dangerous levels of hydrogen sulfide can go unnoticed by workers and rise suddenly. Techniques have been developed to detect hydrogen sulfide in the atmosphere [159]. The adsorption of hydrogen sulfide (H_2S) on a crystal surface that has been covered with an acetone extract of different soot particles that are produced when specific organochlorine chemicals are burned is the basis of this technique. The best substrate was chlorobenzoic acid extract of soot, and this technique is highly effective in the concentration range between 1–60 ppm. Lead acetate, copper and silver metal, and anthraquinone disulfonic acid are additional coating materials proposed by King to detect hydrogen sulfide.

4.9. Solution Measurement

Nickel dimethylglyoxime has been utilized as a coating by Webber and Guilbault [155] to detect ammonia in solution. By Utilizing the hydrophobic membranes between both the sample solution as well as the crystal, the effects of moisture were reduced. Alternately, the crystal was moved to the sampling chamber after being allowed to establish equilibrium over a sample of the distilled water. A signal of -135 Hz was produced by 0.15 M of ammonia in water. Up to a value of 0.45 M ammonia, the calibration curve was linear. Sulfur dioxide was determined in the ppb range under identical circumstances utilizing quadrol as the coating.

Piezoelectric crystals have been utilized by Nomura and colleagues [160,161] to detect cyanide in solution. AT crystals cut to 9 MHz gold electrodes with silver plating were utilized. An original investigation either used dihydrogen phosphate-borate or a borate-hydroxide buffer to maintain a consistent volume of a sample or a standard solution at pH 9.6. In a water bath, the solution was maintained at a consistent temperature of 25 °C. For the analysis, the crystal, whose frequency was already determined, was submerged inside this solution for about 15 min while being agitated at 430 rpm. After being removed, the

crystal was cleaned with acetone and water before being immersed in a steady stream of 30 °C air. The frequency was determined after 1 minute. According to reports, cyanide measurement has a linear range from 10^{-7} M to 10^{-5} M. Ethylenediaminetetraacetic acid (EDTA) was used to remove the cation interferences that formed complexes with cyanide.

A preliminary investigation into the utilization of the piezoelectric quartz crystals to evaluate the rate of microbial or fungal growth on their surface was published in Down [162]. The study was unable to quantify any significant alterations brought on by the expansion of these biological systems. It was believed that cells grew very slowly and that the cell membrane was broken by high-frequency vibrations.

Nomura and Tsuge [163] used an oscillator equipped with transistors to develop a technique for the determination of the silver concentration in the solution. It was found that this form of oscillator had a much lower frequency drift than an integrated circuit oscillator, which has previously been reported [164]. Silver concentration in solution is measured using a three-electrode deposition system that includes a platinum-plated gold electrode as that of the cathode, a coiled platinum wire as the anode, and a silver chloride as the reference electrode. The test solution is mixed with 1×10^{-3} M EDTA to create a stable combination with the intervening ions in the solution. Mercury (II) was deposited on the electrode even in the presence of EDTA; however, a technique was established for both silver and mercury in the solution. After 10 min of electrodeposition, the silver response was linear, ranging from 10^{-6} M to 3×10^{-5} M and from 2×10^{-7} M to 1×10^{-6} M after 1 h.

Nomura and colleagues [165] devised a sensitive method for the determination of iodide in the solution utilizing a silver-plated piezoelectric crystal. First, 11.2 mL (approximately 0.38 oz)/min of a blank solution containing reagent is delivered through the cell until the crystal's frequency has stabilized (F1). The blank solution containing the reagent is added to the cell till the crystal reaches equilibrium (F2) after the sample or the standard solution has been running through it for precisely five minutes. The frequency change (ΔF), i.e., F = F1 − F2 is proportionate to the concentration of iodide. A 0.01 M of ammoniacal buffer solution having pH 9.4 containing 2 mM of sodium thiosulfate can then be passed through the cell for over 30 s at 50 Hz to remove the deposited iodide from the electrode (F). At least 30 determinations can be performed before the electrode must be replotted. This technique can detect iodide at concentrations ranging from 0.5 M to 7 M.

4.10. Miscellaneous Applications

Daley et al. [166] determined the mass (concentration) of an aerosol using a piezoelectric crystal sensor. Humidity, temperature, particle accumulation characteristics, mass sensitivity, and response linearity were examined as five areas of influence. No reference crystal is used to compensate for changes in airflow temperature or humidity. By reducing the inlet temperature's rate of change, the error due to temperature was successfully reduced. The absorption and release of moisture by aerosol deposition caused the error due to humidity. The recorded linear response limitations for several aerosols and devices ranged from 0.2 μg/mm^2 to 6 μg/mm^2. Mass sensitivity was affected by sediment size and location. At particle sizes of 2 m in diameter, mass sensing was reduced, reaching 0 m to 20 m. In the size range of 2 μm–20 μm, plastic crystal coatings improved sensor performance. Olin et al. [167] assert that the suspended particle's mass concentration can be determined using piezoelectric quartz as a microbalance. A collector, such as an electrostatic precipitator or an impactor, deposits suspended particles on the surface of the electrode of the vibrating crystal, and the resonance frequency lowers proportionally to the additional mass of the particles. The device's time resolution and high sensitivity were examined. An electrostatic precipitator that sampled at 1 L/min was utilized to measure the mass concentration of the particles in the air at 41 s to within 5%. Chuan [168] s described a portable direct reading device capable of monitoring particle mass concentrations in the range of about 50 μg/m^3 to 5000 μg/m$_3$. Vapors in the air, including water vapor, have no impact on the sensors. The chemisorption reactions of mono-, dimethyl-, and trimethylamine with piezoelectric

crystals in vacuum systems have been studied at ambient temperature [169,170]. For the solid substrate coating over the crystals, thin films of several metal salts such as $ZnCl_2$, $FeCl_3$, $CoCl_2$, ZnI_2, and $HgBr_2$ have been applied. The reactions were studied to find the optimal coating for detecting and identifying these dangerous amines with piezoelectric crystal detectors. Iron (III) chloride coating has immense potential. Behrndt etc. [171] and Oberg [172] created a technique that makes use of piezoelectric crystals to measure the deposition rate and the thickness of the film. AT-cut crystals in thick slip mode with a vibration frequency of 2.5 MHz show a frequency variation of about 1 Hz per thickness of the metal accumulated over the exposed facets. On average, crystals can hold about 20,000 g (about 44.09 lb) of metal before the deposits need to be removed or new crystals need to be used. King [173] used a solvent sorption detector to create a simple portable detector for studying the detection limits of various chemicals. Finally, quartz thermometers, quartz pressure transducers [174], and thin film thermocouples [175] are some other applications.

5. Future Perspective and Conclusions

Piezoelectric materials have a very promising future in analytical chemistry. This review covers the recent advancements in piezoelectric materials for analytical applications. For various purposes, changing mechanical vibrations in various frequency bands are obtained using piezoelectric materials of the specific frequency. When selecting piezoelectric materials for experiments, these factors consistently offer guidance. Analytical chemistry uses piezoelectric crystals in a variety of ways. Most of those described devices are available commercially. However, equipment for detecting various gas/pollutants is not yet available because finding a long-life coating is difficult or specified only for the target gas. However, there are many devices that are portable with it and are in the developing stage, which shows the major role of piezoelectric materials in the future. In particular, coronavirus detection and sampling have been highlighted in this review and are currently the subject of intense research. There is a need to create more efficient and reliable viral detection sensors with higher accuracy and sensitivity, smaller weight and size, and lower cost in the future. Such sensors are going to become a reality as materials science further develops and with the technological development of AI, data analytics, and machine learning. Piezoelectric materials can be crucial in developing novel solutions to problems relating to energy and environmental concerns. Piezoelectric materials transform mechanical energy into a source of electrical energy that can be used later. Although piezo analytical applications are of great interest with increasing research, patents, and publications, commercial translations of these potential applications are necessary.

Author Contributions: Conceptualization, A.A.; methodology, H.S., S.B. and A.A.; software, H.S. and A.A.; formal analysis, H.S. and S.B.; investigation, H.S.; resources, A.A., W.A.A., M.N. and S.A.K.; writing—original draft preparation, H.S.; writing—review and editing, A.A., S.B., W.A.A., M.N. and S.A.K.; visualization, H.S. and S.B.; supervision, A.A.; project administration, A.A., S.B., W.A.A., M.N. and S.A.K. All authors have read and agreed to the published version of the manuscript.

Funding: This research received no external funding.

Institutional Review Board Statement: Not applicable.

Informed Consent Statement: Not applicable.

Data Availability Statement: Not applicable.

Conflicts of Interest: The authors declare no conflict of interest.

References

1. Bettini, S.; Pagano, R.; Bonfrate, V.; Maglie, E.; Manno, D.; Serra, A.; Valli, L.; Giancane, G. Promising Piezoelectric Properties of New ZnO@Octadecylamine Adduct. *J. Phys. Chem. C* **2015**, *119*, 20143–20149. [CrossRef]
2. Săvescu, C.; Comeagă, D.; Morega, A.; Veli, Y. Experimental Tests with Piezoelectric Harvester for Tuning Resonant Frequency to Vibrating Source. *Rev. Roum. Sci. Techn.—Électrotechn. Énerg.* **2022**, *67*, 457–460.

3. Kouritem, S.A.; Altabey, W.A. Ultra-broadband natural frequency using automatic resonance tuning of energy harvester and deep learning algorithms. *Energy Convers. Manag.* **2022**, *272*, 116332. [CrossRef]
4. Bani-Hani, M.; Aljanaideh, K.; Almomani, A.; Kouritem, S.A. Analytical Modeling and Numerical Investigation of Earthquake-Induced Structural Vibration Energy Harvester. *IEEE Sens. J.* **2022**, *22*, 19237–19248. [CrossRef]
5. Elahi, H.; Mughal, M.R.; Eugeni, M.; Qayyum, F.; Israr, A.; Ali, A.; Munir, K.; Praks, J.; Gaudenzi, P. Characterization and Implementation of a Piezoelectric Energy Harvester Configuration: Analytical, Numerical and Experimental Approach. *Integr. Ferroelectr.* **2020**, *212*, 39–60. [CrossRef]
6. Wu, J.; Wu, Z.; Qian, W.; Jia, Y.; Wang, Y.; Luo, H. Electric-field-treatment-induced enhancement of photoluminescence in $Er3^{+}$-doped $(Ba_{0.95}Sr_{0.05})(Zr_{0.1}Ti_{0.9})O_3$ piezoelectric ceramic. *Mater. Lett.* **2016**, *184*, 131–133. [CrossRef]
7. Zhu, R.; Yang, R. Introduction to the Piezotronic Effect and Sensing Applications. In *Synthesis and Characterization of Piezotronic Materials for Application in Strain/Stress Sensing*; Springer: Cham, Switzerland, 2018; pp. 1–4. [CrossRef]
8. Hehn, T.; Manoli, Y. CMOS Circuits for Piezoelectric Energy Harvesters. *Springer Ser. Adv. Microelectron.* **2015**, *38*, 21–40. [CrossRef]
9. Sezer, N.; Koç, M. A comprehensive review on the state-of-the-art of piezoelectric energy harvesting. *Nano Energy* **2021**, *80*, 105567. [CrossRef]
10. Kobayashi, T.; Ichiki, M.; Kondou, R.; Nakamura, K.; Maeda, R. Fabrication of piezoelectric microcantilevers using $LaNiO_3$ buffered $Pb(Zr,Ti)O_3$ thin film. *J. Micromech. Microeng.* **2008**, *18*, 035007. [CrossRef]
11. Katsouras, I.; Asadi, K.; Li, M.; Van Driel, T.B.; Kjær, K.S.; Zhao, D.; Lenz, T.; Gu, Y.; Blom, P.W.M.; Damjanovic, D.; et al. The negative piezoelectric effect of the ferroelectric polymer poly(vinylidene fluoride). *Nat. Mater.* **2015**, *15*, 78–84. [CrossRef]
12. Ueda, S.; Okada, M.; Nakaue, Y. Transient thermal response of a functionally graded piezoelectric laminate with a crack normal to the bimaterial interface. *J. Therm. Stress.* **2017**, *41*, 98–118. [CrossRef]
13. Elahi, H.; Eugeni, M.; Gaudenzi, P. Electromechanical Degradation of Piezoelectric Patches. *Adv. Struct. Mater.* **2018**, *81*, 35–44. [CrossRef]
14. Kouritem, S.A.; Bani-Hani, M.A.; Beshir, M.; Elshabasy, M.M.; Altabey, W.A. Automatic Resonance Tuning Technique for an Ultra-Broadband Piezoelectric Energy Harvester. *Energies* **2022**, *15*, 7271. [CrossRef]
15. Elahi, H.; Eugeni, M.; Gaudenzi, P. A Review on Mechanisms for Piezoelectric-Based Energy Harvesters. *Energies* **2018**, *11*, 1850. [CrossRef]
16. Xia, Y.; Michelin, S.; Doaré, O. Fluid-Solid-Electric Lock-In of Energy-Harvesting Piezoelectric Flags. *Phys. Rev. Appl.* **2015**, *3*, 014009. [CrossRef]
17. Yang, Z.; Erturk, A.; Zu, J. On the efficiency of piezoelectric energy harvesters. *Extrem. Mech. Lett.* **2017**, *15*, 26–37. [CrossRef]
18. Kouritem, S.A.; Al-Moghazy, M.A.; Noori, M.; Altabey, W.A. Mass tuning technique for a broadband piezoelectric energy harvester array. *Mech. Syst. Signal Process.* **2022**, *181*, 109500. [CrossRef]
19. Ali, A.; Pasha, R.A.; Sheeraz, M.A.; Butt, Z.; Elahi, H.; Khan, A.A. Investigation of Electrical Properties for Cantilever-Based Piezoelectric Energy Harvester. *Adv. Sci. Technol. Res. J.* **2019**, *13*, 76–85. [CrossRef]
20. Ali, F.; Raza, W.; Li, X.; Gul, H.; Kim, K.-H. Piezoelectric energy harvesters for biomedical applications. *Nano Energy* **2019**, *57*, 879–902. [CrossRef]
21. Ghazanfarian, J.; Mohammadi, M.M.; Uchino, K. Piezoelectric Energy Harvesting: A Systematic Review of Reviews. *Actuators* **2021**, *10*, 312. [CrossRef]
22. Li, H.; Sang, Y.; Chang, S.; Huang, X.; Zhang, Y.; Yang, R.; Jiang, H.; Liu, H.; Wang, Z.L. Enhanced Ferroelectric-Nanocrystal-Based Hybrid Photocatalysis by Ultrasonic-Wave-Generated Piezophototronic Effect. *Nano Lett.* **2015**, *15*, 2372–2379. [CrossRef] [PubMed]
23. Qian, W.; Zhao, K.; Zhang, D.; Bowen, C.R.; Wang, Y.; Yang, Y. Piezoelectric Material-Polymer Composite Porous Foam for Efficient Dye Degradation via the Piezo-Catalytic Effect. *ACS Appl. Mater. Interfaces* **2019**, *11*, 27862–27869. [CrossRef] [PubMed]
24. Zhang, Y.; Schultz, A.M.; Salvador, P.A.; Rohrer, G.S. Spatially selective visible light photocatalytic activity of $TiO_2/BiFeO_3$ heterostructures. *J. Mater. Chem.* **2011**, *21*, 4168–4174. [CrossRef]
25. Bermúdez, V.; Caccavale, F.; Sada, C.; Segato, F.; Diéguez, E. Etching effect on periodic domain structures of lithium niobate crystals. *J. Cryst. Growth* **1998**, *191*, 589–593. [CrossRef]
26. Holstein, W.L. Etching study of ferroelectric microdomains in $LiNbO_3$ and MgO:$LiNbO_3$. *J. Cryst. Growth* **1997**, *171*, 477–484. [CrossRef]
27. Nassau, K.; Levinstein, H.J.; Loiacono, G.M. The domain structure and etching of ferroelectric lithium niobate. *Appl. Phys. Lett.* **1965**, *6*, 228–229. [CrossRef]
28. Sones, C.L.; Mailis, S.; Brocklesby, W.S.; Eason, R.W.; Owen, J.R. Differential etch rates in z-cut $LiNbO_3$ for variable HF/HNO_3 concentrations. *J. Mater. Chem.* **2001**, *12*, 295–298. [CrossRef]
29. Xue, X.; Wang, S.; Guo, W.; Zhang, Y.; Wang, Z.L. Hybridizing Energy Conversion and Storage in a Mechanical-to-Electrochemical Process for Self-Charging Power Cell. *Nano Lett.* **2012**, *12*, 5048–5054. [CrossRef]
30. Ramadoss, A.; Saravanakumar, B.; Lee, S.W.; Kim, Y.-S.; Kim, S.J.; Wang, Z.L. Piezoelectric-Driven Self-Charging Supercapacitor Power Cell. *ACS Nano* **2015**, *9*, 4337–4345. [CrossRef]

31. Song, R.; Jin, H.; Li, X.; Fei, L.; Zhao, Y.; Huang, H.; Chan, H.L.-W.; Wang, Y.; Chai, Y. A rectification-free piezo-supercapacitor with a polyvinylidene fluoride separator and functionalized carbon cloth electrodes. *J. Mater. Chem. A* **2015**, *3*, 14963–14970. [CrossRef]
32. Wang, F.; Jiang, C.; Tang, C.; Bi, S.; Wang, Q.; Du, D.; Song, J. High output nano-energy cell with piezoelectric nanogenerator and porous supercapacitor dual functions—A technique to provide sustaining power by harvesting intermittent mechanical energy from surroundings. *Nano Energy* **2016**, *21*, 209–216. [CrossRef]
33. Parida, K.; Bhavanasi, V.; Kumar, V.; Wang, J.; Lee, P.S. Fast charging self-powered electric double layer capacitor. *J. Power Sources* **2017**, *342*, 70–78. [CrossRef]
34. Lee, B.-S.; Yoon, J.; Jung, C.; Kim, D.Y.; Jeon, S.-Y.; Kim, K.-H.; Park, J.-H.; Park, H.; Lee, K.H.; Kang, Y.-S.; et al. Silicon/Carbon Nanotube/$BaTiO_3$ Nanocomposite Anode: Evidence for Enhanced Lithium-Ion Mobility Induced by the Local Piezoelectric Potential. *ACS Nano* **2016**, *10*, 2617–2627. [CrossRef] [PubMed]
35. Kim, S.; Choi, S.J.; Zhao, K.; Yang, H.; Gobbi, G.; Zhang, S.; Li, J. Electrochemically driven mechanical energy harvesting. *Nat. Commun.* **2016**, *7*, 10146. [CrossRef]
36. Lang, S.B.; Tofail, S.A.M.; Kholkin, A.L.; Wojtaś, M.; Gregor, M.; Gandhi, A.A.; Wang, Y.; Bauer, S.; Krause, M.; Plecenik, A. Ferroelectric Polarization in Nanocrystalline Hydroxyapatite Thin Films on Silicon. *Sci. Rep.* **2013**, *3*, 2215. [CrossRef]
37. Baxter, F.R.; Bowen, C.; Turner, I.G.; Dent, A.C.E. Electrically Active Bioceramics: A Review of Interfacial Responses. *Ann. Biomed. Eng.* **2010**, *38*, 2079–2092. [CrossRef]
38. Touach, N.; Ortiz-Martínez, V.; Salar-García, M.; Benzaouak, A.; Hernández-Fernández, F.; de Ríos, A.P.; El Mahi, M.; Lotfi, E. On the use of ferroelectric material $LiNbO_3$ as novel photocatalyst in wastewater-fed microbial fuel cells. *Particuology* **2017**, *34*, 147–155. [CrossRef]
39. Tiwari, D.; Dunn, S.; Zhang, Q. Impact of Zr/Ti ratio in the PZT on the photoreduction of silver nanoparticles. *Mater. Res. Bull.* **2009**, *44*, 1219–1224. [CrossRef]
40. Mushtaq, F.; Chen, X.; Hoop, M.; Torlakcik, H.; Pellicer, E.; Sort, J.; Gattinoni, C.; Nelson, B.J.; Pané, S. Piezoelectrically Enhanced Photocatalysis with $BiFeO_3$ Nanostructures for Efficient Water Remediation. *iScience* **2018**, *4*, 236–246. [CrossRef]
41. Sun, C.; Fu, Y.; Wang, Q.; Xing, L.; Liu, B.; Xue, X. Ultrafast piezo-photocatalytic degradation of organic pollutions by Ag_2O/tetrapod-ZnO nanostructures under ultrasonic/UV exposure. *RSC Adv.* **2016**, *6*, 87446–87453. [CrossRef]
42. Hong, D.; Zang, W.; Guo, X.; Fu, Y.; He, H.; Sun, J.; Xing, L.; Liu, B.; Xue, X. High Piezo-photocatalytic Efficiency of CuS/ZnO Nanowires Using Both Solar and Mechanical Energy for Degrading Organic Dye. *ACS Appl. Mater. Interfaces* **2016**, *8*, 21302–21314. [CrossRef] [PubMed]
43. Wu, M.-H.; Lee, J.-T.; Chung, Y.J.; Srinivaas, M.; Wu, J.-M. Ultrahigh efficient degradation activity of single- and few-layered $MoSe_2$ nanoflowers in dark by piezo-catalyst effect. *Nano Energy* **2017**, *40*, 369–375. [CrossRef]
44. Masimukku, S.; Hu, Y.-C.; Lin, Z.-H.; Chan, S.-W.; Chou, T.-M.; Wu, J.M. High efficient degradation of dye molecules by PDMS embedded abundant single-layer tungsten disulfide and their antibacterial performance. *Nano Energy* **2018**, *46*, 338–346. [CrossRef]
45. Xing, L.; Nie, Y.; Xue, X.; Zhang, Y. PVDF mesoporous nanostructures as the piezo-separator for a self-charging power cell. *Nano Energy* **2014**, *10*, 44–52. [CrossRef]
46. Kim, Y.-S.; Xie, Y.; Wen, X.; Wang, S.; Kim, S.J.; Song, H.-K.; Wang, Z.L. Highly porous piezoelectric PVDF membrane as effective lithium ion transfer channels for enhanced self-charging power cell. *Nano Energy* **2015**, *14*, 77–86. [CrossRef]
47. Noris-Suárez, K.; Lira-Olivares, J.; Ferreira, A.M.; Graterol, A.; Feijoo, J.L.; Lee, S.W. Electrochemical Influence of Collagen Piezoelectric Effect in Bone Healing. *Mater. Sci. Forum* **2007**, *544–545*, 981–984. [CrossRef]
48. Giocondi, J.L.; Rohrer, G.S. The Influence of the Dipolar Field Effect on the Photochemical Reactivity of $Sr_2Nb_2O_7$ and $BaTiO_3$ Microcrystals. *Top. Catal.* **2008**, *49*, 18–23. [CrossRef]
49. Hong, K.-S.; Xu, H.; Konishi, H.; Li, X. Direct Water Splitting through Vibrating Piezoelectric Microfibers in Water. *J. Phys. Chem. Lett.* **2010**, *1*, 997–1002. [CrossRef]
50. Starr, M.B.; Shi, J.; Wang, X. Piezopotential-Driven Redox Reactions at the Surface of Piezoelectric Materials. *Angew. Chem.* **2012**, *124*, 6064–6068. [CrossRef]
51. Tan, C.F.; Ong, W.L.; Ho, G.W. Self-Biased Hybrid Piezoelectric-Photoelectrochemical Cell with Photocatalytic Functionalities. *ACS Nano* **2015**, *9*, 7661–7670. [CrossRef]
52. Lin, J.-H.; Tsao, Y.-H.; Wu, M.-H.; Chou, T.-M.; Lin, Z.-H.; Wu, J.M. Single- and few-layers MoS_2 nanocomposite as piezo-catalyst in dark and self-powered active sensor. *Nano Energy* **2017**, *31*, 575–581. [CrossRef]
53. Lv, W.; Kong, L.; Lan, S.; Feng, J.; Xiong, Y.; Tian, S. Enhancement effect in the piezoelectric degradation of organic pollutants by piezo-Fenton process. *J. Chem. Technol. Biotechnol.* **2016**, *92*, 152–156. [CrossRef]
54. Hong, K.-S.; Xu, H.; Konishi, H.; Li, X. Piezoelectrochemical Effect: A New Mechanism for Azo Dye Decolorization in Aqueous Solution through Vibrating Piezoelectric Microfibers. *J. Phys. Chem. C* **2012**, *116*, 13045–13051. [CrossRef]
55. Xue, X.; Zang, W.; Deng, P.; Wang, Q.; Xing, L.; Zhang, Y.; Wang, Z.L. Piezo-potential enhanced photocatalytic degradation of organic dye using ZnO nanowires. *Nano Energy* **2015**, *13*, 414–422. [CrossRef]
56. Liu, L.; Lu, K.; Wang, T.; Liao, F.; Peng, M.; Shao, M. Flexible piezoelectric nanogenerators based on silicon nanowire/α-quartz composites for mechanical energy harvesting. *Mater. Lett.* **2015**, *160*, 222–226. [CrossRef]

57. Zhang, H.; Zhang, S.; Yao, G.; Huang, Z.; Xie, Y.; Su, Y.; Yang, W.; Zheng, C.; Lin, Y. Simultaneously Harvesting Thermal and Mechanical Energies based on Flexible Hybrid Nanogenerator for Self-Powered Cathodic Protection. *ACS Appl. Mater. Interfaces* **2015**, *7*, 28142–28147. [CrossRef]
58. Ali, A.; Sheeraz, M.A.; Bibi, S.; Khan, M.Z.; Malik, M.S.; Ali, W. Artificial neural network (ANN)-based optimization of a numerically analyzed m-shaped piezoelectric energy harvester. *Funct. Mater. Lett.* **2021**, *14*, 2151046. [CrossRef]
59. Gosavi, S.K.; Balpande, S.S. A Comprehensive Review of Micro and Nano Scale Piezoelectric Energy Harvesters. *Sens. Lett.* **2019**, *17*, 180–195. [CrossRef]
60. Li, H.; Tian, C.; Deng, Z.D. Energy harvesting from low frequency applications using piezoelectric materials articles. *Appl. Phys. Rev.* **2014**, *1*, 41301. [CrossRef]
61. Narita, F.; Fox, M. A Review on Piezoelectric, Magnetostrictive, and Magnetoelectric Materials and Device Technologies for Energy Harvesting Applications. *Adv. Eng. Mater.* **2017**, *20*, 1700743. [CrossRef]
62. Lefeuvre, E.; Sebald, G.; Guyomar, D.; Lallart, M.; Richard, C. Materials, structures and power interfaces for efficient piezoelectric energy harvesting. *J. Electroceram.* **2007**, *22*, 171–179. [CrossRef]
63. Safaei, M.; Sodano, H.A.; Anton, S.R. A review of energy harvesting using piezoelectric materials: State-of-the-art a decade later (2008–2018). *Smart Mater. Struct.* **2019**, *28*, 113001. [CrossRef]
64. Liu, H.; Zhong, J.; Lee, C.; Lee, S.-W.; Lin, L. A comprehensive review on piezoelectric energy harvesting technology: Materials, mechanisms, and applications. *Appl. Phys. Rev.* **2018**, *5*, 041306. [CrossRef]
65. Amin, A.R.; Ali, A.; Ali, H.M. Application of Nanofluids for Machining Processes: A Comprehensive Review. *Nanomaterials* **2022**, *12*, 4214. [CrossRef]
66. Yuan, X.; Changgeng, S.; Yan, G.; Zhenghong, Z. Application review of dielectric electroactive polymers (DEAPs) and piezoelectric materials for vibration energy harvesting. *J. Phys. Conf. Ser.* **2016**, *744*, 12077. [CrossRef]
67. Mishra, S.; Unnikrishnan, L.; Nayak, S.K.; Mohanty, S. Advances in Piezoelectric Polymer Composites for Energy Harvesting Applications: A Systematic Review. *Macromol. Mater. Eng.* **2018**, *304*, 1800463. [CrossRef]
68. Bowen, C.R.; Kim, H.A.; Weaver, P.M.; Dunn, S. Piezoelectric and ferroelectric materials and structures for energy harvesting applications. *Energy Environ. Sci.* **2013**, *7*, 25–44. [CrossRef]
69. Mukherjee, A.; Datta, U. Comparative study of piezoelectric materials properties for green energy harvesting from vibration. In Proceedings of the 2010 Annual IEEE India Conference (INDICON), Kolkata, India, 17–19 December 2010. [CrossRef]
70. Jung, J.H.; Lee, M.; Hong, J.-I.; Ding, Y.; Chen, C.-Y.; Chou, L.-J.; Wang, Z.L. Lead-Free $NaNbO_3$ Nanowires for a High Output Piezoelectric Nanogenerator. *ACS Nano* **2011**, *5*, 10041–10046. [CrossRef]
71. Moorthy, B.; Baek, C.; Wang, J.E.; Jeong, C.K.; Moon, S.; Park, K.-I.; Kim, D.K. Piezoelectric energy harvesting from a PMN–PT single nanowire. *RSC Adv.* **2016**, *7*, 260–265. [CrossRef]
72. Lin, Y.-F.; Song, J.; Ding, Y.; Lu, S.-Y.; Wang, Z.L. Piezoelectric nanogenerator using CdS nanowires. *Appl. Phys. Lett.* **2008**, *92*, 022105. [CrossRef]
73. Naqvi, A.; Ali, A.; Altabey, W.A.; Kouritem, S.A. Energy Harvesting from Fluid Flow Using Piezoelectric Materials: A Review. *Energies* **2022**, *15*, 7424. [CrossRef]
74. Zhang, Z.; Chen, Y.; Guo, J. ZnO nanorods patterned-textile using a novel hydrothermal method for sandwich structured-piezoelectric nanogenerator for human energy harvesting. *Phys. E Low-Dimens. Syst. Nanostruct.* **2018**, *105*, 212–218. [CrossRef]
75. Qiu, Y.; Zhang, H.; Hu, L.; Yang, D.; Wang, L.; Wang, B.; Ji, J.; Liu, G.; Liu, X.; Lin, J.; et al. Flexible piezoelectric nanogenerators based on ZnO nanorods grown on common paper substrates. *Nanoscale* **2012**, *4*, 6568–6573. [CrossRef]
76. Lin, Z.-H.; Yang, Y.; Wu, J.M.; Liu, Y.; Zhang, F.; Wang, Z.L. $BaTiO_3$ Nanotubes-Based Flexible and Transparent Nanogenerators. *J. Phys. Chem. Lett.* **2012**, *3*, 3599–3604. [CrossRef]
77. Badatya, S.; Bharti, D.K.; Sathish, N.; Srivastava, A.K.; Gupta, M.K. Humidity Sustainable Hydrophobic Poly(vinylidene fluoride)-Carbon Nanotubes Foam Based Piezoelectric Nanogenerator. *ACS Appl. Mater. Interfaces* **2021**, *13*, 27245–27254. [CrossRef]
78. Ding, R.; Zhang, X.; Chen, G.; Wang, H.; Kishor, R.; Xiao, J.; Gao, F.; Zeng, K.; Chen, X.; Sun, X.W.; et al. High-performance piezoelectric nanogenerators composed of formamidinium lead halide perovskite nanoparticles and poly(vinylidene fluoride). *Nano Energy* **2017**, *37*, 126–135. [CrossRef]
79. Vivekananthan, V.; Chandrasekhar, A.; Alluri, N.R.; Purusothaman, Y.; Kim, W.J.; Kang, C.-N.; Kim, S.-J. A flexible piezoelectric composite nanogenerator based on doping enhanced lead-free nanoparticles. *Mater. Lett.* **2019**, *249*, 73–76. [CrossRef]
80. Lee, S.-G.; Monteiro, R.G.; Feigelson, R.S.; Lee, H.S.; Lee, M.; Park, S.-E. Growth and electrostrictive properties of $Pb(Mg_{1/3}Nb_{2/3})O_3$ crystals. *Appl. Phys. Lett.* **1999**, *74*, 1030–1032. [CrossRef]
81. Shin, S.-H.; Kim, Y.-H.; Lee, M.H.; Jung, J.-Y.; Nah, J. Hemispherically Aggregated $BaTiO_3$ Nanoparticle Composite Thin Film for High-Performance Flexible Piezoelectric Nanogenerator. *ACS Nano* **2014**, *8*, 2766–2773. [CrossRef]
82. Park, K.-I.; Xu, S.; Liu, Y.; Hwang, G.-T.; Kang, S.-J.L.; Wang, Z.L.; Lee, K.J. Piezoelectric $BaTiO_3$ Thin Film Nanogenerator on Plastic Substrates. *Nano Lett.* **2010**, *10*, 4939–4943. [CrossRef]
83. Uchino, K. Piezoelectric Energy Harvesting Systems—Essentials to Successful Developments. *Energy Technol.* **2018**, *6*, 829–848. [CrossRef]
84. Priya, S. Advances in energy harvesting using low profile piezoelectric transducers. *J. Electroceram.* **2007**, *19*, 167–184. [CrossRef]
85. Yang, Z.; Zhou, S.; Zu, J.; Inman, D. High-Performance Piezoelectric Energy Harvesters and Their Applications. *Joule* **2018**, *2*, 642–697. [CrossRef]

86. Talib, N.H.H.A.; Salleh, H.; Youn, B.D.; Resali, M.S.M. Comprehensive Review on Effective Strategies and Key Factors for High Performance Piezoelectric Energy Harvester at Low Frequency. *Int. J. Automot. Mech. Eng.* **2019**, *16*, 7181–7210. [CrossRef]
87. Ibrahim, S.W.; Ali, W.G. A review on frequency tuning methods for piezoelectric energy harvesting systems. *J. Renew. Sustain. Energy* **2012**, *4*, 062703. [CrossRef]
88. Yildirim, T.; Ghayesh, M.H.; Li, W.; Alici, G. A review on performance enhancement techniques for ambient vibration energy harvesters. *Renew. Sustain. Energy Rev.* **2017**, *71*, 435–449. [CrossRef]
89. Maamer, B.; Boughamoura, A.; El-Bab, A.M.F.; Francis, L.A.; Tounsi, F. A review on design improvements and techniques for mechanical energy harvesting using piezoelectric and electromagnetic schemes. *Energy Convers. Manag.* **2019**, *199*, 111973. [CrossRef]
90. Young, K.F.; Frederikse, H.P.R. Compilation of the Static Dielectric Constant of Inorganic Solids. *J. Phys. Chem. Ref. Data* **1973**, *2*, 313–410. [CrossRef]
91. Turner, R.; Fuierer, P.; Newnham, R.; Shrout, T. Materials for high temperature acoustic and vibration sensors: A review. *Appl. Acoust.* **1994**, *41*, 299–324. [CrossRef]
92. Cheng, K.; Chan, H.; Choy, C.; Yin, Q.; Luo, H.; Yin, Z. Single crystal PMN-0.33PT/epoxy 1-3 composites for ultrasonic transducer applications. *IEEE Trans. Ultrason. Ferroelectr. Freq. Control.* **2003**, *50*, 1177–1183. [CrossRef]
93. Tadigadapa, S.A.; Mateti, K. Piezoelectric MEMS sensors: State-of-the-art and perspectives. *Meas. Sci. Technol.* **2009**, *20*, 092001. [CrossRef]
94. Shung, K.K.; Cannata, J.M.; Zhou, Q.F. Piezoelectric materials for high frequency medical imaging applications: A review. *J. Electroceram.* **2007**, *19*, 141–147. [CrossRef]
95. Guy, I.L.; Muensit, S.; Goldys, E.M. Extensional piezoelectric coefficients of gallium nitride and aluminum nitride. *Appl. Phys. Lett.* **1999**, *75*, 4133–4135. [CrossRef]
96. Weis, R.S.; Gaylord, T.K. Lithium niobate: Summary of physical properties and crystal structure. *Appl. Phys. A* **1985**, *37*, 191–203. [CrossRef]
97. Wilson, S.A.; Jourdain, R.P.; Zhang, Q.; Dorey, R.A.; Bowen, C.R.; Willander, M.; Wahab, Q.U.; Al-Hilli, S.M.; Nur, O.; Quandt, E.; et al. New materials for micro-scale sensors and actuators: An engineering review. *Mater. Sci. Eng. R Rep.* **2007**, *56*, 1–129. [CrossRef]
98. Crisler, D.; Cupal, J.; Moore, A. Dielectric, piezoelectric, and electromechanical coupling constants of zinc oxide crystals. *Proc. IEEE* **1968**, *56*, 225–226. [CrossRef]
99. Qin, L.; Wang, Q.-M. Mass sensitivity of thin film bulk acoustic resonator sensors based on polar *c*-axis tilted zinc oxide and aluminum nitride thin film. *J. Appl. Phys.* **2010**, *108*, 104510. [CrossRef]
100. Muensit, S.; Goldys, E.M.; Guy, I.L. Shear piezoelectric coefficients of gallium nitride and aluminum nitride. *Appl. Phys. Lett.* **1999**, *75*, 3965–3967. [CrossRef]
101. Qin, L.; Wang, Q.-M. Analysis of dual-mode thin film bulk acoustic resonators based on polar c-axis tilted wurtzite gallium nitride. *J. Appl. Phys.* **2010**, *107*, 114102. [CrossRef]
102. Nam, C.-Y.; Jaroenapibal, P.; Tham, D.; Luzzi, D.E.; Evoy, S.; Fischer, J.E. Diameter-Dependent Electromechanical Properties of GaN Nanowires. *Nano Lett.* **2006**, *6*, 153–158. [CrossRef]
103. Gao, P.; Liu, K.; Liu, L.; Wang, Z.; Liao, Z.; Xu, Z.; Wang, W.; Bai, X.; Wang, E.; Li, Y. Higher-order harmonic resonances and mechanical properties of individual cadmium sulphide nanowires measured by in situ transmission electron microscopy. *J. Electron Microsc.* **2010**, *59*, 285–289. [CrossRef] [PubMed]
104. Ali, A.; Pasha, R.A.; Elahi, H.; Sheeraz, M.A.; Bibi, S.; Hassan, Z.U.; Eugeni, M.; Gaudenzi, P. Investigation of Deformation in Bimorph Piezoelectric Actuator: Analytical, Numerical and Experimental Approach. *Integr. Ferroelectr.* **2019**, *201*, 94–109. [CrossRef]
105. Maarsen, J.W.; Smit, M.C.; Matze, J. The Raman and infra-red spectra of some compounds $(iH_7C_3O)_2PXO$. *Recl. Trav. Chim. Pays-Bas* **1957**, *76*, 713–723. [CrossRef]
106. Sheeraz, M.A.; Butt, Z.; Khan, A.M.; Mehmood, S.; Ali, A.; Azeem, M.; Nasir, A.; Imtiaz, T. Design and Optimization of Piezoelectric Transducer (PZT-5H Stack). *J. Electron. Mater.* **2019**, *48*, 6487–6502. [CrossRef]
107. Guilbault, G.G.; Jordan, J.M.; Scheide, E. Analytical Uses of Piezoelectric Crystals: A Review. *CRC Crit. Rev. Anal. Chem.* **1988**, *19*, 1–28. [CrossRef]
108. Lu, C.; Czanderna, A.W. *Applications of Piezoelectric Quartz Crystal Microbalances*; Elsevier Science: Burlington, NJ, USA, 2012.
109. Guilbault, G.G.; Ngeh-Ngwainbi, J. Use of Protein Coatings on Piezoelectric Crystals for Assay of Gaseous Pollutants. In *Analytical Uses of Immobilized Biological Compounds for Detection, Medical and Industrial Uses*; Springer: Dordrecht, The Nethelands, 1988; pp. 187–194. [CrossRef]
110. Blum, L.J.; Coulet, P.R. *Biosensor Principles and Applications*; Dekker: New York, NY, USA, 1991.
111. King, W.H. Piezoelectric Sorption Detector. *Anal. Chem.* **1964**, *36*, 1735–1739. [CrossRef]
112. Lee, C.; Fung, Y.; Fung, K. A piezoelectric crystal detector for water in gases. *Anal. Chim. Acta* **1982**, *135*, 277–283. [CrossRef]
113. Shahid, M.; Javed, H.M.A.; Ahmad, M.I.; Qureshi, A.A.; Khan, M.I.; Alnuwaiser, M.A.; Ahmed, A.; Khan, M.A.; Tag-ElDin, E.S.M.; Shahid, A.; et al. A Brief Assessment on Recent Developments in Efficient Electrocatalytic Nitrogen Reduction with 2D Non-Metallic Nanomaterials. *Nanomaterials* **2022**, *12*, 3413. [CrossRef]

114. Okosun, F.; Guerin, S.; Celikin, M.; Pakrashi, V. Flexible amino acid-based energy harvesting for structural health monitoring of water pipes. *Cell Rep. Phys. Sci.* **2021**, *2*, 100434. [CrossRef]
115. Karasek, F.; Tiernay, J. Analytical performance of the piezoelectric crystal detector. *J. Chromatogr. A* **1974**, *89*, 31–38. [CrossRef]
116. Karasek, F.; Guy, P.; Hill, H.; Tiernay, J. Chromatographic design and temperature-related characteristics of the piezoelectric detector. *J. Chromatogr. A* **1976**, *124*, 179–186. [CrossRef]
117. Drake, P. The Development of Quartz Crystal Microbalance Based Chemical Sensors. Ph.D. Dissertation, University of Bath, Bath, UK, 2000.
118. Edmonds, T.; West, T. A quartz crystal piezoelectric device for monitoring organic gaseous pollutants. *Anal. Chim. Acta* **1980**, *117*, 147–157. [CrossRef]
119. Hu, J.; Qu, H.; Pang, W.; Duan, X. In-Line Detection with Microfluidic Bulk Acoustic Wave Resonator Gas Sensor for Gas Chromatography. *Sensors* **2021**, *21*, 6800. [CrossRef] [PubMed]
120. Yen, T.-Y.; Yao, D.-J. Detection of the Freshness of Kiwifruit With a TD-GC-MS and a Gas-Sensing Array Based on the Surface-Acoustic-Wave Technique. *IEEE Trans. NanoBiosci.* **2021**, *21*, 363–369. [CrossRef] [PubMed]
121. Christofides, C.; Mandelis, A. Solid-state sensors for trace hydrogen gas detection. *J. Appl. Phys.* **1990**, *68*, R1–R30. [CrossRef]
122. Thomas, J.H.; Sharma, S.P.; Iii, J.H.T. Adsorption and desorption of water on Au by the quartz-crystal-oscillator method. *J. Vac. Sci. Technol.* **1976**, *13*, 549–551. [CrossRef]
123. Smith, J.R.; Phelps, P. Septic arthritis, gout, pseudogout and osteoarthritis in the knee of a patient with multiple myeloma. *Arthritis Rheum.* **1972**, *15*, 89–96. [CrossRef]
124. Konash, P.L.; Bastiaans, G.J. Piezoelectric crystals as detectors in liquid chromatography. *Anal. Chem.* **1980**, *52*, 1929–1931. [CrossRef]
125. Oda, S.; Sawada, T. Laser-induced photoacoustic detector for high-performance liquid chromatography. *Anal. Chem.* **1981**, *53*, 471–474. [CrossRef]
126. Kartanas, T.; Levin, A.; Toprakcioglu, Z.; Scheidt, T.; Hakala, T.A.; Charmet, J.; Knowles, T.P. Label-free protein analysis using liquid chromatography with gravimetric detection. *Anal. Chem.* **2021**, *93*, 2848–2853. [CrossRef]
127. Jones, J.L.; Mieure, J.P. Piezoelectric transducer for determination of metals at the micromolar level. *Anal. Chem.* **1969**, *41*, 484–490. [CrossRef]
128. Nomura, T.; Mimatsu, T. Electrolytic determination of traces of iodide in solution with a piezoelectric quartz crystal. *Anal. Chim. Acta* **1982**, *143*, 237–241. [CrossRef]
129. Nomura, T.; Maruyama, M. Effect of metal ions on a piezoelectric quartz crystal in aqueous solution and the adsorptive determination of iron(III) as phosphate. *Anal. Chim. Acta* **1983**, *147*, 365–369. [CrossRef]
130. Ekrami, E.; Pouresmaieli, M.; Shariati, P.; Mahmoudifard, M. A review on designing biosensors for the detection of trace metals. *Appl. Geochem.* **2021**, *127*, 104902. [CrossRef]
131. Eddaif, L.; Shaban, A.; Telegdi, J. Sensitive detection of heavy metals ions based on the calixarene derivatives-modified piezoelectric resonators: A review. *Int. J. Environ. Anal. Chem.* **2019**, *99*, 824–853. [CrossRef]
132. Sartore, L.; Barbaglio, M.; Borgese, L.; Bontempi, E. Polymer-grafted QCM chemical sensor and application to heavy metal ions real time detection. *Sens. Actuators B Chem.* **2011**, *155*, 538–544. [CrossRef] [PubMed]
133. Hüseynli, S.; Çimen, D.; Bereli, N.; Denizli, A. Molecular Imprinted Based Quartz Crystal Microbalance Nanosensors for Mercury Detection. *Glob. Chall.* **2018**, *3*, 1800071. [CrossRef]
134. Narita, F.; Wang, Z.; Kurita, H.; Li, Z.; Shi, Y.; Jia, Y.; Soutis, C. A Review of Piezoelectric and Magnetostrictive Biosensor Materials for Detection of COVID-19 and Other Viruses. *Adv. Mater.* **2020**, *33*, e2005448. [CrossRef]
135. Huang, J.; Chen, B.; Fu, W.; Huang, Q.; Wang, J.; Liu, M. Detection of Human Papilloma Virus with Piezoelectric Quartz Crystal Genesensors Superconductivity and Quantum Phase Transition View project Ras localization and its relative function View project Detection of Human Papilloma Virus with Piezoelectric Quartz Crystal Genesensors. *Sens. Transducers Mag. (S&T e-Dig.)* **2004**, *42*, 214–219. Available online: http://www.sensorsportal.com (accessed on 25 October 2022).
136. Kleo, K.; Kapp, A.; Ascher, L.; Lisdat, F. Detection of vaccinia virus DNA by quartz crystal microbalance. *Anal. Biochem.* **2011**, *418*, 260–266. [CrossRef]
137. Wu, T.-Z.; Su, C.-C.; Chen, L.-K.; Yang, H.-H.; Tai, D.-F.; Peng, K.-C. Piezoelectric immunochip for the detection of dengue fever in viremia phase. *Biosens. Bioelectron.* **2005**, *21*, 689–695. [CrossRef] [PubMed]
138. Baca, J.T.; Severns, V.; Lovato, D.; Branch, D.W.; Larson, R.S. Rapid Detection of Ebola Virus with a Reagent-Free, Point-of-Care Biosensor. *Sensors* **2015**, *15*, 8605–8614. [CrossRef]
139. Jiang, Y.; Tan, C.Y.; Tan, S.Y.; Wong, M.S.F.; Chen, Y.F.; Zhang, L.; Yao, K.; Gan, S.K.E.; Verma, C.; Tan, Y.-J. SAW sensor for Influenza A virus detection enabled with efficient surface functionalization. *Sens. Actuators B Chem.* **2014**, *209*, 78–84. [CrossRef]
140. Xu, T.; Miao, J.; Wang, Z.; Yu, L.; Li, C.M. Micro-piezoelectric immunoassay chip for simultaneous detection of Hepatitis B virus and α-fetoprotein. *Sens. Actuators B Chem.* **2011**, *151*, 370–376. [CrossRef]
141. Giri, B.; Pandey, S.; Shrestha, R.; Pokharel, K.; Ligler, F.S.; Neupane, B.B. Review of analytical performance of COVID-19 detection methods. *Anal. Bioanal. Chem.* **2020**, *413*, 35–48. [CrossRef] [PubMed]
142. Zuo, B.; Li, S.; Guo, Z.; Zhang, J.; Chen, C. Piezoelectric Immunosensor for SARS-Associated Coronavirus in Sputum. *Anal. Chem.* **2004**, *76*, 3536–3540. [CrossRef]

143. Pandey, L.M. Design of engineered surfaces for prospective detection of SARS-CoV-2 using quartz crystal microbalance-based techniques. *Expert Rev. Proteom.* **2020**, *17*, 425–432. [CrossRef]
144. Cheney, J.; Norwood, T.; Homolya, J. The Detection of Sulfur Dioxide Utilizing a Piezo-Electric Crystal Coated with Ethylenedinitrilotetraethanol. *Anal. Lett.* **1976**, *9*, 361–377. [CrossRef]
145. Guilbault, G.G.; Lopez-Roman, A. Use of Sodium Tetrachloromercuriate as a Substrate for the Determination of So2 on the Piezocrystal Detector. *Environ. Lett.* **1971**, *2*, 35–45. [CrossRef]
146. Cheney, J.L.; Homolya, J.B. The development of a sulfur dioxide continuous monitor incorporating a piezo-electric sorption detector. *Sci. Total Environ.* **1976**, *5*, 69–77. [CrossRef]
147. Wade, W.H.; Slutsky, L.J. Adsorption on Quartz Single Crystals. In *Vacuum Microbalance Techniques*; Springer: Boston, MA, USA, 1962; pp. 115–128. [CrossRef]
148. Guilbault, G.G.; Lopez-Roman, A.; Billedeau, S. Gas-phase reactions of mono-, di-, and trimethylamine with various metal salts: The use of piezoelectric crystals in a vacuum system. *Anal. Chim. Acta* **1972**, *58*, 421–427. [CrossRef]
149. Karmarkar, K.H.; Webber, L.M.; Guilbault, G.G. Measurement of SO 2 in Air Using Coated Piezoelectric Crystal Detectors. *Environ. Lett.* **1975**, *8*, 345–352. [CrossRef]
150. Karmarkar, K.; Guilbault, G. A new design and coatings for piezoelectric crystals in measurement of trace amounts of sulfur dioxide. *Anal. Chim. Acta* **1974**, *71*, 419–424. [CrossRef]
151. Frechette, M.W.; Fasching, J.L.; Rosie, D.M. Evaluation of substrates for use on a piezoelectric detector for sulfur dioxide. *Anal. Chem.* **1973**, *45*, 1765–1766. [CrossRef]
152. Frechette, M.W.; Fasching, J.L. Simple Piezoelectric Probe for Detection and Measurement of SO_2. *Environ. Sci. Technol.* **1973**, *7*, 1135–1137. [CrossRef]
153. Webber, L.; Karmarkar, K.; Guilbault, G. A coated piezoelectric crystal detector for the selective detection and determination of hydrogen sulfide in the atmosphere. *Anal. Chim. Acta* **1978**, *97*, 29–35. [CrossRef]
154. Hlavay, J.; Guilbault, G.G. Applications of the piezoelectric crystal detector in analytical chemistry. *Anal. Chem.* **1977**, *49*, 1890–1898. [CrossRef]
155. Webber, L.M.; Guilbault, G.G. Coated piezoelectric crystal detector for selective detection of ammonia in the atmosphere. *Anal. Chem.* **1976**, *48*, 2244–2247. [CrossRef]
156. Tomita, Y.; Guilbault, G.G. Coating for a piezoelectric crystal sensitive to organophosphorus pesticides. *Anal. Chem.* **1980**, *52*, 1484–1489. [CrossRef]
157. Suleiman, A.; Guilbault, G. Piezoelectric Crystal Detectors for Environmental Pollutants. *Stud. Environ. Sci.* **1994**, *59*, 273–303. [CrossRef]
158. Shackelford, W.M.; Guilbault, G.G. A piezoelectric detector for organophosphorus pesticides in the air. *Anal. Chim. Acta* **1974**, *73*, 383–389. [CrossRef] [PubMed]
159. Scheide, E.P.; Guilbault, G.G. Piezoelectric detectors for organophosphorus compounds and pesticides. *Anal. Chem.* **1972**, *44*, 1764–1768. [CrossRef]
160. Nomura, T.; Hattori, O. Determination of micromolar concentrations of cyanide in solution with a piezoelectric detector. *Anal. Chim. Acta* **1980**, *115*, 323–326. [CrossRef]
161. Nomura, T. Single-drop method for determination of cyanide in solution with a piezoelectric quartz crystal. *Anal. Chim. Acta* **1981**, *124*, 81–84. [CrossRef]
162. Morris, R.G.; Downes, J.J.; Sahakian, B.J.; Evenden, J.L.; Heald, A.; Robbins, T.W. Planning and spatial working memory in Parkinson's disease. *J. Neurol. Neurosurg. Psychiatry* **1988**, *51*, 757–766. [CrossRef]
163. Nomura, T.; Okuhara, M. Frequency shifts of piezoelectric quartz crystals immersed in organic liquids. *Anal. Chim. Acta* **1982**, *142*, 281–284. [CrossRef]
164. Nomura, T.; Tsuge, K. Determination of silver in solution with a piezoelectric detector after electrodeposition. *Anal. Chim. Acta* **1985**, *169*, 257–262. [CrossRef]
165. Nomura, T.; Watanabe, M.; West, T. Behaviour of piezoelectric quartz crystals in solutions with application to the determination of iodide. *Anal. Chim. Acta* **1985**, *175*, 107–116. [CrossRef]
166. Daley, P.S.; Lundgren, D.A. The Performance of Piezoelectric Crystal Sensors Used to Determine Aerosol Mass Concentrations. *Am. Ind. Hyg. Assoc. J.* **1975**, *36*, 518–532. [CrossRef]
167. Olin, J.G.; Sem, G.J. Piezoelectric microbalance for monitoring the mass concentration of suspended particles. *Atmos. Environ. (1967)* **1971**, *5*, 653–668. [CrossRef]
168. Liu, B.Y. *Fine Particles: Aerosol Generation, Measurement, Sampling and Analysis*; Academic Press: New York, NY, USA, 1976.
169. Karmarkar, K.; Webber, L.; Guilbault, G. Measurement of sulfur dioxide in automobile exhausts and industrial stack gases with a coated piezoelectric crystal detector. *Anal. Chim. Acta* **1976**, *81*, 265–271. [CrossRef] [PubMed]
170. Tomita, Y.; Ho, M.H.; Guilbault, G.G. Detection of explosives with a coated piezoelectric quartz crystal. *Anal. Chem.* **1979**, *51*, 1475–1478. [CrossRef]
171. Behrndt, K.; Love, R. Automatic control of film-deposition rate with the crystal oscillator for preparation of alloy films. *Vacuum* **1962**, *12*, 1–9. [CrossRef]
172. Oberg, P.; Lingensjo, J. Crystal Film Thickness Monitor. *Rev. Sci. Instrum.* **1959**, *30*, 1053. [CrossRef]

173. Richardson, P.D. Discussion of paper by W. H. King., Jr.: The use of resonating devices to make small mass measurements. *Bull. N. Y. Acad. Med.* **1972**, *48*, 465–467.
174. Hammond, D.L.; Benjaminson, A. The crystal resonator- a digital transducer. *IEEE Spectr.* **1969**, *6*, 53–58. [CrossRef]
175. King, W.H.; Camilli, C.T.; Findeis, A.F. Thin Film Thermocouples for Differential Thermal Analysis. *Anal. Chem.* **1968**, *40*, 1330–1335. [CrossRef]

Disclaimer/Publisher's Note: The statements, opinions and data contained in all publications are solely those of the individual author(s) and contributor(s) and not of MDPI and/or the editor(s). MDPI and/or the editor(s) disclaim responsibility for any injury to people or property resulting from any ideas, methods, instructions or products referred to in the content.